

Time-Resolved Transmission Electron Microscopy: Instrumentation and Applications

Présentée le 14 juin 2021

Faculté des sciences de base
Laboratoire de nanodynamique moléculaire
Programme doctoral en chimie et génie chimique

pour l'obtention du grade de Docteur ès Sciences

par

Pavel OLSHIN

Acceptée sur proposition du jury

Prof. R. Beck, président du jury
Prof. U. Lorenz, directeur de thèse
Dr F. Houdellier, rapporteur
Prof. O.-H. Kwon, rapporteur
Prof. C. Bostedt, rapporteur

Abstract

In recent decades, *in situ* electron microscopy has attracted considerable attention. The method enables real time observations of the transformations of nanoparticles under various stimuli with atomic spatial resolution. Time-resolved electron microscopy adds a new dimension, time, to such experiments, making it possible to study fast and ultrafast processes on their natural timescales. This thesis presents the work devoted to the development and characterization of a time-resolved transmission electron microscope, as well as multiple studies that demonstrate its capabilities to perform various *in situ* experiments at timescales from minutes to hundreds of femtoseconds.

In **Chapter 2**, the transformation of a conventional transmission electron microscope into a time-resolved instrument is discussed. The required modifications include the installation of several optical elements inside the device. Some of them aimed to direct a laser beam to a sample, other to focus a laser beam into the electron gun to generate electron pulses. Our optical scheme allows us to generate high brightness electron pulses from the tungsten filament, or pulses with a high number of electrons from the extractor electrode. The energy spread, duration of pulses, and instantaneous brightness of the electron beams generated by the nanosecond and femtosecond UV lasers were characterized. Thus, a wide range of experiments can be carried out with the instrument developed in our group.

Chapter 3 presents an *in situ* electron microscopy study of Coulomb fission of plasmonic nanoparticles under femtosecond laser irradiation. Gold nanoparticles encapsulated in a silica shell fission by ejecting gold clusters of 1-2 nm diameter. Continued exposure to the laser beam leads to the coalescence of the ejected particles into a second core within seconds. Under ultrafast pulses, the core ionizes, emitting the electrons along the laser polarization direction. The resulting uneven charge distribution in the silica shell then causes the progeny particles to

be ejected in the same direction. This chapter demonstrates that the combination of ultrafast laser systems with a transmission electron microscope allows *in situ* observations of complex laser-driven processes with high spatial resolution.

Chapter 4 presents a time-resolved electron microscopy study that elucidates the morphological dynamics of so-called jumping nanodroplets that were created by melting triangular gold nanoprisms on a graphene surface with a laser pulse. A nanoscale movie was recorded that shows the shape evolution of the droplets as they dewet and jump off the substrate. Inhomogeneities of the graphene surface lead to variations in the dewetting trajectories. Surprisingly, some droplets adopt cylindrical or dumbbell-shaped geometries after they jump, suggesting that they spin with considerable angular momentum.

Keywords: *in situ* electron microscopy, time-resolved transmission electron microscopy, light-matter interaction, photon induced near field electron microscopy, stroboscopic experiments, single shot imaging, femtosecond laser, laser heating, dewetting, gold nanoparticles.

Riassunto

Negli ultimi decenni, la microscopia elettronica *in situ* ha guadagnato considerevole attenzione, garantendo la possibilità di visualizzare processi fisico-chimici in tempo reale con risoluzione atomica. L'ambito della microscopia elettronica *time-resolved* (con risoluzione temporale), ha successivamente aperto le porte allo studio di processi veloci e ultraveloci, che possono essere visualizzati con una risoluzione temporale di pochi femtosecondi. Questa tesi presenta lo sviluppo di un microscopio elettronico *time-resolved*, insieme ad alcuni esempi che ne dimostrano la capacità su diverse scale temporali.

Nel **secondo capitolo** viene affrontata la trasformazione di un microscopio convenzionale in uno strumento *time-resolved*. Il lavoro ha richiesto l'installazione di diverse componenti ottiche - alcune per dirigere un fascio laser verso il campione, altre per generare impulsi di elettroni a partire dal cannone. Il nostro apparato consente l'emissione di elettroni da diverse parti del cannone, rendendo possibile la scelta di diversi tipi di impulsi a seconda delle caratteristiche dell'esperimento. Viene anche fornita una caratterizzazione completa degli impulsi di elettroni - risoluzione spaziale, temporale e diffusione delle energie.

Nel **terzo capitolo** viene presentato uno studio *in situ* della fissione coulombiana di nanoparticelle plasmoniche irradiate con impulsi laser al nanosecondo e femtosecondo. Le nanoparticelle - oro incastonato in un guscio di silica - espellono piccoli aggregati di 1-2 nm, che si fondono durante l'irradiazione fino a formare un aggregato di dimensioni simili alla particella originale. Quando viene illuminata con un impulso laser di alcuni femtosecondi, la nanoparticella d'oro viene ionizzata, emettendo elettroni nella direzione della polarizzazione del laser. Gli elettroni rimangono impiantati nel guscio di silica per alcuni secondi. Per minimizzare la repulsione coulombiana, la nanoparticella emette dei frammenti che vengono attratti dagli elettroni espulsi in precedenza, allineandosi così alla direzione della

polarizzazione del laser. Il capitolo dimostra quindi come l'integrazione di laser ultraveloci in un TEM consenta lo studio di nuovi complicati processi con elevata risoluzione.

Nel **quarto capitolo** viene presentato uno studio sulle cosiddette “jumping nanodroplets”. Un nano-prisma triangolare d'oro, su una superficie di grafene, viene sciolto grazie a un impulso laser; la nano-goccia che ne emerge, saltando dalla superficie, viene studiata grazie a un filmato alla nanoscala, che ne rivela la complicata evoluzione temporale. La traiettoria della nano-goccia dipende dalle inomogeneità del grafene. Alcune delle gocce mostrano una forma cilindrica o “a manubrio”, evidenziando la presenza di un elevato momento angolare.

Parole chiave: microscopia elettronica in situ, microscopia elettronica con risoluzione temporale, interazione luce-materia, microscopia elettronica a campo vicino fotonico, esperimenti stroboscopici, impulso singolo, laser al femtosecond, riscaldamento laser, dewetting, nanoparticelle d'oro

List of Abbreviations

TEM – transmission electron microscopy (microscope);

CFE – cold field emitter;

HR-TEM – high resolution transmission electron microscopy;

STEM – scanning transmission electron microscopy;

UV – ultraviolet;

FWHM – full width at half maximum;

CLA – condenser lens aperture.

Table of Contents

Abstract

Riassunto

List of Abbreviations

Chapter 1 Introduction.....8

The role of microscopy in science.....8

In situ TEM.....10

There is plenty of time in a second.....11

Electron guns in electron microscopy.....13

Outline.....17

References.....19

Chapter 2 Characterization of a Time-Resolved Electron Microscope with a Schottky

Field Emission Gun.....31

Introduction.....31

Experimental Setup.....34

Results and Discussion.....37

Conclusion.....48

References.....49

Chapter 3 *In Situ* Observation of Coulomb Fission of Individual Plasmonic

Nanoparticles.....57

Introduction.....57

Results and Discussion.....59

Conclusion.....70

References.....72

Chapter 4 Real-Time Observation of Jumping and Spinning Nanodroplets.....	78
Introduction.....	78
Experimental Setup.....	80
Results and Discussion.....	83
Conclusion.....	92
References.....	93
Chapter 5 Conclusion and Outlook.....	98
References.....	102
Appendix 1 Supporting information for Chapter 4.....	106
References.....	112
List of Figures.....	114
List of Tables.....	116
Acknowledgments.....	117
Curriculum Vitae.....	119

Chapter 1

Introduction

The role of microscopy in science

Visual perception plays an important role in the popularization of scientific knowledge. A few years ago, the first image of a black hole gained widespread attention in the mass media ¹. Enormous efforts of a team of scientists from different fields, who used data from observatories located in different parts of the world, from Hawaii to Antarctica, led to a series of publications ²⁻⁷. Petabytes of raw data and two years of thorough analysis yielded the first image of a black hole, showing of a black region in the center with an orange crescent-like structure surrounding it. Images are useful because they can be easily interpreted. Even if images are recorded with complicated tools, they can be used to communicate the main concept of a discovery to a non-specialist viewer. For example, one does not need to be an expert in electron microscopy to understand the magnificent images of insects or cell organelles, recorded with scanning electron microscopy, or transmission electron microscopy (TEM), respectively.

At the same time, visual observation is an important tool in science. For a long time, the unaided eye was the only imaging device available to early researchers. As Stefan Hell noted in his Nobel lecture, the ‘...historical beginning of modern natural sciences very much coincides with the invention of light microscopy’ ⁸. The discovery and interpretation of the phenomenon of Brownian motion is a good illustration of the importance of imaging techniques, especially microscopy, in modern science. The idea that all objects are composed of small indivisible blocks, atoms, which constantly move and collide with each other, was proposed by ancient scientists ^{9,10}. But it was not until the invention of a microscope that the effects caused by atomic and molecular collisions could be detected ¹¹. Robert Brown in 1827

observed and systematically studied chaotic movements of micrometer sized particles ¹², which were large enough to be seen in an optical microscope, and small enough to be moved by the molecules in a liquid. The phenomenon remained largely unexplained until 1905, when A. Einstein used molecular kinetic theory to describe Brownian motion. To check the validity of his calculations, he proposed to measure the mean displacement of particles suspended in a liquid. Experimental verification of his theory would mean that "... classical thermodynamics can no longer be looked upon as applicable with precision to bodies even of dimensions distinguishable in a microscope..." ¹³. In the following years, J. Perrin performed thorough measurements of the mean path lengths of microscopic particles in liquids with an ultra-microscope, a new instrument that had been developed a short time before ^{14,15}. These experiments confirmed the molecular kinetic theory, the existence of atoms and molecules, and, what is more important, the discontinuous structure of matter ¹⁶.

The increasing resolving power of the microscopes has since allowed modern microscopists to reveal many important insights into the structure and properties of matter. For a long time, the resolving power of microscopes was limited by diffraction, in accordance with the Abbe formula:

$$d = \frac{\lambda}{2n \cdot \sin\alpha} ,$$

where d is the resolution, λ is the light wavelength, n is the refractive index of the medium, and α is the convergence semi angle. According to this equation, the resolution of an optical microscope cannot be better than several hundred nanometers. In the last century, however, many techniques with higher resolving power have been developed. In optical microscopy, the Abbe limit was circumvented with super-resolution methods that are based on localizing individual fluorescent particles with a precision much higher than the resolution limit of the microscope would allow ^{17,18}. Some other methods are based on using shorter wavelengths,

such as in X-ray^{19,20} and electron microscopy²¹. Scanning probe techniques^{22,23} such as atomic force microscopy and scanning tunneling microscopy rely upon a different physical principle, namely, on the interaction of a sample with a sharp tip. In these methods, the resolution is defined by the tip size and the precision of the probe positioning, and can reach sub-nm values.

In situ TEM

Transmission electron microscopy is based on the same principle as light microscopy, but with photons replaced by electrons and the glass optics replaced with magnetic lenses. As charged particles, electrons interact strongly with matter, providing various signals, which can be detected and used to collect diverse information about a sample. Morphology, structure, chemical composition, and optical properties are among the types of information that can be extracted from real space images, electron diffraction patterns, electron energy loss spectra, X-ray energy dispersive spectra, and cathodoluminescence analysis.

Although the examination of static samples provides valuable information about the structure and composition of materials, observations of their behavior under various stimuli at the nano- and microscale can provide additional information about their properties. In their review on the future of *in situ* electron microscopy, H. Zheng and Y. Zhu refer to this method as “one of the major future directions of electron microscopy”²⁴. *In situ* experiments allow researchers to observe the evolution of a specimen under the effect of an external stimulus. Therefore special specimen holders have been designed to study samples *in situ* under a variety of different conditions, such under heating^{25–27}, electrical bias²⁸, mechanical stress²⁹, or in a liquid or gaseous environment³⁰.

Laser illumination is also used as an external stimulus in *in situ* TEM³¹. A laser beam can be focused to a spot of tens of micrometers, providing fast local heating, so that the specimen temperature can be rapidly increased to values exceeding those achievable in heating

holders (1200-1300 °C). Ultrafast lasers have also been used to reach extreme conditions (peak laser powers in the focal point can reach values of several TW/cm²), which are otherwise difficult to attain with other methods. Direct observation of femtosecond laser induced transformations can shed light on basic mechanisms of intense light-matter interactions, which are of fundamental and applied interest.

There is plenty of time in a second

Specimen changes during *in situ* experiments are typically observed and recorded with electron cameras ^{32–35}. Although modern detectors provide millisecond temporal resolution ³⁶, direct observation of fast dynamics is not possible with a conventional TEM. Therefore, it was proposed to study fast processes with stroboscopic electron microscopy, in which reversible dynamics of a sample are periodically excited and probed at a specific moment in time. With this approach, the temporal resolution of the instrument does not depend on the detector, but is limited by the electron pulse duration in the sample plane. In early experiments, stroboscopic imaging in transmission and scanning electron microscopy was performed with nanosecond electron pulses generated with electrostatic deflectors ^{37–40}.

To study irreversible processes, a single shot approach was developed, which is based on probing the transient state of a specimen with just one electron pulse. K. Ura and A. Takaoka applied electron pulses of 30 μs duration, which were produced by modulating the extraction field in a thermal field emission gun, to study various processes, for example, the movement of dislocations in metal films ⁴¹. They also used a deflection coil to shift the electron beam position on the photographic film to record several images with a short delay. This approach has become known in time-resolved electron microscopy as ‘movie mode’.

The groups of O. Bostanjoglo ^{42–44} and N. Browning ^{45,46} used a similar approach, but generated electron pulses by illuminating metal photocathodes with ultraviolet nanosecond

laser pulses, with the specimen dynamics induced by a pump laser pulse. In order to record single shot images, electron pulses with high charges (10^6 - 10^9 electrons) are required, which limits the temporal resolution of the method to several nanoseconds due to space charge effects^{44,47,48}.

The group of A. Zewail achieved femtosecond temporal resolution in TEM in stroboscopic pump-probe experiments. They used ultrafast electron pulses containing a small number of electrons, sometimes, below 1 electron per pulse⁴⁹ to minimize the Coulomb interactions that ultimately limit both the temporal and spatial coherence⁵⁰.

Real space images, diffraction patterns and energy loss spectra can be recorded with high temporal resolution in a time-resolved electron microscope⁵¹. The versatility of the method has stimulated studies of a range of phenomena on the nanoscale⁵²⁻⁵⁸. Sometimes, several microscopy modes are used together to elucidate various aspects of a physical or chemical process. Irradiation with a laser pulse can lead to the excitation of phonon waves⁵⁹, vibrational oscillations⁶⁰, thermal expansion⁶¹, or various deformations of the sample⁶². Bright and dark field imaging together with electron diffraction are actively used to study these phenomena to obtain information about the mechanical properties of various nanoscale objects, for example, organic^{60,63,64} and inorganic materials⁶⁵⁻⁶⁸, metal-organic framework nanocrystals⁶⁹, carbon nanotubes⁷⁰⁻⁷², or 2-D materials⁶². The temperature jump caused by the laser illumination can also induce phase transitions, or chemical transformation of the specimen. Depending on the material and the nature of the process, it can be studied stroboscopically, or with the single-shot method. Valuable information about the transient state of the materials can be obtained with both electron diffraction^{69,73} and real space imaging^{43,44,46,47,74,75}. Electron energy loss spectroscopy can be used to measure the dynamical changes in the electronic structure⁷⁶⁻⁷⁸, or the rate of a chemical⁴⁸.

Ultrafast transmission electron microscopy also opened up a new direction in quantum optics, namely the manipulation of electron wave packets with light fields. A good example of the method is near field photon induced microscopy, which is characterized by changing the electron energy (increasing or decreasing) by multiples of the photon energy of the probe laser⁷⁹. Typically, the coupling of free electrons and photons is impossible because of the energy-momentum mismatch, but in the presence of the light induced electric field around a nanoparticle, the interaction is achievable^{80,81}. The number of absorbed/emitted photons depends on the field intensity at a specific point relative to an object. The field strength is determined by the laser power⁸¹, the laser polarization direction⁷⁹, the dielectric properties of the specimen⁸⁰, and the distance of the probe beam from the specimen⁸². Besides studies of fundamental photon-electron interactions, PINEM is widely used for finding the temporal overlap in ultrafast TEM and the characterization of electron pulses. The short lifetime of the evanescent electric field (10-100 fs) makes it possible to use this effect for the measurement of the cross-correlation between the laser and electron pulse. Another promising application of the effect is the improvement of the temporal resolution via photon gating⁸³ or the generation of attosecond electron combs⁸⁴.

Electron guns in electron microscopy

The electron gun of an electron microscope crucially determines the properties of the electron beam, such as the spatial coherence, brightness, or energy spread, and therefore the ultimate performance of the instrument. Historically, the first electron guns in TEM were based on thermal emission, with the emission current depending on the temperature and the work function of the material. Therefore, the most popular materials have been tungsten, the metal with the highest melting point, and lanthanum hexaboride, a material with a low work function. Thermionic guns consist of several electrodes: an emitter, a Wehnelt cap, and an accelerator.

The cap is biased negatively with respect to the emitter, and is used to determine the source size and focus the electron beam through the anode, where the electrons reach the desired velocity ($\sim 2/3$ of the speed of light at 200 kV). Thermionic guns are robust, can operate at high pressures (10^{-3} - 10^{-5} Pa), and provide high currents. The high temperature of the emitter leads to significant energy spreads above 2 eV for tungsten hairpins, and around 1 eV for LaB₆ crystals. The size of the electron source limits the spatial coherence, which is important for applications based on the interference of the electron waves.

In most advanced TEM applications, tungsten tip based electron guns are used. Schottky and cold field emitters (CFE) electron gun assemblies are similar and consist of several electrodes: the cathode, which is a tungsten needle with an apex sharpened to sub-micron size, the extractor, that creates the strong electric field (10^8 - 10^9 V/m) around the filament, and the focusing electrode, that defines the convergence of the electron beam while it travels down the column. The main difference between the two types of the guns is the size of the apex of the filament. The emitting surface can be as small as 10 nm in diameter for CFEs, and reach several hundred nanometers for Schottky filaments. Low dimensions of the CFE result in much stronger fields at the apex, making tunneling possible. Schottky type emitters are sometimes called ‘field assisted thermal emitters’⁸⁵, as the emission occurs due to the thermal excitation of electrons from a hot (~ 1800 K) cathode, while the electric field only decreases the work function. The filament is also covered with an atomically thin layer of ZrO₂ to reduce the work function further⁸⁶. Electron emission from the shank of the hot cathode is prevented by using an additional electrode, named suppressor, that is biased negatively with respect to the filament.

Among the different figures of merit of an electron gun, its transverse brightness, defined as the current density per unit solid angle, is particularly important. High brightness is advantageous for high resolution TEM (HR-TEM), scanning TEM (STEM)⁸⁷, and for electron holography⁸⁸. Thermionic emitters deliver electron beams with high currents, but low

brightness ($\sim 10^{10}$ A/m²sr)⁸⁹, while tip based cathodes provide low current beams with high brightness ($\sim 10^{13}$ A/m²sr)⁹⁰. Such a large difference is the result of a significantly smaller electron source size for Schottky and CFE guns.

Different types of electron guns have been adapted for time-resolved electron microscopy. The first instruments employing photoemission sources were equipped with thermionic electron guns^{43,46,49}. In the last decade, a number of groups have installed time-resolved TEMs^{61,91–99}, most of them equipped with thermionic emitters, either LaB₆ crystals or flat metal plates. Recently, a new generation of ultrafast TEMs with tip emitters has been introduced^{92,95,97}. Although thermionic emitters can provide higher currents, in stroboscopic mode, when about one electron per pulse is used, the beam quality is higher for point source emitters. Therefore, single shot imaging is typically performed with instruments equipped with thermionic guns, while experiments requiring the highest coherence, such as electron holography, have only become possible with tip based instruments^{58,100}.

Time-resolved electron microscopy suffers from low average currents that are several orders of magnitude smaller than during conventional operation. Employing pulses with a larger number of electrons per pulse could significantly decrease the time of the experiment, or improve the signal to noise ratio. Unfortunately, Coulomb repulsion between electrons prevents the generation of high charge pulses and decreases the spatial, energy, and temporal resolution. For example, spatial and energy resolution in a single shot experiments are as low as 10 nm⁴⁵ and 30 eV⁴⁸, respectively. Space charge interactions are especially important for ultrafast pulses, where the pulse duration can suffer significantly due to Coulomb repulsion.

The number of electrons extracted with femtosecond pulses is very low, and does not exceed 10^3 - 10^4 ^{91,93,96} and 10 - 20 ^{92,100} electrons in a pulse for thermionic and filament-based emitters, respectively. Therefore, ultrafast single shot experiments with atomic spatial resolution in real space have not been reported yet. It should be noted that using electron pulses

accelerated to relativistic velocities can decrease the negative effects of Coulomb interactions^{101,102}.

Outline

This thesis describes the implementation and characterization of a time-resolved transmission electron microscope equipped with a Schottky field emission gun and presents its application to study several fast nanoscale processes. The document is divided in four chapters. Briefly, **Chapters 2** describes the instrument, the design of the modifications, and its capabilities. **Chapter 3** details *in situ* observations of the fragmentation of gold nanoparticles embedded in a silica shell under ultrafast laser irradiation. **Chapter 4** presents a study of fast fluid dynamics with nanosecond temporal resolution. **Chapter 5** summarizes the work and proposes future directions in the field.

Initially, my work was devoted to building a time-resolved transmission electron microscope, which can be operated in different modes, with the high current beam similar to that produced from a flat emitter, or with the high brightness beam from a Schottky emitter. **Chapter 2** contains details related to the modification and characterization of our instrument. In our design, the mirror that directs the UV laser beam to a Schottky filament, is installed inside the focusing electrode of the gun assembly, allowing the generation of electron pulses from both the tip and the extractor electrode. Thus, depending on the desired application, we can choose to operate an electron beam with high brightness or with high current. In this chapter, the effect of the probe laser power on the electron beam parameters, such as the number of electrons in a pulse, energy spread, pulse duration, and the beam brightness, are also discussed.

Chapter 3, presents an *in situ* study involving Coulomb fission of plasmonic nanoparticles under femtosecond laser irradiation. It is shown that gold nanoparticles embedded in a silica shell eject small gold clusters of about 10-500 atoms under illumination with the femtosecond laser beam. Over time, the number of ejected progeny particles increases,

and they coalesce in the second particle. The effect of the laser beam parameters, such as pulse energy and polarization, on this process is discussed. The direct observation of the reshaping of the gold nanoparticles yields insights into the mechanism of Coulomb fission of gold nanoparticles. Similar experiments can provide valuable information about the mechanism of the laser processing that can significantly expand the understanding of the interaction of intense laser beams with various materials.

In **Chapter 4**, a time-resolved study of so-called jumping nanodroplets is described. In this experiment, a picosecond laser pulse initiates melting of a gold nanoprism on a graphene surface, followed by the fast contraction of the liquid metal into a sphere and its detachment from the substrate. In this experiment, we make use of the ability of our instrument to generate electron pulses with a high number of electrons and, consequently, perform single shot experiments. The shape evolution of the prisms during the contraction, and the parameters affecting the jumping process are discussed.

Finally, **Chapter 5** provides a conclusion and outlook.

References

- (1) Castelvechi, D. Black Hole Imaged for First Time. *Nature* **2019**, 568, 284–285.
- (2) The Event Horizon Telescope Collaboration et al. First M87 Event Horizon Telescope Results. I. The Shadow of the Supermassive Black Hole. *Astrophys. J. Lett.* **2019**, 875, L1.
- (3) The Event Horizon Telescope Collaboration et al. First M87 Event Horizon Telescope Results. II. Array and Instrumentation. *Astrophys. J. Lett.* **2019**, 875, L2.
- (4) The Event Horizon Telescope Collaboration et al. First M87 Event Horizon Telescope Results. III. Data Processing and Calibration. *Astrophys. J. Lett.* **2019**, 875, L3.
- (5) The Event Horizon Telescope Collaboration et al. First M87 Event Horizon Telescope Results. IV. Imaging the Central Supermassive Black Hole. *Astrophys. J. Lett.* **2019**, 875, L4.
- (6) The Event Horizon Telescope Collaboration et al. First M87 Event Horizon Telescope Results. V. Physical Origin of the Asymmetric Ring. *Astrophys. J. Lett.* **2019**, 875, L5.
- (7) The Event Horizon Telescope Collaboration et al. First M87 Event Horizon Telescope Results. VI. The Shadow and Mass of the Central Black Hole. *Astrophys. J. Lett.* **2019**, 875, L6.
- (8) Hell, S. W. Nanoscopy with Focused Light, 2014.
- (9) Jenkin, F. The Atomic Theory of Lucretius. *North Br. Rev.* **1868**, 48 (95), 211–242.
- (10) Tóthová, J.; Vasziová, G.; Glod, L.; Lisy, V. Langevin Theory of Anomalous Brownian Motion Made Simple. *Eur. J. Phys.* **2011**, 32 (5), 1437–1437.
- (11) Frey, E.; Kroy, K. Brownian Motion: A Paradigm of Soft Matter and Biological Physics. *Ann. Phys.* **2005**, 14 (1–3), 20–50.
- (12) Brown, R. XXVII. A Brief Account of Microscopical Observations Made in the Months of June, July and August 1827, on the Particles Contained in the Pollen of Plants; and on the

General Existence of Active Molecules in Organic and Inorganic Bodies. *Philos. Mag.* **1828**, 4 (21), 161–173.

(13) Einstein, A. Über die von der molekularkinetischen Theorie der Wärme geforderte Bewegung von in ruhenden Flüssigkeiten suspendierten Teilchen. *Ann. Phys.* **1905**, 322 (8), 549–560.

(14) Perrin, J. B. Mouvement brownien et grandeurs moléculaires. *Le Radium* **1909**, 6 (12), 353–360.

(15) Mappes, T.; Jahr, N.; Csaki, A.; Vogler, N.; Popp, J.; Fritzsche, W. The Invention of Immersion Ultramicroscopy in 1912-The Birth of Nanotechnology? *Angew. Chem. Int. Ed.* **2012**, 51 (45), 11208–11212.

(16) Perrin, J. B. Discontinuous Structure of Matter, 1926.

(17) Sigal, Y. M.; Zhou, R.; Zhuang, X. Visualizing and Discovering Cellular Structures with Super-Resolution Microscopy. *Science* **2018**, 361 (6405), 880–887.

(18) Szymborska, A.; de Marco, A.; Daigle, N.; Cordes, V. C.; Briggs, J. A. G.; Ellenberg, J. Nuclear Pore Scaffold Structure Analyzed by Super-Resolution Microscopy and Particle Averaging. *Science* **2013**, 341, 655–658.

(19) Rösner, B.; Finizio, S.; Koch, F.; Döring, F.; Guzenko, V. A.; Langer, M.; Kirk, E.; Watts, B.; Meyer, M.; Loroña Ornelas, J.; Späth, A.; Stanescu, S.; Swaraj, S.; Belkhou, R.; Ishikawa, T.; Keller, T. F.; Gross, B.; Poggio, M.; Fink, R. H.; Raabe, J.; Kleibert, A.; David, C. Soft X-Ray Microscopy with 7 Nm Resolution. *Optica* **2020**, 7 (11), 1602.

(20) Kodur, M.; Kumar, R. E.; Luo, Y.; Cakan, D. N.; Li, X.; Stuckelberger, M.; Fenning, D. P. X-Ray Microscopy of Halide Perovskites: Techniques, Applications, and Prospects. *Adv Energy Mater* **2020**, 25.

(21) Ruska, E. The Development of the Electron Microscope and of Electron Microscopy. *Rev Mod Phys* **1987**, 59 (3), 24.

- (22) Sugimoto, Y.; Pou, P.; Abe, M.; Jelinek, P.; Perez, R.; Morita, S. Chemical Identification of Individual Surface Atoms by Atomic Force Microscopy. **2007**, *446*, 4.
- (23) Zhang, Y.; Li, S.-Y.; Huang, H.; Li, W.-T.; Qiao, J.-B.; Wang, W.-X.; Yin, L.-J.; Bai, K.-K.; Duan, W.; He, L. Scanning Tunneling Microscopy of the π Magnetism of a Single Carbon Vacancy in Graphene. *Phys. Rev. Lett.* **2016**, *117* (16), 166801.
- (24) Zheng, H.; Zhu, Y. Perspectives on in Situ Electron Microscopy. *Ultramicroscopy* **2017**, *180*, 188–196.
- (25) Vanrompay, H.; Bladt, E.; Albrecht, W.; Béch , A.; Zakhosheva, M.; S  nchez-Iglesias, A.; Liz-Marz  n, L. M.; Bals, S. 3D Characterization of Heat-Induced Morphological Changes of Au Nanostars by Fast *in Situ* Electron Tomography. *Nanoscale* **2018**, *10* (48), 22792–22801.
- (26) Dargusch, M.; Shi, X.-L.; Tran, X. Q.; Feng, T.; Somidin, F.; Tan, X.; Liu, W.; Jack, K.; Venezuela, J.; Maeno, H.; Toriyama, T.; Matsumura, S.; Pantelides, S. T.; Chen, Z.-G. *In Situ* Observation of the Continuous Phase Transition in Determining the High Thermoelectric Performance of Polycrystalline Sn_{0.98}Se. *J. Phys. Chem. Lett.* **2019**, *10* (21), 6512–6517.
- (27) Zhang, Y.; Zhang, Z.; Cheng, Y.; Cheng, F.; Wang, L.; Liu, N.; Li, L.; Su, J.; Gao, Y. In Situ TEM Observation of Controlled Growth of Two-Dimensional WS₂ with Vertically Aligned Layers and High-Temperature Stability. *Nano Energy* **2020**, *67*, 104221.
- (28) Yuan, Y.; Amine, K.; Lu, J.; Shahbazian-Yassar, R. Understanding Materials Challenges for Rechargeable Ion Batteries with in Situ Transmission Electron Microscopy. *Nat. Commun.* **2017**, *8* (1), 15806.
- (29) Spiecker, E.; Oh, S. H.; Shan, Z.-W.; Ikuhara, Y.; Mao, S. X. Insights into Fundamental Deformation Processes from Advanced in Situ Transmission Electron Microscopy. *MRS Bull.* **2019**, *44* (06), 443–449.

- (30) Wu, J.; Shan, H.; Chen, W.; Gu, X.; Tao, P.; Song, C.; Shang, W.; Deng, T. In Situ Environmental TEM in Imaging Gas and Liquid Phase Chemical Reactions for Materials Research. *Adv. Mater.* **2016**, *28* (44), 9686–9712.
- (31) Taheri, M. L.; Lagrange, T.; Reed, B. W.; Armstrong, M. R.; Campbell, G. H.; DeHope, W. J.; Kim, J. S.; King, W. E.; Masiel, D. J.; Browning, N. D. Laser-Based in Situ Techniques: Novel Methods for Generating Extreme Conditions in TEM Samples. *Microsc. Res. Tech.* **2009**, *72* (3), 122–130.
- (32) Loh, N. D.; Sen, S.; Bosman, M.; Tan, S. F.; Zhong, J.; Nijhuis, C. A.; Král, P.; Matsudaira, P.; Mirsaidov, U. Multistep Nucleation of Nanocrystals in Aqueous Solution. *Nat. Chem.* **2017**, *9* (1), 77–82.
- (33) Lee, S.-Y.; Wu, L.; Poyraz, A. S.; Huang, J.; Marschilok, A. C.; Takeuchi, K. J.; Takeuchi, E. S.; Kim, M.; Zhu, Y. Lithiation Mechanism of Tunnel-Structured MnO₂ Electrode Investigated by In Situ Transmission Electron Microscopy. *Adv. Mater.* **2017**, *29* (43), 1703186.
- (34) Li, Y.; Lu, J.; Cheng, X.; Shi, H.; Zhang, Y. Interfacial Lithiation Induced Leapfrog Phase Transformation in Carbon Coated Se Cathode Observed by In-Situ TEM. *Nano Energy* **2018**, *48*, 441–447.
- (35) Chee, S. W.; Arce-Ramos, J. M.; Li, W.; Genest, A.; Mirsaidov, U. Structural Changes in Noble Metal Nanoparticles during CO Oxidation and Their Impact on Catalyst Activity. *Nat. Commun.* **2020**, *11* (1), 2133.
- (36) Chee, S. W.; Anand, U.; Bisht, G.; Tan, S. F.; Mirsaidov, U. Direct Observations of the Rotation and Translation of Anisotropic Nanoparticles Adsorbed at a Liquid–Solid Interface. *Nano Lett.* **2019**, *19* (5), 2871–2878.

- (37) MacDonald, N. C.; Robinson, G. Y.; White, R. M. Time-Resolved Scanning Electron Microscopy and Its Application to Bulk-Effect Oscillators. *J. Appl. Phys.* **1969**, *40* (11), 4516–4528.
- (38) Plows, G. S.; Nixon, W. C. Stroboscopic Scanning Electron Microscopy. *J. Phys. [E]* **1968**, *1* (6), 595–600.
- (39) Durasova, U.; Kolotov, O.; Kolotov, I.; Petrov, V.; Spivak, G.; Telesnin, R. Investigation of Thin Magnetic Films Switching in Stroboscopic Transmission Electron Microscope. *IEEE Trans. Magn.* **1969**, *5* (3), 179–180.
- (40) Durasova, U. A.; Kolotov, I. S.; Kolotov, O. S.; Petrov, V. I.; Spivak, G. V.; Telesnin, R. V. Investigation of Incoherent Rotation in Thin Magnetic Films by Means of the Stroboscopic Electron Microscope. *Czechoslov. J. Phys.* **1971**, *21* (4–5), 451–453.
- (41) Takaoka, A.; Ura, K. Stroboscopic TEM with Time Resolution of 30 Ms. *J. Electron Microsc. (Tokyo)* **1983**, *5* (4), 299–304.
- (42) Bostanjoglo, O.; Heinrich, F. Producing High-Current Nanosecond Electron Pulses with a Standard Tungsten Hairpin Gun. *J. Phys. [E]* **1987**, *20* (12), 1491–1493.
- (43) Bostanjoglo, O.; Elschner, R.; Mao, Z.; Nink, T.; Weingärtner, M. Nanosecond Electron Microscopes. *Ultramicroscopy* **2000**, *81* (3–4), 141–147.
- (44) Dömer, H.; Bostanjoglo, O. High-Speed Transmission Electron Microscope. *Rev. Sci. Instrum.* **2003**, *74* (10), 4369–4372.
- (45) LaGrange, T.; Armstrong, M. R.; Boyden, K.; Brown, C. G.; Campbell, G. H.; Colvin, J. D.; DeHope, W. J.; Frank, A. M.; Gibson, D. J.; Hartemann, F. V.; Kim, J. S.; King, W. E.; Pyke, B. J.; Reed, B. W.; Shirk, M. D.; Shuttlesworth, R. M.; Stuart, B. C.; Torralva, B. R.; Browning, N. D. Single-Shot Dynamic Transmission Electron Microscopy. *Appl. Phys. Lett.* **2006**, *89* (4), 044105.

- (46) LaGrange, T.; Campbell, G. H.; Reed, B. W.; Taheri, M.; Pesavento, J. B.; Kim, J. S.; Browning, N. D. Nanosecond Time-Resolved Investigations Using the in Situ of Dynamic Transmission Electron Microscope (DTEM). *Ultramicroscopy* **2008**, *108* (11), 1441–1449.
- (47) LaGrange, T.; Reed, B. W.; Santala, M. K.; McKeown, J. T.; Kulovits, A.; Wiezorek, J. M. K.; Nikolova, L.; Rosei, F.; Siwick, B. J.; Campbell, G. H. Approaches for Ultrafast Imaging of Transient Materials Processes in the Transmission Electron Microscope. *Micron* **2012**, *43* (11), 1108–1120.
- (48) Sinha, S. K.; Khammari, A.; Picher, M.; Roulland, F.; Viart, N.; LaGrange, T.; Banhart, F. Nanosecond Electron Pulses in the Analytical Electron Microscopy of a Fast Irreversible Chemical Reaction. *Nat. Commun.* **2019**, *10* (1), 3648.
- (49) Lobastov, V. A.; Srinivasan, R.; Zewail, A. H. Four-Dimensional Ultrafast Electron Microscopy. *Proc. Natl. Acad. Sci.* **2005**, *102* (20), 7069–7073.
- (50) Barwick, B.; Park, H. S.; Kwon, O.-H.; Baskin, J. S.; Zewail, A. H. 4D Imaging of Transient Structures and Morphologies in Ultrafast Electron Microscopy. *Science* **2008**, *322* (5905), 1227–1231.
- (51) Spencer Baskin, J.; Zewail, A. H. Seeing in 4D with Electrons: Development of Ultrafast Electron Microscopy at Caltech. *Comptes Rendus Phys.* **2014**, *15* (2–3), 176–189.
- (52) Flannigan, D. J.; Park, S. T.; Zewail, A. H. Nanofriction Visualized in Space and Time by 4D Electron Microscopy. *Nano Lett.* **2010**, *10* (11), 4767–4773.
- (53) Park, H. S.; Baskin, J. S.; Zewail, A. H. 4D Lorentz Electron Microscopy Imaging: Magnetic Domain Wall Nucleation, Reversal, and Wave Velocity. *Nano Lett.* **2010**, *10* (9), 3796–3803.
- (54) Berruto, G.; Madan, I.; Murooka, Y.; Vanacore, G. M.; Pomarico, E.; Rajeswari, J.; Lamb, R.; Huang, P.; Kruchkov, A. J.; Togawa, Y.; LaGrange, T.; McGrouther, D.; Rønnow,

H. M.; Carbone, F. Laser-Induced Skyrmion Writing and Erasing in an Ultrafast Cryo-Lorentz Transmission Electron Microscope. *Phys. Rev. Lett.* **2018**, *120* (11), 117201.

(55) Rubiano da Silva, N.; Möller, M.; Feist, A.; Ulrichs, H.; Ropers, C.; Schäfer, S. Nanoscale Mapping of Ultrafast Magnetization Dynamics with Femtosecond Lorentz Microscopy. *Phys. Rev. X* **2018**, *8* (3), 031052.

(56) Fu, X.; Pollard, S. D.; Chen, B.; Yoo, B.-K.; Yang, H.; Zhu, Y. Optical Manipulation of Magnetic Vortices Visualized in Situ by Lorentz Electron Microscopy. *Sci. Adv.* **2018**, *4* (7), eaat3077.

(57) Möller, M.; Gaida, J. H.; Schäfer, S.; Ropers, C. Few-Nm Tracking of Current-Driven Magnetic Vortex Orbits Using Ultrafast Lorentz Microscopy. *Commun. Phys.* **2020**, *3* (1), 36.

(58) Houdellier, F.; Caruso, G. M.; Weber, S.; Hÿtch, M. J.; Gatel, C.; Arbouet, A. Optimization of Off-Axis Electron Holography Performed with Femtosecond Electron Pulses. *Ultramicroscopy* **2019**, *202*, 26–32.

(59) Cremons, D. R.; Du, D. X.; Flannigan, D. J. Picosecond Phase-Velocity Dispersion of Hypersonic Phonons Imaged with Ultrafast Electron Microscopy. *Phys. Rev. Mater.* **2017**, *1* (7), 073801.

(60) Lorenz, U. J.; Zewail, A. H. Biomechanics of DNA Structures Visualized by 4D Electron Microscopy. *Proc. Natl. Acad. Sci.* **2013**, *110* (8), 2822–2827.

(61) Lee, Y. M.; Kim, Y. J.; Kim, Y.-J.; Kwon, O.-H. Ultrafast Electron Microscopy Integrated with a Direct Electron Detection Camera. *Struct. Dyn.* **2017**, *4* (4), 044023.

(62) Kim, Y.-J.; Lee, Y.; Kim, K.; Kwon, O.-H. Light-Induced Anisotropic Morphological Dynamics of Black Phosphorus Membranes Visualized by Dark-Field Ultrafast Electron Microscopy. *ACS Nano* **2020**, *14* (9), 11383–11393.

- (63) Fitzpatrick, A. W. P.; Park, S. T.; Zewail, A. H. Exceptional Rigidity and Biomechanics of Amyloid Revealed by 4D Electron Microscopy. *Proc. Natl. Acad. Sci.* **2013**, *110* (27), 10976–10981.
- (64) Fitzpatrick, A. W. P.; Lorenz, U. J.; Vanacore, G. M.; Zewail, A. H. 4D Cryo-Electron Microscopy of Proteins. *J. Am. Chem. Soc.* **2013**, *135* (51), 19123–19126.
- (65) Kwon, O.-H.; Barwick, B.; Park, H. S.; Baskin, J. S.; Zewail, A. H. Nanoscale Mechanical Drumming Visualized by 4D Electron Microscopy. *Nano Lett.* **2008**, *8* (11), 3557–3562.
- (66) Flannigan, D. J.; Samartzis, P. C.; Yurtsever, A.; Zewail, A. H. Nanomechanical Motions of Cantilevers: Direct Imaging in Real Space and Time with 4D Electron Microscopy. *Nano Lett.* **2009**, *9* (2), 875–881.
- (67) Baskin, J. S.; Park, H. S.; Zewail, A. H. Nanomusical Systems Visualized and Controlled in 4D Electron Microscopy. *Nano Lett.* **2011**, *11* (5), 2183–2191.
- (68) Kim, Y.-J.; Jung, H.; Han, S. W.; Kwon, O.-H. Ultrafast Electron Microscopy Visualizes Acoustic Vibrations of Plasmonic Nanorods at the Interfaces. *Matter* **2019**, *1* (2), 481–495.
- (69) van der Veen, R. M.; Kwon, O.-H.; Tissot, A.; Hauser, A.; Zewail, A. H. Single-Nanoparticle Phase Transitions Visualized by Four-Dimensional Electron Microscopy. *Nat. Chem.* **2013**, *5* (5), 395–402.
- (70) Kwon, O.-H.; Zewail, A. H. 4D Electron Tomography. *Science* **2010**, *328* (5986), 1668–1673.
- (71) Park, S. T.; Flannigan, D. J.; Zewail, A. H. 4D Electron Microscopy Visualization of Anisotropic Atomic Motions in Carbon Nanotubes. *J. Am. Chem. Soc.* **2012**, *134* (22), 9146–9149.

- (72) Cao, G.; Sun, S.; Li, Z.; Tian, H.; Yang, H.; Li, J. Clocking the Anisotropic Lattice Dynamics of Multi-Walled Carbon Nanotubes by Four-Dimensional Ultrafast Transmission Electron Microscopy. *Sci. Rep.* **2015**, *5* (1), 8404.
- (73) Lobastov, V. A.; Weissenrieder, J.; Tang, J.; Zewail, A. H. Ultrafast Electron Microscopy (UEM): Four-Dimensional Imaging and Diffraction of Nanostructures during Phase Transitions. *Nano Lett.* **2007**, *7* (9), 2552–2558.
- (74) Park, S. T.; Flannigan, D. J.; Zewail, A. H. Irreversible Chemical Reactions Visualized in Space and Time with 4D Electron Microscopy. *J. Am. Chem. Soc.* **2011**, *133* (6), 1730–1733.
- (75) Danz, T.; Domröse, T.; Ropers, C. Ultrafast Nanoimaging of the Order Parameter in a Structural Phase Transition. *Science* **2021**, *371* (6527), 371–374.
- (76) Carbone, F.; Kwon, O.-H.; Zewail, A. H. Dynamics of Chemical Bonding Mapped by Energy-Resolved 4D Electron Microscopy. *Science* **2009**, *325* (5937), 181–184.
- (77) Piazza, L.; Ma, C.; Yang, H. X.; Mann, A.; Zhu, Y.; Li, J. Q.; Carbone, F. Ultrafast Structural and Electronic Dynamics of the Metallic Phase in a Layered Manganite. *Struct. Dyn.* **2014**, *1* (1), 014501.
- (78) Zheng, D.; Zhu, C.; Li, Z.; Li, Z.; Li, J.; Sun, S.; Zhang, Y.; Wang, F.; Tian, H.; Yang, H.; Li, J. Ultrafast Lattice and Electronic Dynamics in Single-Walled Carbon Nanotubes. *Nanoscale Adv.* **2020**, *2* (7), 2808–2813.
- (79) Barwick, B.; Flannigan, D. J.; Zewail, A. H. Photon-Induced near-Field Electron Microscopy. *Nature* **2009**, *462* (7275), 902–906.
- (80) Park, S. T.; Lin, M.; Zewail, A. H. Photon-Induced near-Field Electron Microscopy (PINEM): Theoretical and Experimental. *New J. Phys.* **2010**, *12* (12), 123028.

- (81) García de Abajo, F. J.; Asenjo-Garcia, A.; Kociak, M. Multiphoton Absorption and Emission by Interaction of Swift Electrons with Evanescent Light Fields. *Nano Lett.* **2010**, *10* (5), 1859–1863.
- (82) Liu, H.; Baskin, J. S.; Zewail, A. H. Infrared PINEM Developed by Diffraction in 4D UEM. *Proc. Natl. Acad. Sci.* **2016**, *113* (8), 2041–2046.
- (83) Hassan, M. T.; Liu, H.; Baskin, J. S.; Zewail, A. H. Photon Gating in Four-Dimensional Ultrafast Electron Microscopy. *Proc. Natl. Acad. Sci.* **2015**, *112* (42), 12944–12949.
- (84) Feist, A.; Echtenkamp, K. E.; Schauss, J.; Yalunin, S. V.; Schäfer, S.; Ropers, C. Quantum Coherent Optical Phase Modulation in an Ultrafast Transmission Electron Microscope. *Nature* **2015**, *521* (7551), 200–203.
- (85) Fransen, M. J. Experimental Evaluation of the Extended Schottky Model for ZrO/W Electron Emission. *J. Vac. Sci. Technol. B Microelectron. Nanometer Struct.* **1998**, *16* (4), 2063.
- (86) Kim, H. S. Performance of Zr/O/W Schottky Emitters at Reduced Temperatures. *J. Vac. Sci. Technol. B Microelectron. Nanometer Struct.* **1997**, *15* (6), 2284.
- (87) Muller, D. A. Structure and Bonding at the Atomic Scale by Scanning Transmission Electron Microscopy. *Nat. Mater.* **2009**, *8* (4), 263–270.
- (88) Midgley, P. A.; Dunin-Borkowski, R. E. Electron Tomography and Holography in Materials Science. *Nat. Mater.* **2009**, *8* (4), 271–280.
- (89) Otani, S.; Hiraoka, H.; Ide, M.; Ishizawa, Y. Thermionic Emission Properties of Rare-Earth-Added LaB₆ Crystal Cathodes. *J. Alloys Compd.* **1992**, *189* (1), L1–L3.
- (90) Cook, B.; Verduin, T.; Hagen, C. W.; Kruit, P. Brightness Limitations of Cold Field Emitters Caused by Coulomb Interactions. *J. Vac. Sci. Technol. B Nanotechnol. Microelectron. Mater. Process. Meas. Phenom.* **2010**, *28* (6), C6C74–C6C79.

- (91) Piazza, L.; Masiel, D. J.; LaGrange, T.; Reed, B. W.; Barwick, B.; Carbone, F. Design and Implementation of a Fs-Resolved Transmission Electron Microscope Based on Thermionic Gun Technology. *Chem. Phys.* **2013**, *423*, 79–84.
- (92) Feist, A.; Bach, N.; Rubiano da Silva, N.; Danz, T.; Möller, M.; Priebe, K. E.; Domröse, T.; Gatzmann, J. G.; Rost, S.; Schauss, J.; Strauch, S.; Bormann, R.; Sivilis, M.; Schäfer, S.; Ropers, C. Ultrafast Transmission Electron Microscopy Using a Laser-Driven Field Emitter: Femtosecond Resolution with a High Coherence Electron Beam. *Ultramicroscopy* **2017**, *176*, 63–73.
- (93) Ji, S.; Piazza, L.; Cao, G.; Park, S. T.; Reed, B. W.; Masiel, D. J.; Weissenrieder, J. Influence of Cathode Geometry on Electron Dynamics in an Ultrafast Electron Microscope. *Struct. Dyn.* **2017**, *4* (5), 054303.
- (94) Plemmons, D. A.; Flannigan, D. J. Ultrafast Electron Microscopy: Instrument Response from the Single-Electron to High Bunch-Charge Regimes. *Chem. Phys. Lett.* **2017**, *683*, 186–192.
- (95) Houdellier, F.; Caruso, G. M.; Weber, S.; Kociak, M.; Arbouet, A. Development of a High Brightness Ultrafast Transmission Electron Microscope Based on a Laser-Driven Cold Field Emission Source. *Ultramicroscopy* **2018**, *186*, 128–138.
- (96) Picher, M.; Bucker, K.; LaGrange, T.; Banhart, F. Imaging and Electron Energy-Loss Spectroscopy Using Single Nanosecond Electron Pulses. *Ultramicroscopy* **2018**, *188*, 41–47.
- (97) Zhu, C.; Zheng, D.; Wang, H.; Zhang, M.; Li, Z.; Sun, S.; Xu, P.; Tian, H.; Li, Z.; Yang, H.; Li, J. Development of Analytical Ultrafast Transmission Electron Microscopy Based on Laser-Driven Schottky Field Emission. *Ultramicroscopy* **2020**, *209*, 112887.
- (98) Wang, K.; Dahan, R.; Shentis, M.; Kauffmann, Y.; Ben Hayun, A.; Reinhardt, O.; Tsesses, S.; Kaminer, I. Coherent Interaction between Free Electrons and a Photonic Cavity. *Nature* **2020**, *582* (7810), 50–54.

- (99) Zandi, O.; Sykes, A. E.; Cornelius, R. D.; Alcorn, F. M.; Zerbe, B. S.; Duxbury, P. M.; Reed, B. W.; van der Veen, R. M. Transient Lensing from a Photoemitted Electron Gas Imaged by Ultrafast Electron Microscopy. *Nat. Commun.* **2020**, *11* (1), 3001.
- (100) Caruso, G. M.; Houdellier, F.; Weber, S.; Kociak, M.; Arbouet, A. High Brightness Ultrafast Transmission Electron Microscope Based on a Laser-Driven Cold-Field Emission Source: Principle and Applications. *Adv. Phys. X* **2019**, *4* (1), 1660214.
- (101) Yang, J.; Yoshida, Y.; Yasuda, H. Ultrafast Electron Microscopy with Relativistic Femtosecond Electron Pulses. *Microscopy* **2018**, *67* (5), 291–295.
- (102) Yang, J.; Yoshida, Y. Relativistic Ultrafast Electron Microscopy: Single-Shot Diffraction Imaging with Femtosecond Electron Pulses. *Adv. Condens. Matter Phys.* **2019**, *2019*, 1–6.

Chapter 2

Characterization of a Time-Resolved Electron Microscope with a Schottky Field Emission Gun

Introduction*

Time-resolved electron microscopy has proven a powerful tool for the study of the fast dynamics of nanoscale systems. The versatility of the technique is underlined by the vast range of phenomena that have been investigated, including mechanics,^{1–5} fluid dynamics,⁶ phase transitions,^{7,8} chemical reactions,^{9–11} the dynamics of magnetic structures,¹² or the visualization of optical near fields.¹³ The various implementations of the technique have in common that sample dynamics are initiated *in situ* with a fast trigger, which are then probed at a well-defined point in time with a short electron pulse, such as to capture an image, diffraction pattern, or energy loss spectrum. In such a pump-probe experiment, the time resolution is no longer determined by the speed of the electron camera, but instead by the duration of the sample excitation pulse and the electron probe pulse. Crucially, the temporal resolution of time-resolved electron microscopy can thus be matched to the inherent timescale of atomic-scale motions in a wide range of processes, from microseconds to femtoseconds and even attoseconds.^{14–16}

Along with the increasing interest in time-resolved electron microscopy, the development of instruments has been burgeoning, and a range of new technologies are being pursued to improve their operation. This includes different approaches of generating electron

* Reproduced from Olshin P.K., Drabbels M., Lorenz U. J., *Struct. Dyn.* **7**, 054304 (2020), with the permission of AIP Publishing

Authors Contributions: P.K.O. performed the experiments and analyzed the data; M.D. and U.J.L. supervised the project; U.J.L. wrote the manuscript with the contribution from all authors.

pulses, either through photoemission from the filament through illumination with a short laser pulse, or by chopping a continuous electron beam into pulses with a beam blanker,¹⁷ located either before^{18–20} or after the sample.^{21,22} Another active area of development is the generation of ultrafast electron pulses with high bunch charges, either through pulse compression with radio frequency cavities^{23–26} and THz laser pulses,²⁷ or by accelerating electrons to MeV energies.^{28,29} The importance of the choice of the electron source has also come into focus as it crucially determines the properties of the electron pulses. While flat metal photocathodes and LaB₆ emitters are most widely used,^{30–35} field emitters have recently begun to advance novel types of time-resolved experiments.^{21,22,36–38} Their high brightness and coherence,^{39–43} which makes them the electron source of choice in most high-performance transmission electron microscopes, have enabled time-resolved electron holography experiments^{36,44,45} and have greatly advanced time-resolved experiments with fine electron probes.^{14,15} Moreover, they stand to significantly benefit time-resolved imaging at atomic resolution.^{17,46} At the same time however, the small source size of field emitters also limits the number of electrons that can be extracted in a pulse, putting them at a disadvantage for applications in which the number of electrons is a critical figure of merit. For example, in a single-shot experiment, in which an irreversible process has to be captured with just a single electron pulse,^{30,31} the crucial challenge frequently lies in overcoming the shot noise. Clearly, if the available number of electrons is insufficient, capturing an event becomes unfeasible, no matter the brightness of the pulse. Such experiments are therefore typically performed with pulses containing millions of electrons^{28,31,47} that are generated through photoemission from flat emitters.

Here we describe a straightforward design of a time-resolved transmission electron microscope with a Schottky field emission gun^{48–50} that offers operation both with high-brightness electron pulses from the emitter tip and with pulses containing a large number of electrons, as if the microscope was equipped with a flat photocathode. We provide details of

our design, in which the emitter is illuminated under a small angle with respect to the electron optical axis, and demonstrate that it affords a high spatial, temporal, and energy resolution as well as a high transverse brightness in pulsed operation. The geometry of our electron gun also allows us to create photoelectron pulses from the surface of the extractor instead of the emitter. We demonstrate that it is thus possible to extract vastly larger numbers of electrons per pulse and thus effectively trade brightness for electron counts, depending on the desired application.⁴⁹

Experimental setup

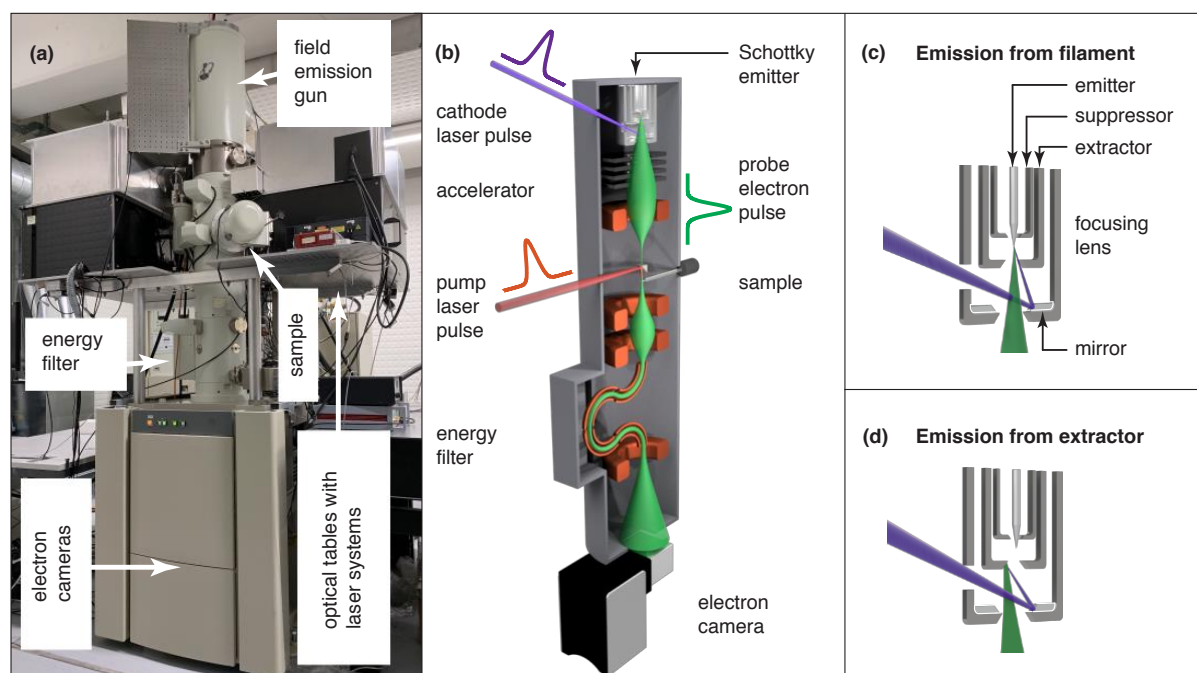


Figure 2-1. Overview of the time-resolved electron microscope. (a) Photograph of the JEOL 2200FS transmission electron microscope in the laboratory. (b) Sketch of the modified instrument. (c) Illustration of the modified Schottky emitter assembly. Photoelectron pulses of high brightness are generated by illuminating the tip of the emitter with UV laser pulses. (d) Pulses with large numbers of electrons are obtained by illuminating the extractor.

Figure 2-1 provides an overview of our modified JEOL JEM-2200FS transmission electron microscope, with a photograph in Fig. 2-1(a) and a schematic of the operating principle in Fig. 2-1(b). The remote operated microscope is equipped with a 200 kV Schottky field emission gun and an in-column Omega-type energy filter. A scintillator based electron camera (Gatan Ultrascan 4000) was used to record the majority of the data in this manuscript, while the high resolution image in Fig. 2-2(a) was acquired with a direct electron detector (Gatan K3). As shown in the photograph of Fig. 2-1(a), we mounted the entire laser system

directly onto the microscope. This allows us to minimize the beam paths and use the same vibration damping system for the microscope and the lasers, so that more stable operation can be achieved.³⁴ In order to provide sufficient space for the lasers and optics, we mounted two levels of breadboards on either side of the column. In the photograph, the optical setup is hidden behind enclosures that protect it from dust. The output of a femtosecond laser (Light Conversion Pharos, 190 fs laser pulses at 1032 nm, up to 1 MHz repetition rate) is doubled to excite the sample (516 nm, 160 fs), while the fourth harmonic (258 nm) is used to illuminate the emitter and create ultrafast photoelectron pulses. In order to access longer timescales, we generate nanosecond electron pulses with an Innolas Picolo 50 MOPA (1 ns pulses at 266 nm, up to 50 kHz repetition rate). Here, the ultrafast and nanosecond experiments were performed at 100 kHz and 20 kHz repetition rate, respectively.

Figure 2-1(b) illustrates the operating principle of the time-resolved electron microscope. Sample dynamics are initiated *in situ* with a pump laser pulse,⁴⁸ which is directed at the sample by means of an aluminum mirror that is mounted above the upper pole piece of the objective lens (Integrated Dynamic Electron Solutions) and that steers the laser beam straight down, so that it propagates almost collinearly with the electron beam.⁵¹ A 250 mm lens focuses the laser beam to a spot size of 24 μm full width at half maximum (FWHM) in the sample plane, as determined by a knife edge scan. In order to generate probe electron pulses, we cool the emitter to about 1100-1300 K, so that the continuous emission current becomes negligible, and illuminate the tip of the Schottky emitter with UV laser pulses. The resulting photoelectron pulses are accelerated to 160 keV, interact with the sample, and after passing the energy filter, are detected by the electron camera. Since our electron gun is a refurbished model, we currently limit its accelerating voltage to 160 kV. However, we note that we have since modified an identical field emission gun that we are operating at 200 kV on a JEOL JEM-2010F.⁵⁰

In order to generate photoelectron pulses, the emitter is illuminated through a viewport on the side of the gun that ordinarily serves for electron beam monitoring purposes. As illustrated in Fig. 2-1(c), the laser beam enters the emitter assembly through a hole in the electrostatic focusing lens.⁵⁰ It is reflected by an aluminum mirror and strikes the tip of the Schottky emitter (York Probe Sources, 400 nm tip radius) under an angle of 16 degrees with respect to the electron optical axis. The laser beam is focused onto the emitter by means of 125 mm lens which is located within the vacuum chamber of the gun. We typically apply +4 kV to the extractor (680 μ m aperture), and bias the suppressor to -300 V with respect to the emitter, while the focusing lens is operated at +6.0 kV.⁵⁰ While illuminating the emitter allows us to generate high brightness electron pulses, the small source size also limits the number of electrons that can be extracted per pulse. Alternatively, we can create photoelectrons by directing the UV laser at the extractor [Fig. 2-1(d)]. The source size can then be adjusted by changing the spot size of the laser, which we can focus as tightly as 25 μ m FWHM. In this configuration, the gun essentially operates as if equipped with a flat photocathode or thermionic emitter, with the larger source size resulting in a vastly greater number of electrons per pulse, albeit at lower brightness. Here, we operate with the original extractor, which is made of stainless steel. In our second instrument, we have replaced it with an extractor machined out of copper, a more frequently used photocathode material.^{52,53}

Results and discussions

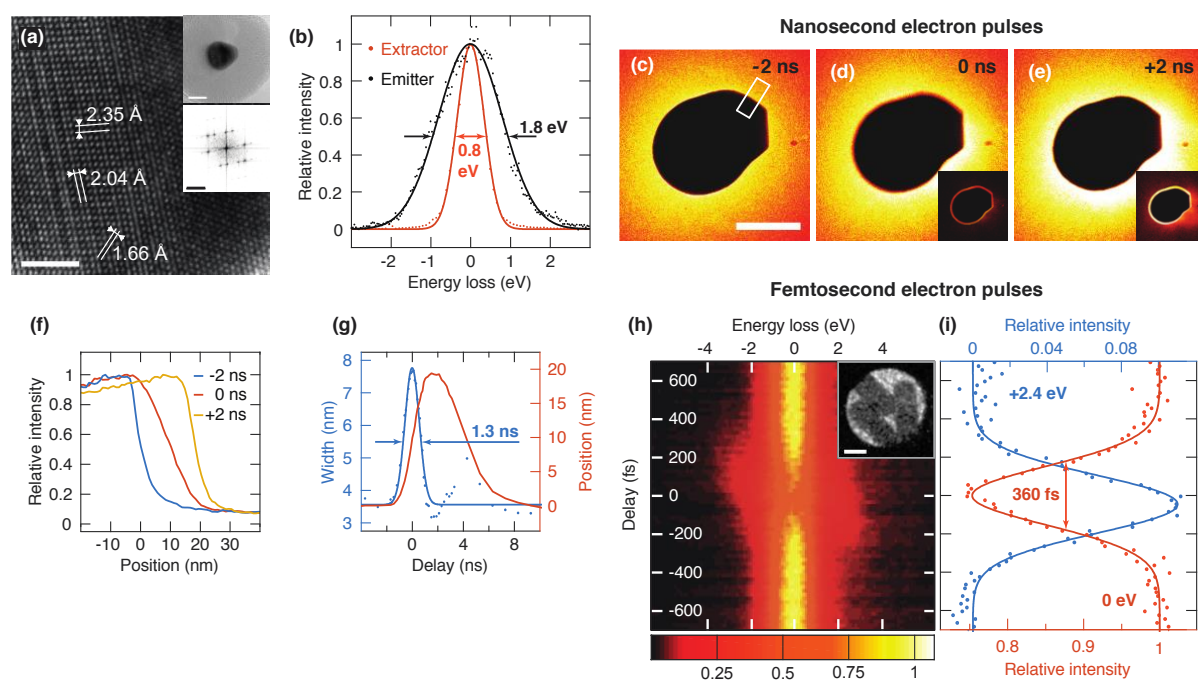


Figure 2-2. Characterization of the spatial, energy, and temporal resolution. (a) High resolution image of the core of the gold-core silica-shell nanoparticle shown in the top inset. The bottom inset displays the corresponding diffractrogram. Scale bar, 2 nm (10 nm and 5 nm⁻¹ in the insets). (b) Energy distribution of photoelectrons from the filament and the extractor. Gaussian fits (solid lines) yield a FWHM of 1.8 eV and 0.8 eV, respectively. (c-e) Determination of the duration of nanosecond electron pulses, images were recorded with 10 seconds acquisition time. (c) Images of a gold nanoparticle under irradiation with a femtosecond laser pulse for different time delays. The insets display the difference with the image at negative time delay. Scale bar, 100 nm. (f) Intensity profiles of the boundary of the particle for different time delays, calculated from the area marked in (c). (g) The width and center position of the particle boundary are determined from a fit with an error function and displayed as a function of time. A Gaussian fit of the width yields an electron pulse duration of 1.3 ns. (h, i) Determination of

the duration of femtosecond electron pulses. (h) Temporal evolution of the energy loss spectra collected from an ensemble of gold nanorods (inset) under femtosecond laser irradiation (average of 10 scans with 30 seconds acquisition time for each spectrum). Scale bar of the inset, 50 nm. (i) Relative intensity of the zero loss peak (0 eV, red) and of a sideband (+2.4 eV, blue) as a function of time (2 eV integration window). Gaussian fits (solid lines) yield a FWHM of 360 fs, corresponding to an electron pulse duration of 320 fs.

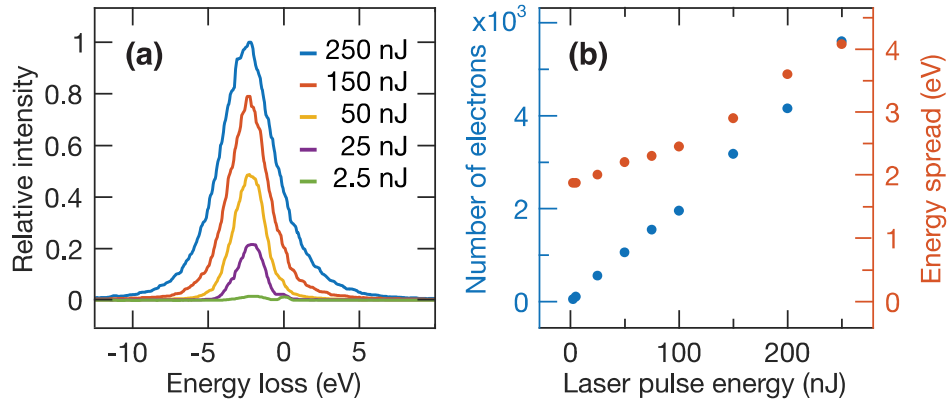
We begin by characterizing the spatial, energy, and temporal resolution of the time-resolved electron microscope. Figure 2-2(a) shows a high-resolution micrograph of the gold core of a silica-shell gold-core nanoparticle (top inset, 20 nm core diameter and 20 nm shell thickness) that was recorded with a continuous electron beam. The visibility of lattice fringes (see also the diffractogram in the bottom inset) demonstrates that our modifications have not deteriorated resolving power of the instrument. Figure 2-2(b) shows energy loss spectra of nanosecond photoelectron pulses that were obtained by illuminating either the emitter (black dots) or the extractor (red dots). Gaussian fits (solid lines) yield a FWHM of 1.8 eV and 0.8 eV, respectively. The difference in energy spread results from the difference in work function of the emitting surface. While the work function of the stainless steel surface of the extractor⁵⁴ closely matches the photon energy (4.8 eV), the zirconium oxide coated tungsten emitter has a work function of only 2.8 eV.⁵⁵ Therefore, photoelectrons are emitted with considerable excess energy, which leads to the larger energy spread.⁵⁶

We characterize the temporal resolution for experiments with nanosecond electron pulses by making use of the transient electric field effect.^{35,57,58} Figure 2-2(c) shows a 200 nm diameter gold particle on a multilayer graphene substrate, imaged with nanosecond electron pulses from the emitter. Under irradiation with a femtosecond laser pulse, the sample emits a cloud of electrons, which deflects the probe electrons, so that images recorded at zero time

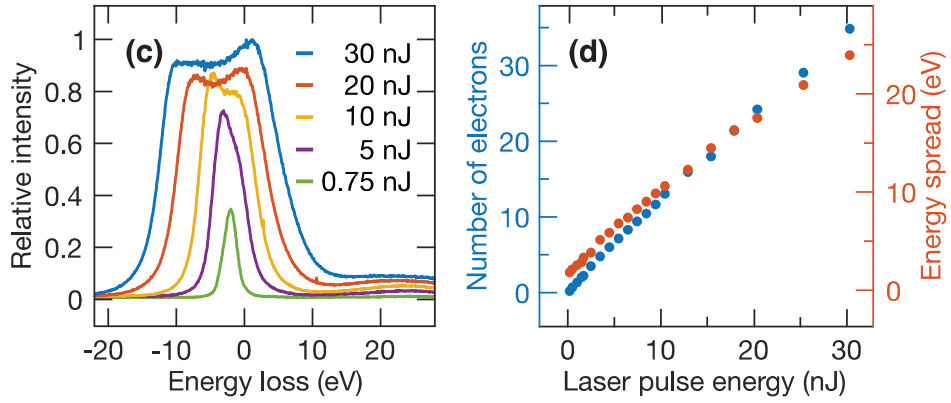
delay or at small positive times appear distorted [Fig. 2-2(d,e)]. This is highlighted by the difference images displayed in the insets, which are obtained by subtracting the image at negative time delay [Fig. 2-2(c)]. To analyze the observed image distortions, we calculate intensity profiles across the particle border [Fig. 2-2(c), white rectangle], which reveal that the boundary shifts with time and that it broadens around time zero [Fig. 2-2(f)]. By fitting with an error function, we determine the position and the width of the particle edge as a function of time delay [Fig. 2-2(g), red line and blue dots, respectively]. The blurring of the particle boundary arises as the emergence of the electron cloud deflects the probe electron pulse,^{35,57,58} a process that occurs on a picosecond timescale, much faster than the duration of the electron pulse. We can therefore use this blurring to estimate the electron pulse duration, for which we obtain 1.3 ns from a fit of the boundary width with a Gaussian function (blue solid line).

We determine the femtosecond electron pulse duration through cross correlation of the electron and laser pulse.^{13,59} To this end, we use the fact that probe electrons interact inelastically with the scattered near-fields of a nanostructure under laser illumination, causing the electrons to gain or lose energy in multiples of the photon energy. Figure 2-2(h) displays the evolution of the energy loss spectrum of three gold nanorods (inset) under illumination with the pump laser (15 nJ pulse energy) as a function of time delay. When the electron and laser pulse overlap in time, the intensity of the zero loss peak decreases, while sidebands at ± 2.4 eV, the photon energy, appear. Figure 2-2(i) shows the evolution of the intensity of the zero loss peak (red dots) and the side band at +2.4 eV (blue dots). From Gaussian fits (solid lines), we extract a FWHM of the interaction time of 360 fs, which yields an electron pulse duration of 320 fs. We note that in this measurement, we have reduced the number of electrons to less than one per pulse (as counted in the sample plane without a condenser lens aperture inserted) in order to obtain the shortest pulse duration. The effects of space charge on the electron pulse properties are described in the following.

Nanosecond electron pulses from filament



Ultrafast electron pulses from filament



Ultrafast electron pulses from extractor

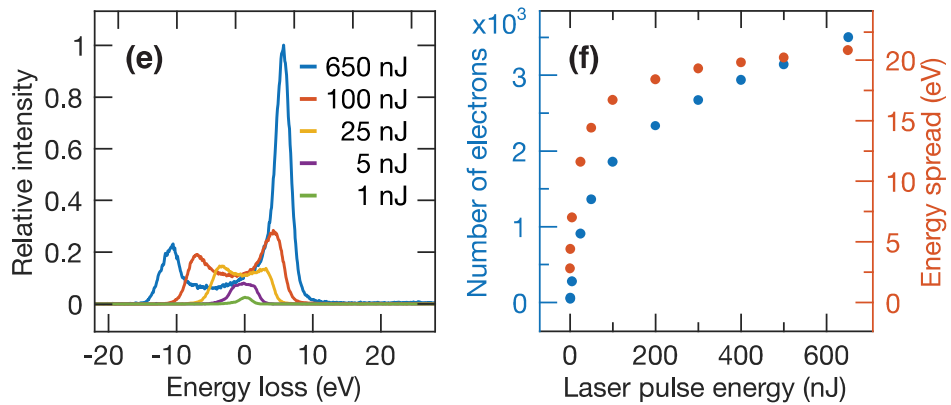


Figure 2-3. Characterization of electron pulses with high charge densities. Energy loss spectra are shown together with the electron yield and the energy spread as a function of laser pulse

energy for (a, b) nanosecond electron pulses from the emitter, each spectrum was recorded 3 times with the exposure time varied from 2 to 30 seconds for different laser powers and averaged, (c, d) ultrafast electron pulses from the emitter (the exposure times were 10 or 20 seconds), and (e, f) ultrafast electron pulses from the extractor, the spectra were recorded with different acquisition times from 20 to 300 seconds. The number of electrons is determined in the sample plane (without condenser lens aperture inserted). The energy spread is measured as the FWHM of the distribution. For distributions featuring two maxima, we report the full width at half the height of the smaller maximum.

In Fig. 2-3, we characterize the generation of pulses with high charge densities, which is of particular relevance for applications in which the available number of electrons is the most important figure of merit. We begin by studying the evolution of the energy loss spectra for nanosecond electron pulses from the emitter as a function of the pulse energy of the cathode laser [Fig. 2-3(a)]. With increasing pulse energy, the number of photoelectrons per pulse grows, and the increasing space charge repulsion within the electron packet broadens its energy distribution.⁶⁰ We note that due to the excess energy with which the photoelectrons are emitted, their energy distribution is shifted by about 2 eV with respect to that of the continuous electron beam.^{61,62} This is evident in the spectra recorded at low pulse energies, which exhibit some residual continuous emission that is apparent as a second peak centered at 0 eV. As shown in Fig. 2-3(b), we find that the number of electrons per pulse increases linearly with the laser pulse energy (blue dots) and reaches over 5000 in the sample plane (no condenser lens aperture) at 250 nJ, while the FWHM energy spread increases from 2 eV to 4 eV (red dots).

Ultrafast electron pulses from the filament are even more strongly affected by space charge [Fig. 2-3(c,d)]. As we raise the laser pulse energy to 30 nJ, which increases the number of electrons per pulse to 35, the energy spread reaches almost 25 eV [Fig. 2-3(d)], with the

energy distribution featuring a characteristic double peak structure [Fig. 2-3(c)].^{60,63,64} Evidently, the number of electrons per pulse can only be increased significantly by sacrificing the energy resolution. Moreover, the larger energy spread of the electrons couples to the chromatic aberration of the electron optical system. It also broadens the arrival time distribution of the electrons at the sample, thus increasing the electron pulse duration and lowering the time resolution of the experiment to several picoseconds, as we will discuss in more detail below.

Significantly larger numbers of electrons per pulse with a comparable energy spread can be obtained by illuminating the surface of the extractor electrode instead of the tip of the emitter [Fig. 2-3(e,f)]. The number of electrons emitted from the extractor initially increases rapidly with the laser pulse energy, but begins to level off above 100 nJ, finally reaching 3500 electrons at 650 nJ [Fig. 2-3(f), blue dots]. The energy spread increases to 20 eV at 200 nJ pulse energy, after which it grows only marginally (red dots). For large numbers of electrons per pulse, the energy loss spectra feature a pronounced double peak structure [Fig. 2-3(e)]. For pulses of such high bunch charge, the pulse duration stretches to several tens of picoseconds.

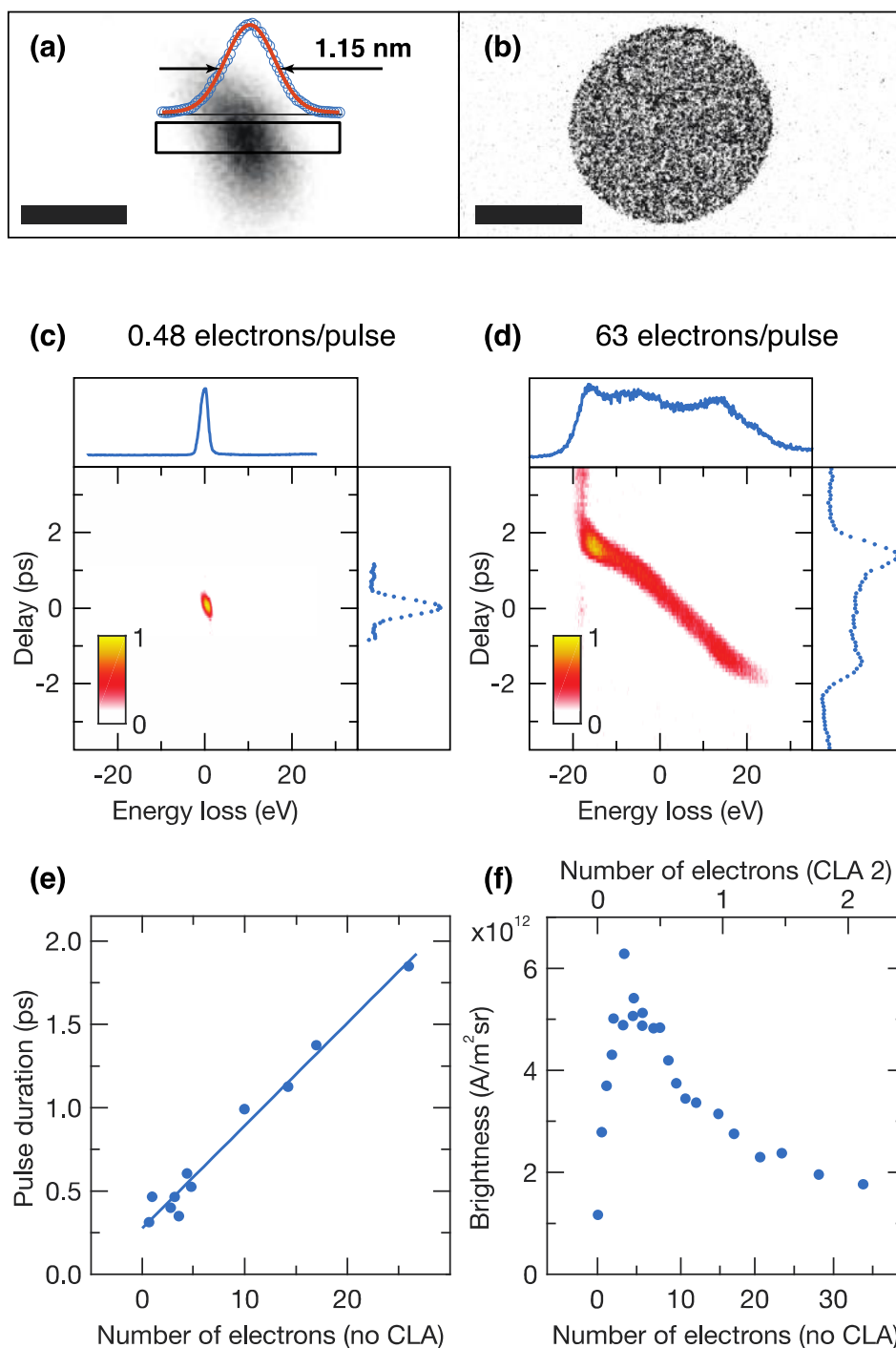


Figure 2-4. Determination of the brightness for ultrafast electron pulses. (a) Image of the converged electron beam (convergent beam electron diffraction mode) with a spot size of 1.15 nm, as determined from a Gaussian fit (red line) of an intensity profile (blue dots) of the area marked with a black rectangle. Scale bar, 2 nm. (b) Diffraction pattern of the converged electron beam. Scale bar, 2 mrad. (c, d) Time-energy distributions of electron pulses with 0.48

and 63 electrons per pulse, respectively. The projections of the pulses into the time and energy domains are presented on the top and on the right, respectively. (e) Pulse duration as a function of the number of electrons per pulse (spot size 1, α 3, no condenser lens aperture [CLA] inserted). For pulses with two maxima in the time domain, we report the full width at half the height of the smaller maximum. A linear fit serves as a guide for the eye. (f) Brightness as a function of the number of electrons per pulse (spot size 1, α 3, CLA 2). The brightness is measured with the second condenser lens aperture inserted, which reduces the number of electrons in the sample plane by a factor of about 15. For easy comparison with (e), we report the number of electrons without condenser lens aperture inserted on the bottom axis and the actual number of electrons on the top axis.

Finally, we demonstrate that our gun design achieves a brightness that is comparable to that of other time-resolved field emission gun microscopes. The transverse brightness of the electron beam can be conveniently determined at a beam waist, which can be formed by focusing the electron beam in the sample plane.¹⁹ In such a configuration, the instantaneous brightness B of the electron pulse can then be obtained as the instantaneous probe current $Ne/\Delta t$ per surface area element πr^2 and solid angle $\pi\alpha^2$

$$B = \frac{Ne/\Delta t}{\pi^2 r^2 \alpha^2}$$

where N is the number of electrons per pulse, e the electron charge, Δt the pulse duration, r the spot radius, and α the convergence semi-angle of the beam. To illustrate the measurement principle, Fig. 2-4(a) shows a micrograph of the focused electron beam, with the microscope operated in convergent beam electron diffraction mode. From an intensity profile (blue circles) of the area marked with a black rectangle, we obtain a FWHM spot size of $2r = 1.15$ nm, as

determined from a fit with a Gaussian (red line). The spot can be seen to be slightly asymmetric. In the following, we therefore determine the spot radius according to $r = \sqrt{r_x r_y}$, with r_x and r_y the semi-axes of the ellipse. The diffraction pattern corresponding to the beam in (a) is displayed in Fig. 2-4(b), from which we determine a convergence semi-angle α of 3.7 mrad. The acquisition time of the images in Fig. 2-4 (a,b) was 120 seconds.

Figure 2-4(c,d) illustrates the determination of the electron pulse duration from time-energy profiles. These are obtained by recording energy loss spectra of the inelastic electron-photon interactions at a nanostructure under laser illumination [*e.g.* Fig. 2-2(h)] and plotting difference spectra as a function of time. The spectra were recorded with the exposure times of 20 and 15 seconds in Figure 2-4(c) and Figure 2-4(d), respectively. Projections of the pulses into the energy and time domain are shown on top of the figure and on its right, respectively. The shortest pulse durations and most narrow energy distribution are obtained for pulses with a small number of electrons. For example, in Fig. 2-4(c), pulses containing 0.48 electrons on average (counted in the sample plane) yield a duration of 410 fs and an energy spread of 2.1 eV FWHM. For large numbers of electrons per pulse, space charge repulsion broadens both distributions, as shown in Fig. 2-4(d) for pulses with 63 electrons on average, which have a pulse duration of 3800 fs and an energy spread of 39.4 eV. Such pulses possess a distinct shape in the time-energy distribution with a large central portion that has a constant chirp as well as smaller wings. Figure 2-4(e) shows that the pulse duration that we extract from the time-energy diagrams increases linearly with the number of electrons per pulse. For pulses with two maxima in the time domain, such as in Fig. 2-4(d), we report the pulse length as the full width at half the height of the smaller maximum.

With the above determined quantities, we calculate the instantaneous brightness as a function of the number of electrons per pulse [Fig. 2-4(f)]. Here, the brightness is measured with the second condenser lens aperture inserted, which reduces the number of electrons in the

sample by about a factor of 15. For easy comparison with Fig. 2-4(e), we report the number of electrons that would be obtained without condenser lens aperture on the bottom axis and the actual number of electrons on the top axis. The brightness initially increases linearly with the number of electrons, but begins to level off as electron-electron interactions become more frequent, causing the spot size to grow and the pulse duration to increase. The brightness reaches a maximum value of $6.3 \cdot 10^{12}$ A/(m²sr) at 0.23 electrons per pulse (in the sample plane) before decreasing again for even larger numbers of electrons. This behavior resembles that of continuous electron beams from field emitters, whose brightness initially grows with increasing emission current, but then levels off as electron-electron interactions become more frequent⁶⁵ and finally goes through a maximum.⁶⁶ Typical values for the instantaneous brightness are given in Table 2-1 for different operating parameters of the microscope. Notably, the instantaneous brightness of the femtosecond electron pulses is higher than that of our continuous electron beam (Table 2-1, first line) and similar to that of side-illuminated field emitters.^{36,37} The brightness can be further increased by raising the accelerating voltage to 200 kV, as we have done on our second time-resolved instrument, choosing a smaller emitter size, and matching the photon energy of the cathode laser more closely to the work function of the emitter. Table 2-1 also includes a brightness measurement for electron pulses generated from the extractor. While the larger emission area on the extractor allows us to obtain higher photocurrents than from the small tip of the emitter [Fig. 2-3(f)], the larger source size also inevitably reduces the brightness of the beam by more than two orders of magnitude.¹⁷

Table 2-1. Brightness of the photoelectron pulses for different operating parameters. For a given laser pulse energy, settings of the condenser lens system (Spot size and Alpha), and condenser lens aperture number (CLA), the table lists the number of electrons per pulse in the sample plane (N), the pulse duration (Δt), the instantaneous probe current (I), the FWHM of the focused electron beam (d), the convergence semi-angle (α), and the instantaneous brightness (B). Unless otherwise noted, electron pulses are generated by illuminating the emitter. For the duration of the nanosecond electron pulses, we assume 1 ns, the duration of the cathode laser pulses.

Laser pulse energy and duration	Spot size	Alpha	CLA	N	Δt (ps)	I (nA)	d (nm)	α (mrad)	B (A/m ² sr)
Continuous beam	5	3	3	–	–	0.105	1.8	3.7	$9.0 \cdot 10^{11}$
30 nJ, fs	5	3	3	0.026	0.45	9.3	7.3	3.7	$5.1 \cdot 10^{12}$
2 nJ, fs	1	3	2	0.23	0.48	76	7.5	9.3	$6.3 \cdot 10^{12}$
10 nJ, fs	1	3	2	0.79	0.83	117	12.8	9.3	$3.3 \cdot 10^{12}$
30 nJ, fs	1	3	2	2.05	1.90	143	19.5	9.3	$1.8 \cdot 10^{12}$
300 nJ, ns	1	3	2	219	1000	35	10.1	9.3	$1.6 \cdot 10^{12}$
150 nJ, ns (Extractor)	1	3	2	111	1000	17.7	133	9.3	$4.7 \cdot 10^9$

Conclusion

We expect that our straightforward design of a time-resolved transmission electron microscope with a field emission gun will facilitate the adoption of these instruments, which are more challenging to modify and operate, but are opening up new possibilities for studying the fast dynamics of nanoscale systems. We demonstrate that our design with a front-illuminated emitter achieves a high spatial, energy, and temporal resolution as well as a brightness that is similar to that of designs in which the emitter is illuminated from the side. Alternatively, the instrument can be operated as if it was equipped with a flat photocathode by creating photoelectrons from the extractor instead of the emitter tip. It thus becomes possible to trade brightness for counts, if this is advantageous for a given application. In our lab, we can switch between both operating modes within minutes, thanks to an optical setup with flip mirrors. We believe that this flexibility will also be useful for the integration of pulse compression cavities into time-resolved microscopes²⁶. If the purpose of the cavity is to compress single-electron pulses and thus improve the time resolution of the experiment,⁶⁷ creating electrons from the tip of the emitter will be preferable due to the smaller source size. However, if the cavity is instead used to boost sensitivity by increasing the number of electrons per pulse without sacrificing time resolution, the number of electrons from the emitter may not be sufficiently high, and creating a large number of electrons from the extractor can be advantageous. Our characterization of space-charge limited electron pulses from the emitter and extractor offers a guide for choosing the best operating parameters for a given experiment.

References

- (1) Kwon, O.-H.; Barwick, B.; Park, H. S.; Baskin, J. S.; Zewail, A. H. Nanoscale Mechanical Drumming Visualized by 4D Electron Microscopy. *Nano Lett.* **2008**, *8* (11), 3557–3562.
- (2) Kwon, O.-H.; Zewail, A. H. 4D Electron Tomography. *Science* **2010**, *328* (5986), 1668–1673.
- (3) Baskin, J. S.; Park, H. S.; Zewail, A. H. Nanomusical Systems Visualized and Controlled in 4D Electron Microscopy. *Nano Lett.* **2011**, *11* (5), 2183–2191.
- (4) Lorenz, U. J.; Zewail, A. H. Biomechanics of DNA Structures Visualized by 4D Electron Microscopy. *Proc. Natl. Acad. Sci.* **2013**, *110* (8), 2822–2827.
- (5) McKenna, A. J.; Eliason, J. K.; Flannigan, D. J. Spatiotemporal Evolution of Coherent Elastic Strain Waves in a Single MoS₂ Flake. *Nano Lett.* **2017**, *17* (6), 3952–3958.
- (6) Lorenz, U. J.; Zewail, A. H. Observing Liquid Flow in Nanotubes by 4D Electron Microscopy. *Science* **2014**, *344* (6191), 1496–1500.
- (7) Kim, J. S.; LaGrange, T.; Reed, B. W.; Taheri, M. L.; Armstrong, M. R.; King, W. E.; Browning, N. D.; Campbell, G. H. Imaging of Transient Structures Using Nanosecond in Situ TEM. *Science* **2008**, *321* (5895), 1472–1475.
- (8) LaGrange, T.; Reed, B. W.; Santala, M. K.; McKeown, J. T.; Kulovits, A.; Wiezorek, J. M. K.; Nikolova, L.; Rosei, F.; Siwick, B. J.; Campbell, G. H. Approaches for Ultrafast Imaging of Transient Materials Processes in the Transmission Electron Microscope. *Micron* **2012**, *43* (11), 1108–1120.
- (9) Carbone, F.; Kwon, O.-H.; Zewail, A. H. Dynamics of Chemical Bonding Mapped by Energy-Resolved 4D Electron Microscopy. *Science* **2009**, *325* (5937), 181–184.

- (10) Park, S. T.; Flannigan, D. J.; Zewail, A. H. Irreversible Chemical Reactions Visualized in Space and Time with 4D Electron Microscopy. *J. Am. Chem. Soc.* **2011**, *133* (6), 1730–1733.
- (11) Sinha, S. K.; Khammari, A.; Picher, M.; Roulland, F.; Viart, N.; LaGrange, T.; Banhart, F. Nanosecond Electron Pulses in the Analytical Electron Microscopy of a Fast Irreversible Chemical Reaction. *Nat. Commun.* **2019**, *10* (1), 3648.
- (12) Park, H. S.; Baskin, J. S.; Zewail, A. H. 4D Lorentz Electron Microscopy Imaging: Magnetic Domain Wall Nucleation, Reversal, and Wave Velocity. *Nano Lett.* **2010**, *10* (9), 3796–3803.
- (13) Barwick, B.; Flannigan, D. J.; Zewail, A. H. Photon-Induced near-Field Electron Microscopy. *Nature* **2009**, *462* (7275), 902–906.
- (14) Priebe, K. E.; Rathje, C.; Yalunin, S. V.; Hohage, T.; Feist, A.; Schäfer, S.; Ropers, C. Attosecond Electron Pulse Trains and Quantum State Reconstruction in Ultrafast Transmission Electron Microscopy. *Nat. Photonics* **2017**, *11* (12), 793–797.
- (15) Morimoto, Y.; Baum, P. Diffraction and Microscopy with Attosecond Electron Pulse Trains. *Nat. Phys.* **2018**, *14* (3), 252–256.
- (16) Schönenberger, N.; Mittelbach, A.; Yousefi, P.; McNeur, J.; Niedermayer, U.; Hommelhoff, P. Generation and Characterization of Attosecond Microbunched Electron Pulse Trains via Dielectric Laser Acceleration. *Phys. Rev. Lett.* **2019**, *123* (26), 264803.
- (17) Zhang, L.; Hoogenboom, J. P.; Cook, B.; Kruit, P. Photoemission Sources and Beam Blankers for Ultrafast Electron Microscopy. *Struct. Dyn.* **2019**, *6* (5), 051501.
- (18) Lau, J. W.; Schliep, K. B.; Katz, M. B.; Gokhale, V. J.; Gorman, J. J.; Jing, C.; Liu, A.; Zhao, Y.; Montgomery, E.; Choe, H.; Rush, W.; Kanareykin, A.; Fu, X.; Zhu, Y. Laser-Free GHz Stroboscopic Transmission Electron Microscope: Components, System Integration, and

Practical Considerations for Pump–Probe Measurements. *Rev. Sci. Instrum.* **2020**, *91* (2), 021301.

(19) Verhoeven, W.; van Rens, J. F. M.; Kieft, E. R.; Mutsaers, P. H. A.; Luiten, O. J. High Quality Ultrafast Transmission Electron Microscopy Using Resonant Microwave Cavities. *Ultramicroscopy* **2018**, *188*, 85–89.

(20) Weppelman, I. G. C.; Moerland, R. J.; Zhang, L.; Kieft, E.; Kruit, P.; Hoogenboom, J. P. Pulse Length, Energy Spread, and Temporal Evolution of Electron Pulses Generated with an Ultrafast Beam Blanker. *Struct. Dyn.* **2019**, *6* (2), 024102.

(21) Niermann, T.; Lehmann, M.; Wagner, T. Gated Interference for Time-Resolved Electron Holography. *Ultramicroscopy* **2017**, *182*, 54–61.

(22) Das, P.; Blazit, J. D.; Tencé, M.; Zagonel, L. F.; Auad, Y.; Lee, Y. H.; Ling, X. Y.; Losquin, A.; Colliex, C.; Stéphan, O.; García de Abajo, F. J.; Kociak, M. Stimulated Electron Energy Loss and Gain in an Electron Microscope without a Pulsed Electron Gun. *Ultramicroscopy* **2019**, *203*, 44–51.

(23) Gao, M.; Jean-Ruel, H.; Cooney, R. R.; Stampe, J.; de Jong, M.; Harb, M.; Sciaini, G.; Moriena, G.; Dwayne Miller, R. J. Full Characterization of RF Compressed Femtosecond Electron Pulses Using Ponderomotive Scattering. *Opt. Express* **2012**, *20* (11), 12048.

(24) Gao, M.; Lu, C.; Jean-Ruel, H.; Liu, L. C.; Marx, A.; Onda, K.; Koshihara, S.; Nakano, Y.; Shao, X.; Hiramatsu, T.; Saito, G.; Yamochi, H.; Cooney, R. R.; Moriena, G.; Sciaini, G.; Miller, R. J. D. Mapping Molecular Motions Leading to Charge Delocalization with Ultrabright Electrons. *Nature* **2013**, *496* (7445), 343–346.

(25) Miller, R. J. D. Femtosecond Crystallography with Ultrabright Electrons and X-Rays: Capturing Chemistry in Action. *Science* **2014**, *343* (6175), 1108–1116.

(26) Sannomiya, T.; Arai, Y.; Nagayama, K.; Nagatani, Y. Transmission Electron Microscope Using a Linear Accelerator. *Phys. Rev. Lett.* **2019**, *123* (15), 150801.

- (27) Ehberger, D.; Mohler, K. J.; Vasileiadis, T.; Ernstorfer, R.; Waldecker, L.; Baum, P. Terahertz Compression of Electron Pulses at a Planar Mirror Membrane. *Phys. Rev. Appl.* **2019**, *11* (2), 024034.
- (28) Yang, J.; Yoshida, Y. Relativistic Ultrafast Electron Microscopy: Single-Shot Diffraction Imaging with Femtosecond Electron Pulses. *Adv. Condens. Matter Phys.* **2019**, *2019*, 1–6.
- (29) Li, R. K.; Musumeci, P. Single-Shot MeV Transmission Electron Microscopy with Picosecond Temporal Resolution. *Phys. Rev. Appl.* **2014**, *2* (2), 024003.
- (30) LaGrange, T.; Campbell, G. H.; Reed, B. W.; Taheri, M.; Pesavento, J. B.; Kim, J. S.; Browning, N. D. Nanosecond Time-Resolved Investigations Using the in Situ of Dynamic Transmission Electron Microscope (DTEM). *Ultramicroscopy* **2008**, *108* (11), 1441–1449.
- (31) Picher, M.; Bücke, K.; LaGrange, T.; Banhart, F. Imaging and Electron Energy-Loss Spectroscopy Using Single Nanosecond Electron Pulses. *Ultramicroscopy* **2018**, *188*, 41–47.
- (32) Piazza, L.; Masiel, D. J.; LaGrange, T.; Reed, B. W.; Barwick, B.; Carbone, F. Design and Implementation of a Fs-Resolved Transmission Electron Microscope Based on Thermionic Gun Technology. *Chem. Phys.* **2013**, *423*, 79–84.
- (33) Lee, Y. M.; Kim, Y. J.; Kim, Y.-J.; Kwon, O.-H. Ultrafast Electron Microscopy Integrated with a Direct Electron Detection Camera. *Struct. Dyn.* **2017**, *4* (4), 044023.
- (34) Ji, S.; Piazza, L.; Cao, G.; Park, S. T.; Reed, B. W.; Masiel, D. J.; Weissenrieder, J. Influence of Cathode Geometry on Electron Dynamics in an Ultrafast Electron Microscope. *Struct. Dyn.* **2017**, *4* (5), 054303.
- (35) Zandi O.; Sykes, A. E.; Cornelius, R. D.; Alcorn, F. M.; Zerbe, B.; Duxbury, P. M.; Reed, B. W.; van der Veen, R. M. Transient Lensing from a Photoemitted Electron Gas Imaged by Ultrafast Electron Microscopy. *Nat. Commun.* **2020**, *11*, 3001.

- (36) Houdellier, F.; Caruso, G. M.; Weber, S.; Kociak, M.; Arbouet, A. Development of a High Brightness Ultrafast Transmission Electron Microscope Based on a Laser-Driven Cold Field Emission Source. *Ultramicroscopy* **2018**, *186*, 128–138.
- (37) Feist, A.; Bach, N.; Rubiano da Silva, N.; Danz, T.; Möller, M.; Priebe, K. E.; Domröse, T.; Gatzmann, J. G.; Rost, S.; Schauss, J.; Strauch, S.; Bormann, R.; Sivilis, M.; Schäfer, S.; Ropers, C. Ultrafast Transmission Electron Microscopy Using a Laser-Driven Field Emitter: Femtosecond Resolution with a High Coherence Electron Beam. *Ultramicroscopy* **2017**, *176*, 63–73.
- (38) Zhu, C.; Zheng, D.; Wang, H.; Zhang, M.; Li, Z.; Sun, S.; Xu, P.; Tian, H.; Li, Z.; Yang, H.; Li, J. Development of Analytical Ultrafast Transmission Electron Microscopy Based on Laser-Driven Schottky Field Emission. *Ultramicroscopy* **2020**, *209*, 112887.
- (39) Swanson, L.; Schwind, G. Review of ZrO/W Schottky Cathode. In *Handbook of Charged Particle Optics*; 2008; pp 1–28.
- (40) Swanson, L. W.; Schwind, G. A. Chapter 2 A Review of the Cold-Field Electron Cathode. *Adv. Imaging Electron Phys.* **2009**, *159*, 63–100.
- (41) M.S. Bronsgeest. *Physics of Schottky Electron Sources: Theory and Optimum Operation*; Jenny Stanford Publishing, 2014.
- (42) Otten, M. T.; Coene, W. M. J. High-Resolution Imaging on a Field Emission TEM. *Ultramicroscopy* **1993**, *48* (1–2), 77–91.
- (43) Lichte, H.; Lehmann, M. Electron Holography - Basics and Applications. *Rep. Prog. Phys.* **2008**, *71* (1).
- (44) Niermann, T.; Lehmann, M.; Wagner, T. Gated Interference for Time-Resolved Electron Holography. *Ultramicroscopy* **2017**, *182*, 54–61.

- (45) Houdellier, F.; Caruso, G. M.; Weber, S.; Hýtch, M. J.; Gatel, C.; Arbouet, A. Optimization of Off-Axis Electron Holography Performed with Femtosecond Electron Pulses. *Ultramicroscopy* **2019**, *202*, 26–32.
- (46) Tiemeijer, P. C.; Bischoff, M.; Freitag, B.; Kisielowski, C. Using a Monochromator to Improve the Resolution in TEM to below 0.5Å. Part I: Creating Highly Coherent Monochromated Illumination. *Ultramicroscopy* **2012**, *114*, 72–81.
- (47) Mo, M. Z.; Chen, Z.; Li, R. K.; Dunning, M.; Witte, B. B. L.; Baldwin, J. K.; Fletcher, L. B.; Kim, J. B.; Ng, A.; Redmer, R.; Reid, A. H.; Shekhar, P.; Shen, X. Z.; Shen, M.; Sokolowski-Tinten, K.; Tsui, Y. Y.; Wang, Y. Q.; Zheng, Q.; Wang, X. J.; Glenzer, S. H. Heterogeneous to Homogeneous Melting Transition Visualized with Ultrafast Electron Diffraction. *Science* **2018**, *360* (6396), 1451–1455.
- (48) Voss, J. M.; Olshin, P. K.; Charbonnier, R.; Drabbels, M.; Lorenz, U. J. In Situ Observation of Coulomb Fission of Individual Plasmonic Nanoparticles. *ACS Nano* **2019**, *13* (11), 12445–12451.
- (49) Olshin, P. K.; Voss, J. M.; Drabbels, M.; Lorenz, U. J. Real-Time Observation of Jumping and Spinning Nanodroplets. *Struct. Dyn.* **2020**, *7* (1), 011101.
- (50) Bongiovanni, G.; Olshin, P. K.; Drabbels, M.; Lorenz, U. J. Intense Microsecond Electron Pulses from a Schottky Emitter. *Appl. Phys. Lett.* **2020**, *116* (23), 234103.
- (51) Baum, P.; Zewail, A. H. Breaking Resolution Limits in Ultrafast Electron Diffraction and Microscopy. *Proc. Natl. Acad. Sci.* **2006**, *103* (44), 16105–16110.
- (52) Maldonado, J. R.; Liu, Z.; Dowell, D. H.; Kirby, R. E.; Sun, Y.; Pianetta, P.; Pease, F. Robust CsBr / Cu Photocathodes for the Linac Coherent Light Source. *Phys. Rev. Spec. Top. - Accel. Beams* **2008**, *11* (6), 060702.

- (53) Qian, H. J.; Li, C.; Du, Y. C.; Yan, L. X.; Hua, J. F.; Huang, W. H.; Tang, C. X. Experimental Investigation of Thermal Emittance Components of Copper Photocathode. *Phys. Rev. Spec. Top. - Accel. Beams* **2012**, *15* (4), 040102.
- (54) Surplice, N. A.; D'Arcy, R. J. Reduction in the Work Function of Stainless Steel by Electric Fields. *J. Phys. F Met. Phys.* **1972**, *2* (1), L8–L10.
- (55) Nishiyama, H.; Ohshima, T.; Shinada, H. Tungsten Schottky Emitters with Reservoirs of Metal Oxide or Nitride. *Appl. Surf. Sci.* **1999**, *146* (1–4), 382–386.
- (56) Brongseest, M. S. Physics of Schottky Electron Sources, Technical University of Delft, 2009.
- (57) Plemmons, D. A.; Flannigan, D. J. Ultrafast Electron Microscopy: Instrument Response from the Single-Electron to High Bunch-Charge Regimes. *Chem. Phys. Lett.* **2017**, *683*, 186–192.
- (58) Manz, S.; Casandruc, A.; Zhang, D.; Zhong, Y.; Loch, R. A.; Marx, A.; Hasegawa, T.; Liu, L. C.; Bayesteh, S.; Delsim-Hashemi, H.; Hoffmann, M.; Felber, M.; Hachmann, M.; Mayet, F.; Hirscht, J.; Keskin, S.; Hada, M.; Epp, S. W.; Flöttmann, K.; Miller, R. J. D. Mapping Atomic Motions with Ultrabright Electrons: Towards Fundamental Limits in Space-Time Resolution. *Faraday Discuss.* **2015**, *177*, 467–491.
- (59) Park, S. T.; Lin, M.; Zewail, A. H. Photon-Induced near-Field Electron Microscopy (PINEM): Theoretical and Experimental. *New J. Phys.* **2010**, *12* (12), 123028.
- (60) Kuwahara, M.; Nambo, Y.; Aoki, K.; Sameshima, K.; Jin, X.; Ujihara, T.; Asano, H.; Saitoh, K.; Takeda, Y.; Tanaka, N. The Boersch Effect in a Picosecond Pulsed Electron Beam Emitted from a Semiconductor Photocathode. *Appl. Phys. Lett.* **2016**, *109* (1), 013108.
- (61) Koyama, R. Y.; Spicer, W. E. Photoemission Studies of Indium. *Phys. Rev. B* **1971**, *4* (12), 4318–4329.

- (62) Rangarajan, L.; Bhide, G. 15. Photoemission Energy Distribution Studies of Gold Thin Films under Uv Excitation by a Photoelectron Spectroscopic Method. *Vacuum* **1980**, *30* (11–12), 515–522.
- (63) Filippetto, D.; Musumeci, P.; Zolotarev, M.; Stupakov, G. Maximum Current Density and Beam Brightness Achievable by Laser-Driven Electron Sources. *Phys. Rev. Spec. Top. - Accel. Beams* **2014**, *17* (2), 024201.
- (64) Bach, N.; Domröse, T.; Feist, A.; Rittmann, T.; Strauch, S.; Ropers, C.; Schäfer, S. Coulomb Interactions in High-Coherence Femtosecond Electron Pulses from Tip Emitters. *Struct. Dyn.* **2019**, *6* (1), 014301.
- (65) van Veen, A. H. V.; Hagen, C. W.; Barth, J. E.; Kruit, P. Reduced Brightness of the ZrO/W Schottky Electron Emitter. *J. Vac. Sci. Technol. B Microelectron. Nanometer Struct. Process. Meas. Phenom.* **2001**, *19* (6), 2038–2044.
- (66) Cook, B.; Verduin, T.; Hagen, C. W.; Kruit, P. Brightness Limitations of Cold Field Emitters Caused by Coulomb Interactions. *J. Vac. Sci. Technol. B* **2010**, *28* (6), C6c74-C6c79.
- (67) Gliserin, A.; Walbran, M.; Krausz, F.; Baum, P. Sub-Phonon-Period Compression of Electron Pulses for Atomic Diffraction. *Nat. Commun.* **2015**, *6* (1), 8723.

Chapter 3

In situ Observation of Coulomb Fission of Individual Plasmonic Nanoparticles

Introduction[†]

Gold nanoparticles have found a plethora of applications in a wide range of fields, including biomedical imaging,¹ sensing,^{2,3} cancer therapy,^{4,5} gene regulation,⁶ catalysis,⁷ and optical devices.^{8,9} The strong plasmonic absorptions of gold nanoparticles provide a convenient means to reshape them through pulsed laser irradiation^{10,11} and thus tune their properties.^{12–14} This has given rise to an entire field of research that investigates and exploits a range of mechanisms for laser particle reshaping.^{10,11} At low laser fluence, shape transformations are induced through partial or complete melting and subsequent resolidification of the nanoparticles.^{15,16} For example, this approach has recently been applied to reshape gold nanorods and improve their monodispersity, thus yielding exceptionally narrow surface plasmon resonances.¹⁴ If higher fluences are employed to heat the particles beyond their boiling point, size reduction occurs through surface evaporation.^{17,18} Fragmentation can be achieved through an entirely different set of mechanisms when intense ultrafast laser pulses are used to ionize the nanoparticles. On ultrafast timescales, excited electrons do not have sufficient time to equilibrate with the lattice, which requires about 3 ps (Ref. 19), and the particles are ionized through multiphoton and thermionic emission.^{20–23} After the laser pulse, the hot electrons equilibrate with the lattice through electron-phonon coupling, which can cause the particle to melt. If the Coulomb repulsion in the resulting charged droplet surpasses its surface tension,

[†] Reproduced with permission from Voss J.M., Olshin P.K., Charbonnier R., Drabbels M., Lorenz U. J., *ACS Nano* 13, 11, 12445-12451 (2019). Copyright 2019 American Chemical Society.

Authors Contributions: V.J.M. and P.K.O. performed the experiments and analyzed the data; C.R. analyzed the data; M.D. and U.J.L. supervised the project; U.J.L. wrote the manuscript with the contribution from all authors.

i.e. if the Rayleigh stability limit is exceeded,²⁴ Coulomb fission occurs through the emission of highly charged progeny droplets.^{25–27} At even higher levels of ionization, Coulomb explosion of the droplet^{28,29} or of the solid particle³⁰ may be induced, which involves the ejection of a large number of charged fragments.

Elucidation of the mechanisms of complex shape transformations that occur during pulsed laser irradiation is frequently a challenge. *Ex situ* analysis of nanoparticle products usually only provides indirect information about the morphological changes that take place during laser irradiation. While time-resolved spectroscopy²⁸ and X-ray diffraction³⁰ can probe the particle evolution on short timescales, they frequently yield only indirect morphological information and thus do not easily permit the elucidation of intricate, multistep processes. In the absence of *in situ* observations on the single-particle level, a robust understanding of different reshaping mechanisms has thus remained elusive, hampering their application in a deterministic fashion. Questions of an even more fundamental nature remain, for example, regarding the mechanism of Coulomb fission, which for the smallest droplets has been predicted to occur through ion emission rather than ejection of progeny droplets.^{31,32}

Here, we present an *in situ* electron microscopy study of Coulomb fission of plasmonic nanoparticles. We observe that under intense femtosecond laser irradiation, gold nanoparticles encapsulated in a silica shell fission through emission of small progeny droplets comprised of about 10-500 atoms. Interestingly, the ejection of these progeny droplets preferentially occurs along the direction of the laser polarization. We find that the droplets emitted from successive fission events accumulate within the silica shell and coalesce into a second core, so that a dual-core particle is formed. Not only do our observations provide insights into the mechanism of Coulomb fission of plasmonic nanoparticles, but they also suggest a straightforward laser-based approach for creating surfaces decorated with aligned dual-gold-core silica shell nanoparticles.

Results and Discussion

The experiments reported here were performed with a modified JEOL 2200FS transmission electron microscope, operating at an accelerating voltage of 160 kV. Silica-coated gold nanoparticles with a 20 ± 3 nm diameter core and a 20 ± 5 nm thick shell (suspended in ethanol, available from NanoComposix) were deposited onto an electron microscopy specimen grid (multilayer graphene on 2000 mesh copper) and were irradiated *in-situ* either with femtosecond (515 nm, 240 fs, 20 kHz) or nanosecond laser pulses (532 nm, 1 ns, 20 kHz). This is achieved with the help of an aluminum mirror that is mounted above the upper pole piece of the objective lens and that reflects the laser beams onto the sample such that they propagate almost collinearly with the electron beam. The excitation wavelengths are close to the predicted absorption maximum at 533 nm of the nanoparticles.³³ In order to obtain the laser fluence, the laser spot size was determined *in-situ* with the knife edge method.

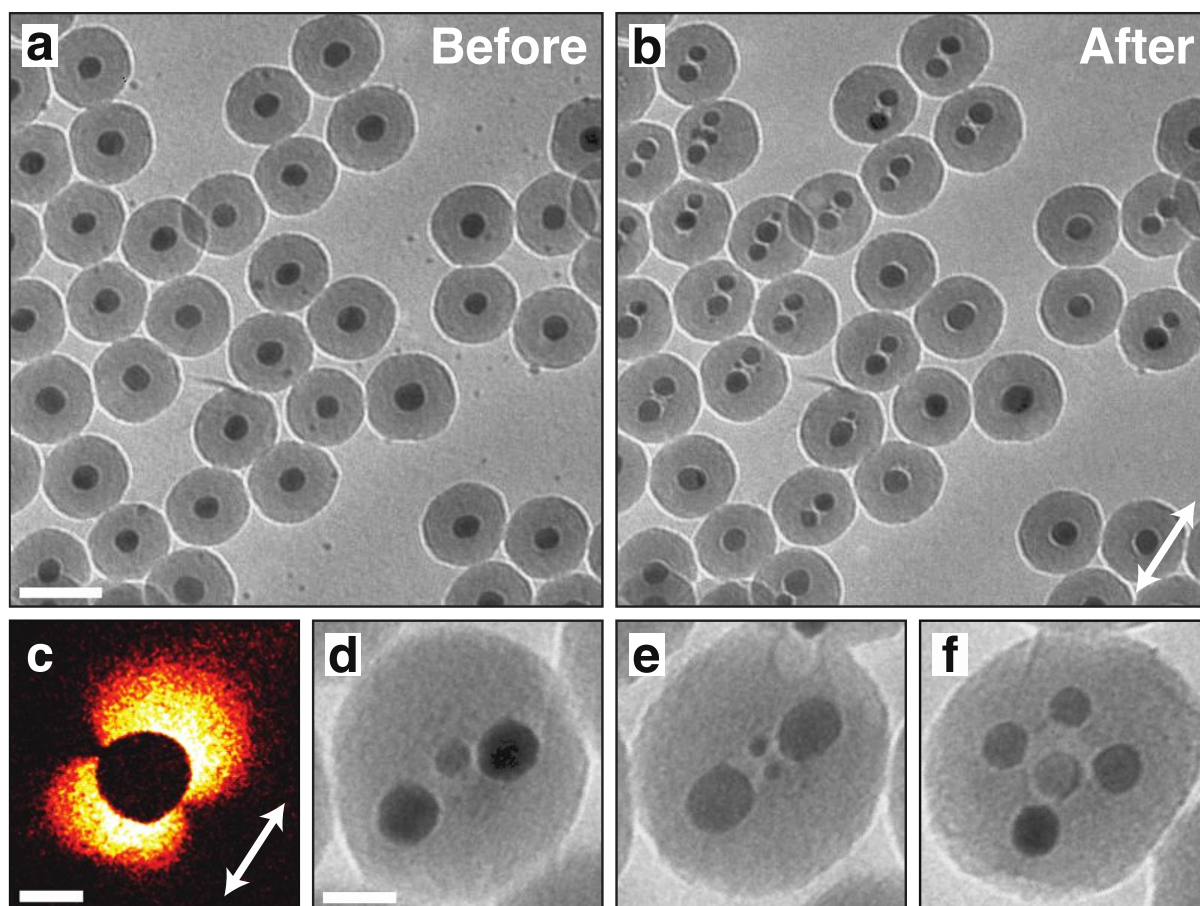


Figure 3-1. Formation of aligned dual-gold-core silica shell nanoparticles under femtosecond laser irradiation. (a,b) Micrographs (0.1 second exposure time) of core-shell particles before and after femtosecond laser irradiation (22 mJ/cm^2 , 10^6 pulses). The polarization is indicated with a double-headed arrow. Scale bar, 50 nm. (c) *In-situ* determination of the laser polarization (double-headed arrow) with photon-induced near-field electron microscopy. An energy gain-filtered image (180 seconds exposure time) of a gold nanoparticle shows the dipolar near-fields during laser excitation. This experiment maps out a particular Fourier component of the z-component of the electric field, as encoded by the color scale. Scale bar, 100 nm. (d-f) At higher fluence (43 mJ/cm^2), the gold cores split into multiple particles (images were averaged from five micrographs recorded with the exposure time of 0.1 second). Scale bar, 15 nm. The double-headed arrow denotes the laser polarization.

Figure 3-1(a) shows a micrograph of a typical sample. After irradiation with 10^6 femtosecond laser pulses [Fig. 3-1(b)], many of the cores have fragmented into two equally-sized gold particles that appear to be connected by a void in the silica shell. The newly formed dual-cores are roughly aligned along the polarization direction of the laser (as indicated by the double-headed arrow). Here, we determine the laser polarization direction *in situ* by illuminating a gold nanoparticle with an ultrafast optical pulse and imaging the scattered near-fields with photon-induced near-field electron microscopy³⁴ [Fig. 3-1(c)]. Briefly, the ultrafast laser pulse striking the gold particle is spatially and temporally overlapped with an ultrafast electron pulse. Under such conditions, electrons that interact with the near-fields of the particle gain or lose energy in multiples of the photon energy. The energy-filtered micrograph of Fig. 3-1(c), which is formed only with electrons that have gained energy, therefore maps the dipolar near-fields of the particle and allows us to accurately determine the laser polarization direction.³⁵ We find that femtosecond laser irradiation of the gold-core silica shell particles predominantly leads to the formation of two equally-sized gold cores. However, approximately 2% of particles feature three, four, or even five cores of different sizes arranged in varying configurations [Fig. 3-1(d-f)].

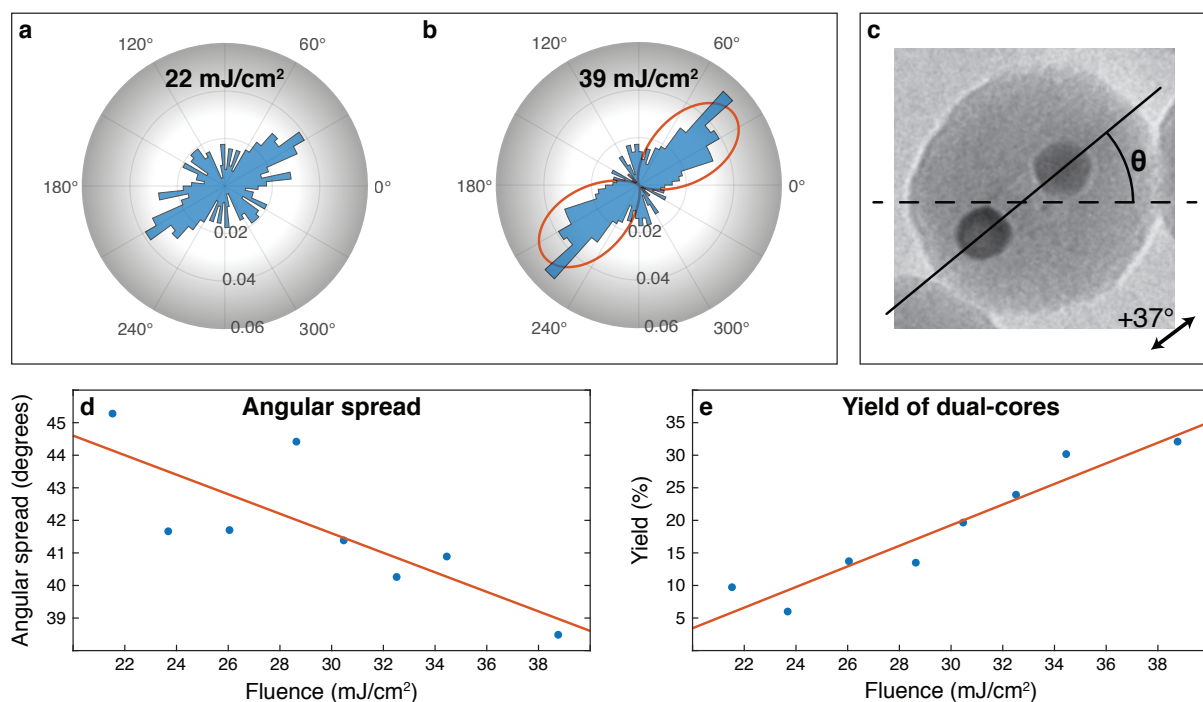


Figure 3-2. Angular distribution and yield of the dual-cores as a function of laser fluence. (a,b) Angular distributions for two different laser fluences ($6 \cdot 10^6$ pulses). The red line in (b) represents an estimate of the relative photoemission current from the core. (c) Angles θ are measured as illustrated. The laser polarization is indicated with a double-headed arrow. (d) Angular spread (as measured by the standard deviation) as a function of laser fluence and linear fit (solid line). (e) Yield of dual-core particles as a function of laser fluence and linear fit (solid line).

We quantify the degree of alignment of the dual-core particles as well as their yield as a function of laser fluence. For core-shell nanoparticles that were irradiated with $6 \cdot 10^6$ ultrafast laser pulses, we obtain a fairly broad angular distribution at a fluence of 22 mJ/cm² [Fig. 3-2(a)]. At almost twice the fluence [39 mJ/cm², Fig. 3-2(b)], the distribution markedly narrows and peaks around 37°, the angle of the laser polarization. Here, the angles θ of the dual-cores are determined with respect to the horizontal, as shown in Fig. 3-2(c). We find that

with increasing fluence, the angular spread of the dual-cores (as measured by the standard deviation of the angle θ) decreases [Fig. 3-2(d)]. At the same time, the yield of the dual-cores increases with laser fluence, reaching about 30% at the highest fluence employed here [Fig. 3-2(e)]. The lines in Fig. 3-2(d) and 3-2(e) represent linear fits of the data that serve to guide the eye.

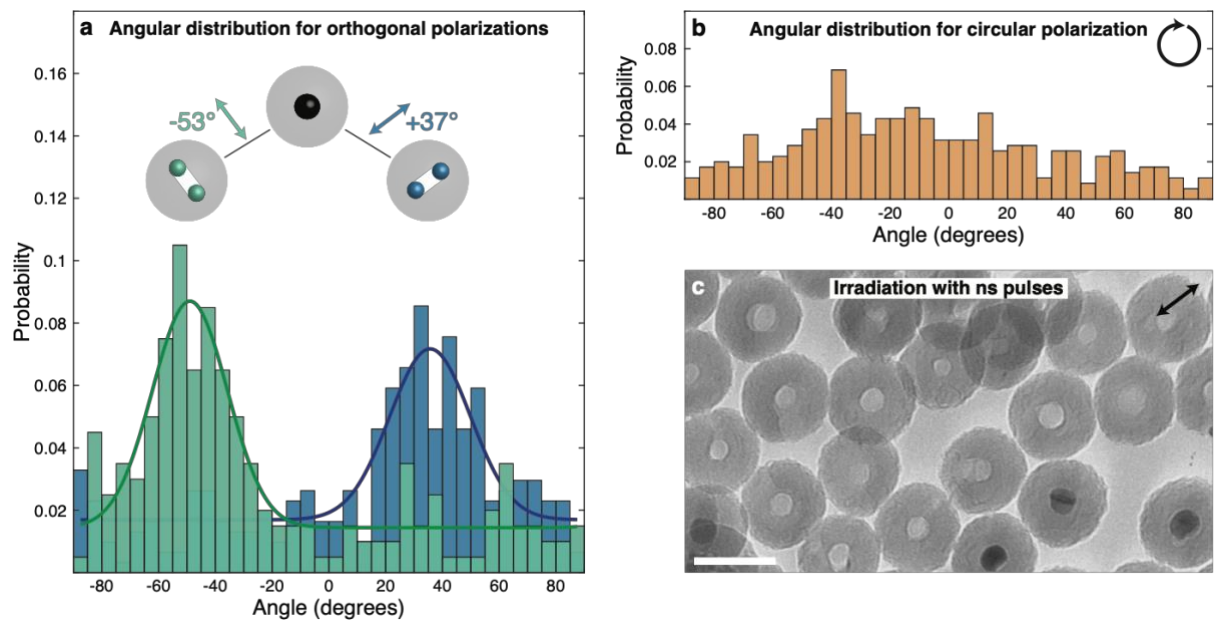


Figure 3-3. Effects of laser polarization and pulse duration on the formation of dual-cores. (a) Angular distributions for orthogonal laser polarizations (-53° and $+37^\circ$, indicated with double-headed arrows; $6 \cdot 10^6$ femtosecond pulses; 30 mJ/cm^2). The distributions peak at -49° and $+36^\circ$, as determined from Gaussian fits with constant offsets. (b) Angular distributions after illumination with circular polarization ($6 \cdot 10^6$ femtosecond pulses, 30 mJ/cm^2). (c) After nanosecond laser irradiation ($6 \cdot 10^6$ pulses, 1 ns, 41 mJ/cm^2) the gold cores have evaporated. The polarization is indicated with a double-headed arrow. Scale bar, 50 nm.

Figure 3-3(a) reveals that it is the linear polarization of the ultrafast laser pulses that determines the alignment of the dual-cores. When we use a half-wave plate in the laser beam path to rotate the polarization by 90° , the angular distribution of the dual-cores (irradiated with $6 \cdot 10^6$ pulses at 30 mJ/cm^2) shifts by the same angle within experimental accuracy [Fig. 3-3(a), green and blue histograms, the lines indicate Gaussian fits with a constant offset]. In contrast, irradiation of the core-shell particles with circularly polarized light under otherwise identical conditions produces a broad angular distribution [orange histogram in Fig. 3-3(b)]. Furthermore, we find that the pulse duration plays a crucial role in the formation of the dual-core particles. Whereas both femtosecond and picosecond pulses ($\lesssim 3 \text{ ps}$, obtained by stretching the output of the femtosecond laser) can be employed to form the dual-core particles, nanosecond pulses of similar fluence leave the gold cores largely unchanged. When we increase the fluence of the nanosecond pulses further, the gold cores simply evaporate as evidenced by the micrograph in Fig. 3-3(c) ($6 \cdot 10^6$ pulses, 41 mJ/cm^2). In some instances, narrow channels in the silica shell can be observed that appear to be created as a result of the evaporation process. Evidently, ultrafast pulses are necessary to form the dual-core particles, which strongly suggests that ionization of the core plays a central role in the fragmentation mechanism. Ionization can only be achieved with ultrafast pulses and indeed has been observed in previous studies for similar laser pulse parameters.^{20–23,29} As discussed above, on ultrafast timescales, the electrons do not have sufficient time to equilibrate with the lattice, so that multiphoton emission can be induced. In contrast, nanosecond laser pulses will simply heat the gold cores to high temperatures without causing significant ionization.^{10,29}

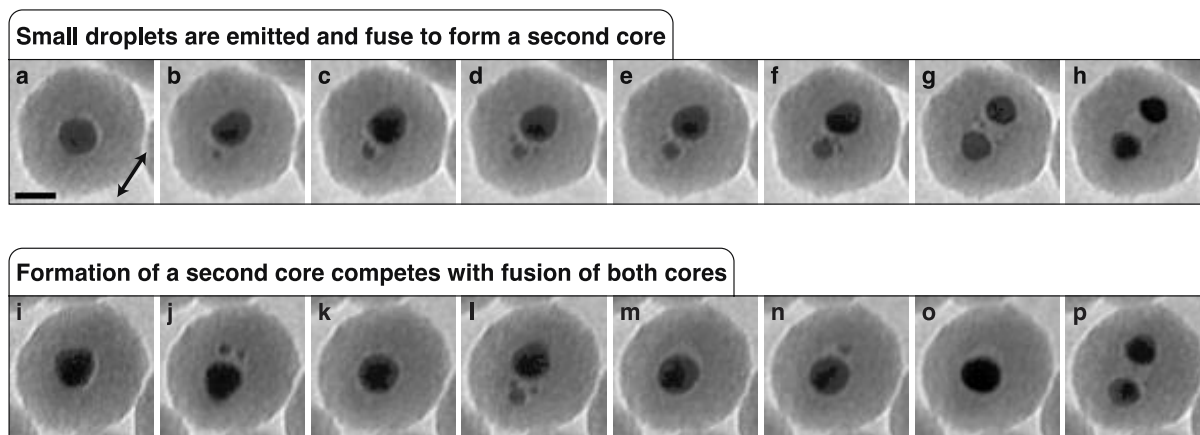


Figure 3-4. *In situ* observation of the formation of aligned dual-core particles. (a-h) Under femtosecond laser irradiation, the gold core ejects small droplets, which accumulate and fuse into a second core of equal size. (i-p) A core-shell particle undergoes repeated cycles in which a second core is formed and subsequently fuses again with the first. The laser polarization is indicated with a double-headed arrow in (a). Scale bar, 20 nm.

In order to unravel the formation mechanism of the dual-cores, we carry out *in-situ* observations of individual particles under laser irradiation. Typical sequences of events are shown in Fig. 3-4. The images were extracted from a movie recorded with the frame intervals of 1 second. They reveal that the mechanism involves the stepwise ejection of small gold fragments from the core. When the nanoparticle displayed in Fig. 3-4(a) is irradiated with femtosecond pulses (16 mJ/cm^2), its gold core ejects a small particle of about 2 nm diameter [Fig. 3-4(b)] along the direction of the laser polarization [double-headed arrow in (a)]. Subsequently, further particles of 1-2 nm diameter (about 30-200 atoms) are emitted [Fig. 3-4(c,d)], which can then be seen to coalesce into a single mass [Fig. 3-4(e)]. This secondary gold core continues to grow by absorbing further particles [Fig. 3-4(f)] until both cores eventually reach a similar size [Fig. 3-4(g,h)]. We also observe that the shapes of the cores fluctuate under laser irradiation. This suggests that the cores melt after every laser pulse

and then resolidify in varying configurations. Indeed, we estimate that after the laser pulse, the temperature of the cores initially exceeds the melting point of gold by hundreds of Kelvin, so that melting can be expected to occur rapidly, within tens of picoseconds.³⁶ We also frequently observe that the formation of a second gold core competes with the fusion of both cores, as illustrated by the sequence of micrographs in Fig. 3-4(i-p). The core of the nanoparticle in Fig. 3-4(i) initially emits two small fragments [Fig. 3-4(j)]. However, these particles are then reabsorbed by the core [Fig. 3-4(k)]. This process then repeats two more times [Fig. 3-4(l-o)], until two well-separated cores of similar diameter are finally formed [Fig. 3-4(p)].

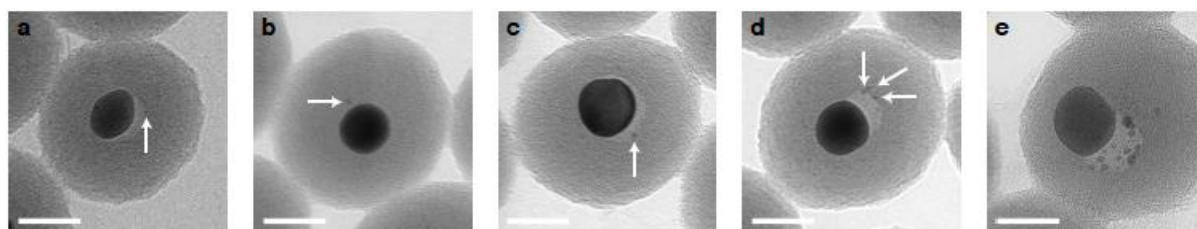


Figure 3-5. High magnification micrographs of progeny particles. Gold-core silica shell nanoparticles were irradiated with femtosecond pulses (20 mJ/cm^2 , 20 kHz) until a small number of progeny droplets were emitted. Subsequently, the particles were imaged without laser irradiation. The diameters of the emitted particles in (a-c) are 0.7 nm , 1.4 nm , 1.5 nm , respectively. In (d) the diameters of the particles are between $1.6\text{-}1.8 \text{ nm}$. The larger particles observed in (e) are likely the result of progeny droplets which have coalesced into larger particles. The micrographs were recorded with the acquisition time of 1 second . Scale bars, 20 nm .

In order to better characterize the emitted fragments, we stop the laser irradiation once a gold core has ejected just a small number of fragments, and image them at high magnification (Fig. 3-5). We find that their diameters range from 0.7 to 2.5 nm (about 10 to 500 atoms). These

fragments have likely been created in a single emission event, since particle ejection occurs with a considerable angular spread. As further fragments are emitted from the core, some of them will coalesce with other particles already implanted in the silica shell. We note that we cannot exclude that even smaller fragments or individual atoms are also emitted from the core, since they may not offer sufficient contrast against the background of the thick silica shell.

The ejection of individual, small particles from the core strongly suggests that we are observing Coulomb fission of the ionized, liquid gold core. This interpretation is consistent with the fact that the process appears to be driven by the ionization of the cores, as discussed above, and that the cores melt under our experimental conditions. We note that our observations are in contrast to the mechanism previously proposed for the fragmentation of gold nanoparticles suspended in water that were irradiated with femtosecond pulses.^{28,29} Based on transient absorption spectroscopy and *ex-situ* product analysis, it was concluded that the nanoparticles undergo Coulomb explosion, shattering into a large number of fragments after a single laser pulse. Clearly, this mechanism does not operate under our experimental conditions.

The micrographs in Fig. 3-4 suggest that the laser polarization determines the direction in which progeny droplets are ejected, thus controlling the alignment of the resulting dual-cores. This may appear counterintuitive, since Coulomb fission can only occur once the core has melted, which requires tens of picoseconds.³⁶ Furthermore, the process of Coulomb fission itself can be estimated to require another 100 ps[‡] for a liquid gold droplet of 20 nm diameter

[‡] The timescale for Coulomb fission of the highly ionized liquid gold cores was estimated from the scaling behavior derived from numerical simulations.²⁶ The fission timescale, $t_{fission}$, is therefore given by

$$t_{fission} = \left(\frac{r^3 \rho}{\sigma} \right)^{\frac{1}{2}}$$

where r , ρ , and σ are the radius, density, and surface tension of the liquid gold core, respectively. Using $1.93 \cdot 10^4$ kg/m³ and 1.15 J/m² for the density and surface tension,⁴⁶ respectively, a molten gold core of 20 nm diameter is expected to undergo fission on a timescale of 100 ps.

that is charged to the Rayleigh limit. At this point, however, the molten gold particle should have lost any memory of the polarization of the laser pulse.

In order to resolve this apparent contradiction, it is important to realize that under our experimental conditions, the photoemission of electrons from the core is highly directional and predominantly occurs along the laser polarization direction. At incident peak fields of 10^8 - 10^9 V/m, such as those in our experiments, the ionization process is dominated by multiphoton emission.²⁰⁻²² The local emission current from the particle is therefore roughly proportional to the $2n$ th power of the electric field at the particle surface, where n is the number of photons required to overcome the work function of the metal.³⁷ Here, about two photons (2.4 eV) are necessary to overcome the work function of gold (5.1 eV). Since the field at the particle surface resembles that of an electric dipole, the photoemission current should therefore follow a $\cos^4(\theta)$ dependence, as shown by the red line in Fig. 3-2(b). In other words, near-field enhancement leads to a preferential emission of electrons along the laser polarization direction, as has been observed for multiphoton emission from a range of different nanoparticles.²⁰⁻²² Electrons injected into silicon dioxide thin films are known to populate trap states with lifetimes of seconds,^{38,39} far exceeding the timescale of Coulomb fission. The directional emission of electrons should therefore create an anisotropic charge distribution in the silica shell that persists long enough to steer the emission of progeny droplets, thus resulting in the alignment of the dual-cores. We note that a related mechanism has been proposed to induce the elongation of silver nanoparticles in bulk glass under irradiation with femtosecond pulses.^{40,41}

While many of the dual-core particles are aligned according to the laser polarization, a significant fraction is randomly oriented, as evidenced by the angular distributions in Fig. 3-3(a). Occasionally, the emission of the first progeny droplet occurs in a random direction, which appears to determine the final alignment of the dual-cores. We speculate that in these instances, inhomogeneities in the silica matrix surrounding the gold core steer the

emission of the first progeny droplet into a direction different from that of the laser polarization. This creates a void in the silica shell, which then drives the emission of subsequent progeny droplets in the same direction. Ultimately, a channel linking both cores is formed in the silica shell.

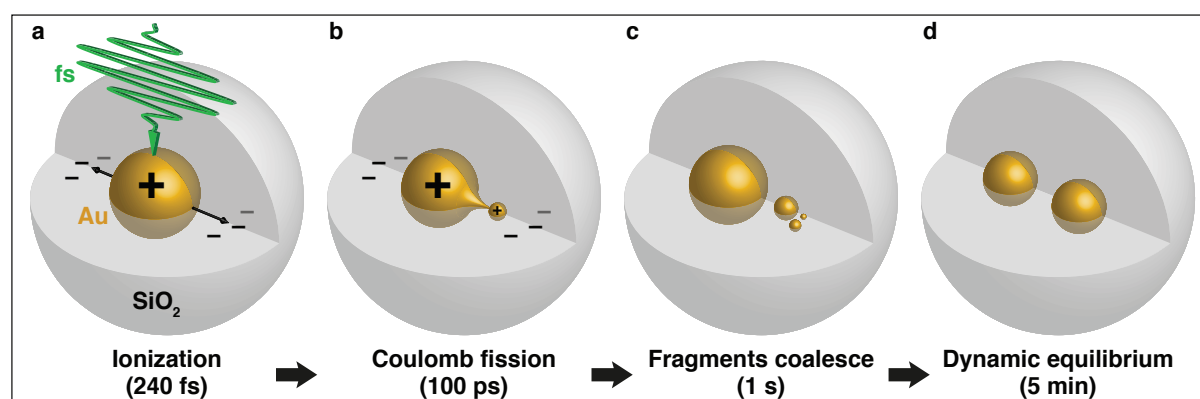


Figure 3-6. The formation mechanism of dual-core particles. (a) The femtosecond laser pulse ionizes the gold core. Electrons are preferentially ejected along the polarization direction. (b) The ionized gold core melts and undergoes Coulomb fission through emission of a highly charged progeny droplet. (c) Several progeny droplets accumulate and fuse into a second core. (d) A dynamic equilibrium is reached between both cores as they continue to fission.

Figure 3-6 summarizes the multistep formation mechanism of the dual-core particles. An ultrafast laser pulse (240 fs) ionizes the gold core, with photoemission of electrons occurring predominantly along the polarization direction of the laser, so that an anisotropic distribution of negative charge is created in the silica shell [Fig. 3-6(a)]. In a second step, the gold core melts and the ionized droplet undergoes Coulomb fission on a timescale of 100 ps [Fig. 3-6(b)]. The highly charged progeny droplets are preferentially ejected towards the areas of concentrated negative charge in the silica shell and coalesce into a second core [Fig. 3-6(c)], a

process that occurs in a matter of seconds. Lastly, the second core continues to grow through repeated absorption of progeny droplets, until both cores reach equal size [Fig. 3-6(d)]. This process is complete after several minutes. We note that once the second core has formed, it can also be observed to undergo Coulomb fission. Progeny droplets are then continuously ejected from either core and absorbed by the other, a process during which the void in the silica shell connecting both cores becomes more pronounced. We infer that the final configuration of two equally-sized cores corresponds to a state of dynamic equilibrium.

For such a dynamic equilibrium to exist, the rate of mass ejection from a large droplet must exceed that of ejection from a small droplet. Although the kinetics of the system are complex, this is likely due to the fact that the volume of a progeny droplet is proportional to the volume of its parent droplet,²⁶ so that for every fission event, a larger droplet ejects more mass than a smaller droplet. Moreover, large gold particles are more easily ionized since the absorption cross section scales approximately with r^3 for gold particles of radii $r \leq 20$ nm.³³ Whereas larger droplets also require a higher critical charge in order to undergo fission, this critical charge only scales with $r^{3/2}$.²⁶

Conclusion

In conclusion, we have presented an *in-situ* electron microscopy study of Coulomb fission in gold-core silica shell nanoparticles under femtosecond laser irradiation. Our experiments demonstrate the strength of *in-situ* observations on a single-particle level for elucidating complex mechanisms of laser reshaping of plasmonic nanoparticles that have only been incompletely understood and are difficult to study with other approaches. Our results also suggest a facile laser-mediated route for forming dual-core silica shell nanoparticles, which otherwise require complex synthetic procedures.^{42–45} Tuning the properties of the precursor

particles should improve the yield as well as the degree of alignment of the dual-cores. This should, for example, make it possible to fabricate linearly dichroic surfaces of aligned dual-gold-core silica shell particles.

References

- (1) Boisselier, E.; Astruc, D. Gold Nanoparticles in Nanomedicine: Preparations, Imaging, Diagnostics, Therapies and Toxicity. *Chem. Soc. Rev.* **2009**, *38*, 1759–1782.
- (2) Saha, K.; Agasti, S. S.; Kim, C.; Li, X.; Rotello, V. M. Gold Nanoparticles in Chemical and Biological Sensing. *Chem. Rev.* **2012**, *112*, 2739–2779.
- (3) Howes, P. D.; Chandrawati, R.; Stevens, M. M. Colloidal Nanoparticles as Advanced Biological Sensors. *Science* **2014**, *346*, 1247390.
- (4) Huang, X.; El-Sayed, I. H.; Qian, W.; El-Sayed, M. A. Cancer Cell Imaging and Photothermal Therapy in the Near-Infrared Region by Using Gold Nanorods. *J. Am. Chem. Soc.* **2006**, *128*, 2115–2120.
- (5) Brown, S. D.; Nativo, P.; Smith, J.-A.; Stirling, D.; Edwards, P. R.; Venugopal, B.; Flint, D. J.; Plumb, J. A.; Graham, D.; Wheate, N. J. Gold Nanoparticles for the Improved Anticancer Drug Delivery of the Active Component of Oxaliplatin. *J. Am. Chem. Soc.* **2010**, *132*, 4678–4684.
- (6) Rosi, N. L.; Giljohann, D. A.; Thaxton, C. S.; Lytton-Jean, A. K. R.; Han, M. S.; Mirkin, C. A. Oligonucleotide-Modified Gold Nanoparticles for Intracellular Gene Regulation. *Science* **2006**, *312*, 1027–1030.
- (7) Oliver-Meseguer, J.; Boronat, M.; Vidal-Moya, A.; Concepción, P.; Rivero-Crespo, M. Á.; Leyva-Pérez, A.; Corma, A. Generation and Reactivity of Electron-Rich Carbenes on the Surface of Catalytic Gold Nanoparticles. *J. Am. Chem. Soc.* **2018**, *140*, 3215–3218.
- (8) Eurenium, L.; Hägglund, C.; Olsson, E.; Kasemo, B.; Chakarov, D. Grating Formation by Metal-Nanoparticle-Mediated Coupling of Light into Waveguided Modes. *Nat. Photonics* **2008**, *2*, 360–364.
- (9) Teulle, A.; Bosman, M.; Girard, C.; Gurunatha, K. L.; Li, M.; Mann, S.; Dujardin, E. Multimodal Plasmonics in Fused Colloidal Networks. *Nat. Mater.* **2015**, *14*, 87–94.

- (10) Hashimoto, S.; Werner, D.; Uwada, T. Studies on the Interaction of Pulsed Lasers with Plasmonic Gold Nanoparticles toward Light Manipulation, Heat Management, and Nanofabrication. *J. Photochem. Photobiol. C Photochem. Rev.* **2012**, *13*, 28–54.
- (11) González-Rubio, G.; Guerrero-Martínez, A.; Liz-Marzán, L. M. Reshaping, Fragmentation, and Assembly of Gold Nanoparticles Assisted by Pulse Lasers. *Acc. Chem. Res.* **2016**, *49*, 678–686.
- (12) Kuhlicke, A.; Schietinger, S.; Matyssek, C.; Busch, K.; Benson, O. *In Situ* Observation of Plasmon Tuning in a Single Gold Nanoparticle during Controlled Melting. *Nano Lett.* **2013**, *13*, 2041–2046.
- (13) Herrmann, L. O.; Valev, V. K.; Tserkezis, C.; Barnard, J. S.; Kasera, S.; Scherman, O. A.; Aizpurua, J.; Baumberg, J. J. Threading Plasmonic Nanoparticle Strings with Light. *Nat. Commun.* **2014**, *5*, 4568.
- (14) González-Rubio, G.; Díaz-Núñez, P.; Rivera, A.; Prada, A.; Tardajos, G.; González-Izquierdo, J.; Bañares, L.; Llombart, P.; Macdowell, L. G.; Alcolea Palafox, M.; Liz-Marzán, L. M.; Peña-Rodríguez, O.; Guerrero-Martínez, A. Femtosecond Laser Reshaping Yields Gold Nanorods with Ultranarrow Surface Plasmon Resonances. *Science* **2017**, *358*, 640–644.
- (15) Inasawa, S.; Sugiyama, M.; Yamaguchi, Y. Laser-Induced Shape Transformation of Gold Nanoparticles below the Melting Point: The Effect of Surface Melting. *J. Phys. Chem. B* **2005**, *109*, 3104–3111.
- (16) Catone, D.; Ciavardini, A.; Di Mario, L.; Paladini, A.; Toschi, F.; Cartoni, A.; Fratoddi, I.; Venditti, I.; Alabastri, A.; Proietti Zaccaria, R.; O’Keeffe, P. Plasmon Controlled Shaping of Metal Nanoparticle Aggregates by Femtosecond Laser-Induced Melting. *J. Phys. Chem. Lett.* **2018**, *9*, 5002–5008.
- (17) Takami, A.; Kurita, H.; Koda, S. Laser-Induced Size Reduction of Noble Metal Particles. *J. Phys. Chem. B* **1999**, *103*, 1226–1232.

- (18) Pyatenko, A.; Wang, H.; Koshizaki, N.; Tsuji, T. Mechanism of Pulse Laser Interaction with Colloidal Nanoparticles: Interaction of Nanoparticle with Nanosecond Pulse Laser Is Clarified. *Laser Photonics Rev.* **2013**, *7*, 596–604.
- (19) Ahmadi, T. S.; Logunov, S. L.; El-Sayed, M. A. Picosecond Dynamics of Colloidal Gold Nanoparticles. *J. Phys. Chem.* **1996**, *100*, 8053–8056.
- (20) Hobbs, R. G.; Yang, Y.; Fallahi, A.; Keathley, P. D.; De Leo, E.; Kärtner, F. X.; Graves, W. S.; Berggren, K. K. High-Yield, Ultrafast, Surface Plasmon-Enhanced, Au Nanorod Optical Field Electron Emitter Arrays. *ACS Nano* **2014**, *8*, 11474–11482.
- (21) Hobbs, R. G.; Putnam, W. P.; Fallahi, A.; Yang, Y.; Kärtner, F. X.; Berggren, K. K. Mapping Photoemission and Hot-Electron Emission from Plasmonic Nanoantennas. *Nano Lett.* **2017**, *17*, 6069–6076.
- (22) Putnam, W. P.; Hobbs, R. G.; Keathley, P. D.; Berggren, K. K.; Kärtner, F. X. Optical-Field-Controlled Photoemission from Plasmonic Nanoparticles. *Nat. Phys.* **2017**, *13*, 335–339.
- (23) Li, B.; Yang, C.; Li, H.; Ji, B.; Lin, J.; Tomie, T. Thermionic Emission in Gold Nanoparticles under Femtosecond Laser Irradiation Observed with Photoemission Electron Microscopy. *AIP Adv.* **2019**, *9*, 025112.
- (24) Rayleigh, Lord. XX. On the Equilibrium of Liquid Conducting Masses Charged with Electricity. *Lond. Edinb. Dublin Philos. Mag. J. Sci.* **1882**, *14*, 184–186.
- (25) Duft, D.; Achtzehn, T.; Müller, R.; Huber, B. A.; Leisner, T. Rayleigh Jets from Levitated Microdroplets. *Nature* **2003**, *421*, 128–128.
- (26) Burton, J. C.; Taborek, P. Simulations of Coulombic Fission of Charged Inviscid Drops. *Phys. Rev. Lett.* **2011**, *106*, 144501.
- (27) Consta, S.; Sharawy, M.; Oh, M. I.; Malevanets, A. Advances in Modeling the Stability of Noncovalent Complexes in Charged Droplets with Applications in Electrospray Ionization-MS Experiments. *Anal. Chem.* **2017**, *89*, 8192–8202.

- (28) Werner, D.; Furube, A.; Okamoto, T.; Hashimoto, S. Femtosecond Laser-Induced Size Reduction of Aqueous Gold Nanoparticles: *In Situ* and Pump–Probe Spectroscopy Investigations Revealing Coulomb Explosion. *J. Phys. Chem. C* **2011**, *115*, 8503–8512.
- (29) Werner, D.; Hashimoto, S. Improved Working Model for Interpreting the Excitation Wavelength- and Fluence-Dependent Response in Pulsed Laser-Induced Size Reduction of Aqueous Gold Nanoparticles. *J. Phys. Chem. C* **2011**, *115*, 5063–5072.
- (30) Plech, A.; Kotaidis, V.; Lorenc, M.; Boneberg, J. Femtosecond Laser Near-Field Ablation from Gold Nanoparticles. *Nat. Phys.* **2006**, *2*, 44–47.
- (31) Rohner, T. C.; Lion, N.; Girault, H. H. Electrochemical and Theoretical Aspects of Electrospray Ionisation. *Phys. Chem. Chem. Phys.* **2004**, *6*, 3056–3068.
- (32) Fernández de la Mora, J. The Fluid Dynamics of Taylor Cones. *Annu. Rev. Fluid Mech.* **2007**, *39*, 217–243.
- (33) Oldenburg, S. J. *Light Scattering from Gold Nanoshells*. Ph.D. Dissertation, Rice University, Houston, TX, 2000.
- (34) Barwick, B.; Flannigan, D. J.; Zewail, A. H. Photon-Induced Near-Field Electron Microscopy. *Nature* **2009**, *462*, 902–906.
- (35) Park, S. T.; Lin, M.; Zewail, A. H. Photon-Induced Near-Field Electron Microscopy (PINEM): Theoretical and Experimental. *New J. Phys.* **2010**, *12*, 123028.
- (36) Mo, M. Z.; Chen, Z.; Li, R. K.; Dunning, M.; Witte, B. B. L.; Baldwin, J. K.; Fletcher, L. B.; Kim, J. B.; Ng, A.; Redmer, R.; Reid, A. H.; Shekhar, P.; Shen, X. Z.; Shen, M.; Sokolowski-Tinten, K.; Tsui, Y. Y.; Wang, Y. Q.; Zheng, Q.; Wang, X. J.; Glenzer, S. H. Heterogeneous to Homogeneous Melting Transition Visualized with Ultrafast Electron Diffraction. *Science* **2018**, *360*, 1451–1455.

- (37) Sivis, M.; Pazos-Perez, N.; Yu, R.; Alvarez-Puebla, R.; García de Abajo, F. J.; Ropers, C. Continuous-Wave Multiphoton Photoemission from Plasmonic Nanostars. *Commun. Phys.* **2018**, *1*, 13.
- (38) Mihaychuk, J. G.; Bloch, J.; Liu, Y.; van Driel, H. M. Time-Dependent Second-Harmonic Generation from the Si–SiO₂ Interface Induced by Charge Transfer. *Opt. Lett.* **1995**, *20*, 2063–2065.
- (39) Mihaychuk, J. G.; Shamir, N.; van Driel, H. M. Multiphoton Photoemission and Electric-Field-Induced Optical Second-Harmonic Generation as Probes of Charge Transfer across the Si/SiO₂ Interface. *Phys. Rev. B* **1999**, *59*, 2164–2173.
- (40) Seifert, G.; Kaempfe, M.; Berg, K.-J.; Graener, H. Femtosecond Pump-Probe Investigation of Ultrafast Silver Nanoparticle Deformation in a Glass Matrix. *Appl. Phys. B* **2000**, *71*, 795–800.
- (41) Podlipensky, A.; Abdolvand, A.; Seifert, G.; Graener, H. Femtosecond Laser Assisted Production of Dichroitic 3D Structures in Composite Glass Containing Ag Nanoparticles. *Appl. Phys. A* **2005**, *80*, 1647–1652.
- (42) Rodríguez-Fernández, D.; Langer, J.; Henriksen-Lacey, M.; Liz-Marzán, L. M. Hybrid Au–SiO₂ Core–Satellite Colloids as Switchable SERS Tags. *Chem. Mater.* **2015**, *27*, 2540–2545.
- (43) Smith, K. W.; Zhao, H.; Zhang, H.; Sánchez-Iglesias, A.; Grzelczak, M.; Wang, Y.; Chang, W.-S.; Nordlander, P.; Liz-Marzán, L. M.; Link, S. Chiral and Achiral Nanodumbbell Dimers: The Effect of Geometry on Plasmonic Properties. *ACS Nano* **2016**, *10*, 6180–6188.
- (44) Fang, L.; Wang, Y.; Liu, M.; Gong, M.; Xu, A.; Deng, Z. Dry Sintering Meets Wet Silver-Ion “Soldering”: Charge-Transfer Plasmon Engineering of Solution-Assembled Gold Nanodimers From Visible to Near-Infrared I and II Regions. *Angew. Chem. Int. Ed.* **2016**, *55*, 14296–14300.

- (45) Fang, L.; Liu, D.; Wang, Y.; Li, Y.; Song, L.; Gong, M.; Li, Y.; Deng, Z. Nanosecond-Laser-Based Charge Transfer Plasmon Engineering of Solution-Assembled Nanodimers. *Nano Lett.* **2018**, *18*, 7014–7020.
- (46) Aqra, F.; Ayyad, A. Theoretical Temperature-Dependence Surface Tension of Pure Liquid Gold. *Mater. Lett.* **2011**, *65*, 2124–2126.

Chapter 4

Real-Time Observation of Jumping and Spinning Nanodroplets

Introduction[§]

Despite the common occurrence of liquid drops, the fast morphological transformations they undergo in many everyday processes were only revealed once high-speed flash photography became available. Harold E. Edgerton's 1936 "Milk Drop Coronet" is a now iconic example that spectacularly captures the impact of a drop on a liquid surface.¹ More recently, flash photography has been used to observe the dynamics of highly charged micrometer-sized droplets undergoing Coulomb fission,^{2,3} elucidating a complicated fluid dynamics problem central to the electrospray ionization process.⁴⁻⁷ Due to the shorter length and faster time scales involved, such approaches cannot be extended to study nanodroplets – ubiquitous objects whose controlled generation and manipulation is crucial to a number of technologically important endeavors,⁸ such as jet printing with droplets of ever smaller dimensions.⁹ At the nanoscale, fluid dynamics may be significantly altered by specific nanoscale and surface effects,¹⁰⁻¹² making real-time observations crucial for developing a detailed understanding of these systems.

Here, we study the formation of so-called jumping nanodroplets, which are created when metal nanoprisms are flash-melted with a laser pulse.^{13,14} On a surface that repels the liquid metal, dewetting ensues and the nascent nanodroplet jumps off its substrate, reaching velocities of about 20 m/s. This process is closely related to a broader range of fundamentally important

[§] Reproduced from Olshin P.K., Voss J.M., Drabbels M., Lorenz U. J., *Struct. Dyn.* **7**, 011101 (2020), with the permission of AIP Publishing

Authors Contributions: P.K.O. and V.J.M. performed the experiments and analyzed the data; M.D. and U.J.L. supervised the project; U.J.L. wrote the manuscript with the contribution from all authors. P.K.O. and V.J.M. contributed equally to this work.

phenomena, including the dewetting of extended liquid films,¹⁵ the coalescence-induced jumping of water droplets from the hydrophobic surface of self-cleaning lotus leaves,¹⁶ and the process of droplets impacting a surface.¹⁷ Recently, jumping droplets have even been used to fabricate large arrays of uniform nanoparticles.¹⁸ The mechanism of this process has been investigated both by molecular and continuum dynamics simulations.^{19–21} Molecular dynamics simulations have recently also uncovered a related phenomenon in which nanodroplets are propelled from a structured graphene surface.²² However, in the absence of real-time observations, our understanding of the dynamics is incomplete.

We can estimate the timescale of the dewetting process using Rayleigh’s theory of liquid droplet oscillations.²³ The progression of the droplet from a flattened to a prolate shape that propels itself off the surface resembles a half-oscillation in the fundamental mode of the droplet, with the period τ given by

$$\tau = \sqrt{\frac{\rho r^3 \pi^2}{2\sigma}} \quad (1)$$

where r is the droplet radius, ρ the density, and σ the surface tension of the liquid.²³ For example, a liquid gold droplet of 270 nm diameter, which is the size of the droplets studied here, has a half-period of about 7 ns.

Experimental Setup

In order to directly observe jumping droplets of such small dimensions and on such short timescales, we employ time-resolved electron microscopy.^{24–27} We perform experiments with a modified JEOL 2200FS transmission electron microscope that we operate with an accelerating voltage of 160 kV. Briefly, a short laser pulse illuminates the sample to initiate the dynamics, which are subsequently imaged with a short electron pulse at a specific time delay. The electron pulse ($\sim 2 \cdot 10^4$ electrons, 1 ns) is generated by illuminating the extractor electrode of the electron gun with a UV laser pulse (266 nm, 1 ns FWHM, 2 μ J). This enables us to capture the morphological evolution of individual droplets with single nanosecond time resolution, more than an order of magnitude higher than previously achieved in related experiments on nanoscale fluid dynamics.^{26,28,29}

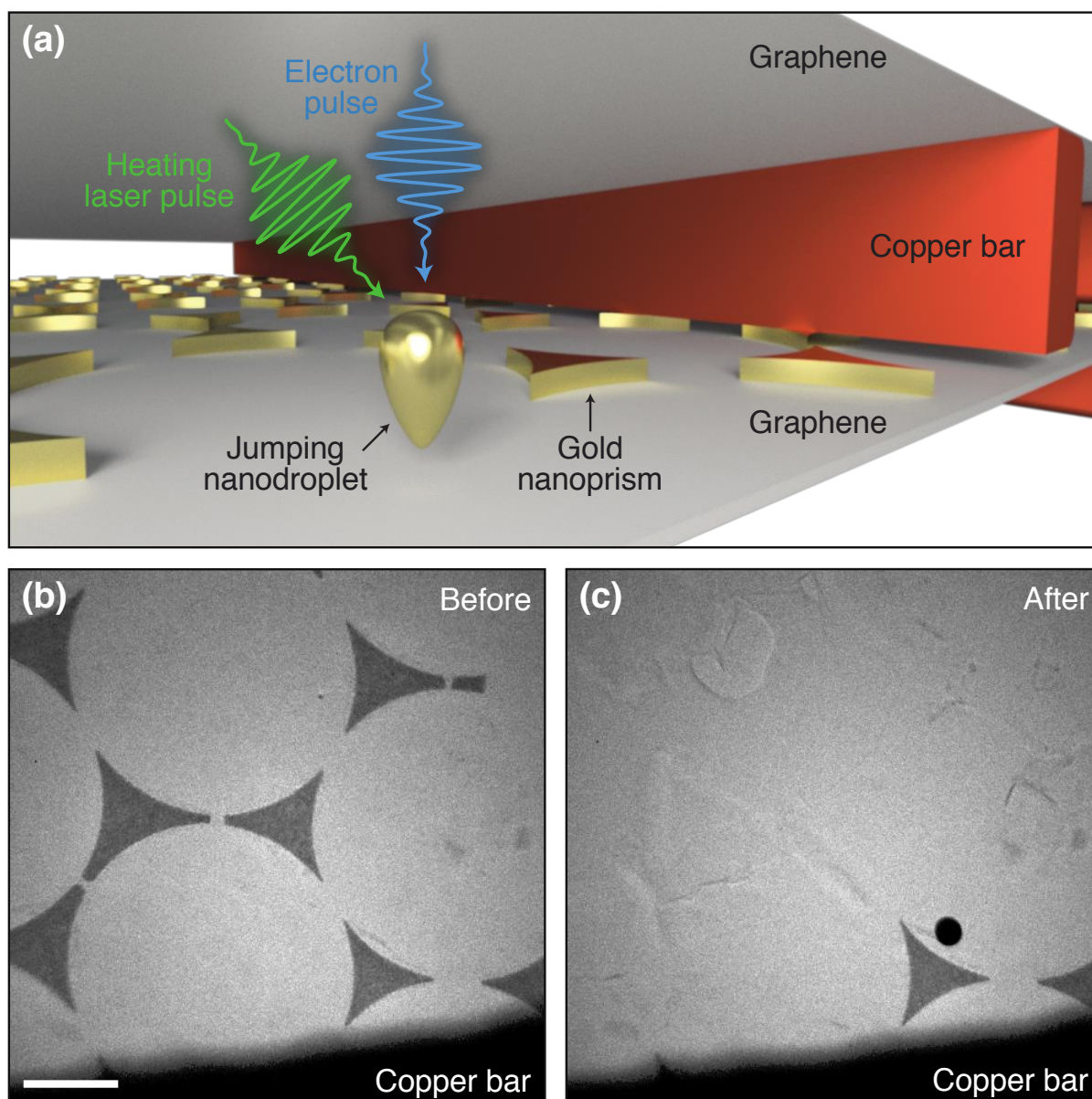


Figure 4-1. Gold nanoprisms as precursors of jumping nanodroplets. (a) Illustration of the sample geometry. Multilayer graphene decorated with gold nanoprisms is supported by an amorphous carbon/formvar thin film on a copper mesh. A second copper grid covered with graphene is added on top. (b) Micrograph of nanoprisms before and (c) after flash-melting with a laser pulse. (Scale bar, 1 μm .)

Figure 4-1(a) shows a sketch of the sample geometry used in our experiments. As precursors for the jumping nanodroplets, we use triangular gold nanoprisms (990 nm side length, 30 nm height). As in previous studies of jumping nanodroplets, the nanoprisms were fabricated with colloidal lithography.^{30–32} The nanoprisms reside on a multilayer graphene film, which is supported by an electron microscopy specimen grid (amorphous carbon/formvar film on 300 mesh copper). Another sample grid (multilayer graphene on 2000 mesh copper) tops the assembly. It reduces the total fluence incident on the thin film substrate that otherwise tends to rupture, and it prevents droplets from contaminating the instrument. A micrograph of a typical sample is shown in Fig. 4-1(b). Illumination *in situ* with a short laser pulse (515 nm, 3 ps FWHM, 1 μ J, focused to a spot size of 32 μ m FWHM) melts the structures and generates jumping nanodroplets. After the laser pulse, most of them disappear from view, and only a single spherical nanoparticle can be observed on the substrate [Fig. 4-1(c)]. Its diameter (310 nm) is larger than expected for a droplet resulting from a symmetric nanoprism (270 nm), suggesting that the droplet either deformed upon impact and solidified in a flattened shape, or that it originated from a larger structure not visible in the micrograph in Fig. 4-1(b). Figure 4-1(c) shows that some nanoprisms close to the copper bars remain. Since the melting laser pulse strikes the sample at a small angle with respect to the electron optical axis, these structures are likely partially shadowed by the copper bars. We also occasionally find that droplets resolidify on the uppermost graphene layer upon impact (Fig. S4-1).

Results and Discussion

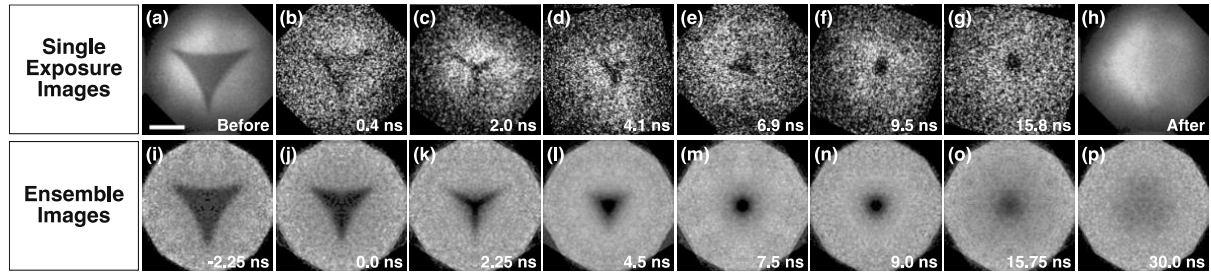


Figure 4-2. Snapshots of jumping nanodroplets and ensemble images. (a) A nanoprism is melted with a short laser pulse, and the (e) jumping nanodroplet is imaged at 6.9 ns with a single electron pulse. (h) After the jump, it leaves behind the bare substrate. (b–g) Representative snapshots of other nanodroplets at different stages of the dewetting process. (i–p) Ensemble averaged images of the dynamics. (Scale bar, 500 nm.)

We elucidate the fast fluid dynamics following the melting laser pulse by recording snapshots with individual, short electron pulses. Flash-melting the nanoprism in Fig. 4-2(a) creates a jumping nanodroplet that disappears from view [Fig. 4-2(h)]. A snapshot recorded at 6.9 ns reveals the transient structure of the collapsing droplet, which has contracted into a compact mass, but has not yet assumed a spherical geometry [Fig. 4-2(e)]. By repeating the experiment on other identical nanoprisms and taking snapshots at different time delays, we capture the entire evolution of the droplet morphology [Fig. 4-2(b–g)].

It is informative to analyze the dynamics both in terms of the average behavior of the ensemble, as well as the variations of individual trajectories. We obtain a movie of the ensemble dynamics by averaging over 500 individual exposures within 0.75 ns time-bins [Fig. 4-2(i–p), Fig. S4-2]. In this manner, we overcome the low signal-to-noise ratio afforded by an individual exposure, which results from the low number of electrons available in a single pulse.

Averaging requires the objects to be aligned to each other, which we achieve with the following procedure. Before melting with a laser pulse, each nanoprism is imaged with an accumulated dose of 1,000 electron pulses. The resulting high signal-to-noise micrograph is then aligned to a reference using phase correlation-based image registration.³³ The same rigid transformation is then applied to the time-resolved image of the jumping droplet that was subsequently recorded with a single electron pulse. In order to account for intensity variations of the electron beam, the time-resolved image is normalized by another micrograph (1,000 electron pulses) of the bare specimen support that is left behind after the droplet has jumped and disappeared from view. Finally, the time-resolved micrographs are sorted into 0.75 ns time-bins, symmetrized assuming C_{3v} symmetry, and averaged to yield the ensemble images of Fig. 4-2(i–p).

These ensemble images reveal that after flash-melting, the triangular structure immediately begins to collapse onto its center of mass [Fig. 4-2(j)]. Within 2 ns, the prism sides have retracted inward, so that the droplet transiently adopts a star-shaped configuration [Fig. 4-2(k)]. As the vertices continue to be pulled inward, the droplet develops a more compact, triangular outline [Fig. 4-2(l)], which approaches a circular shape around 7 ns [Fig. 4-2(m,n)]. At longer times, the droplet outline increasingly blurs [Fig. 4-2(o,p)]. The observed morphological evolution qualitatively agrees with both molecular and continuum dynamics simulations.^{19–21} For gold nanoprisms of 47 nm thickness and 405 nm side length on a silicon dioxide substrate, the collapsing droplet was predicted to maintain a triangular outline, whereas thinner nanoprisms (24 nm) adopted the transient star-shaped configuration we observe in our experiments.²¹

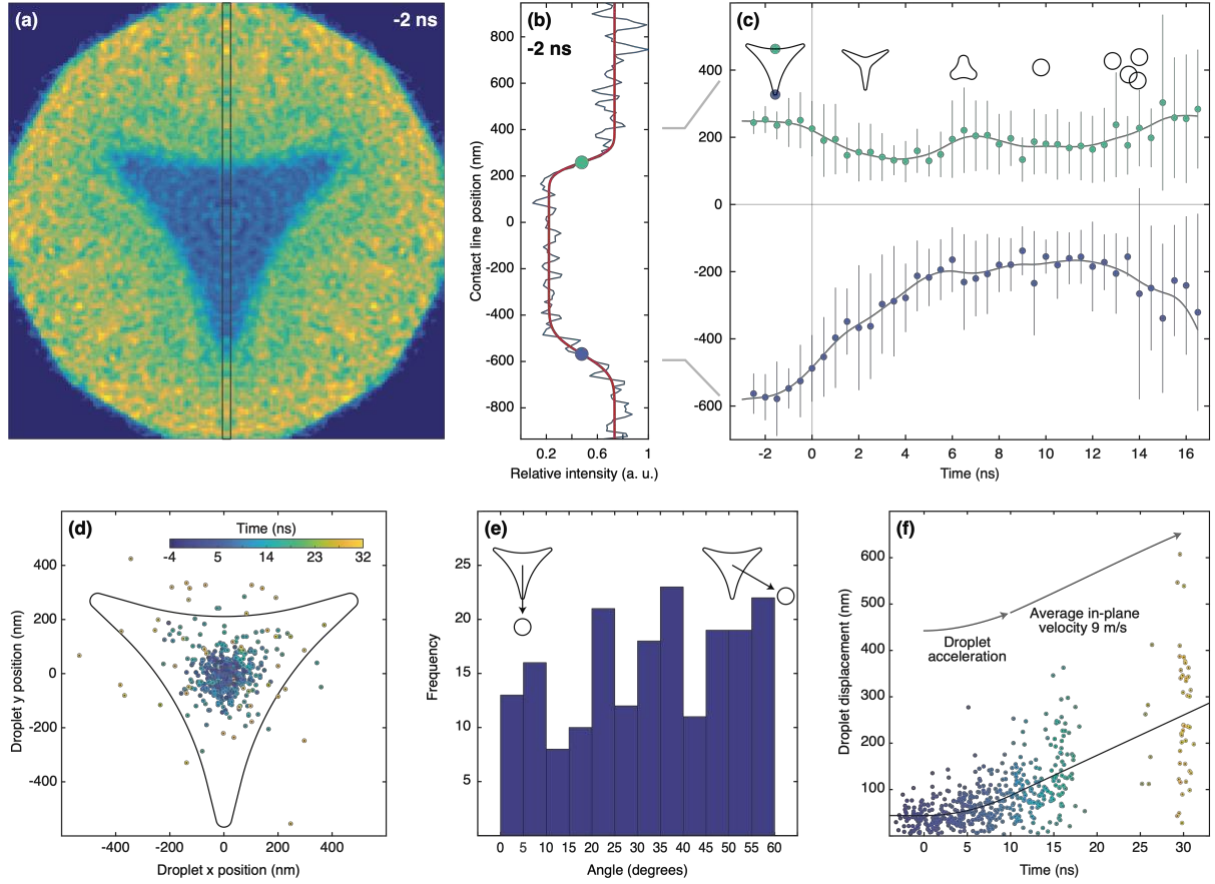


Figure 4-3. Analysis of the jumping nanodroplet dynamics. (a) Ensemble image of the nanoprism 2 ns before flash-melting. (b) Intensity profile (blue line) of the area marked in (a). The center positions of the boundaries (dots) are extracted from a fit (red line). (c) Center positions of the droplet boundaries as a function of time (dots). Vertical lines indicate the standard deviation of the average droplet boundary position. The grey lines serve as a guide for the eye. (d) Positions of the center of mass of the jumping droplets at different time delays (encoded by the color scale, inset). (e) Angular distribution of the jumping droplets in the time interval of 12-32 ns. (f) The displacements of the center of mass of droplets as a function of time (circles) is fit with a simple model (black line).

We analyze the dewetting dynamics as illustrated in Fig. 4-3(a). For each ensemble image, we calculate an intensity profile within the marked area and fit it with the product of

two error functions [Fig. 4-3(b)] **. This fit yields the average position of the droplet boundaries (dots), which are plotted in Fig. 4-3(c) as a function of time. The grey lines serve as a guide for the eye and represent splines of the data points. We find that the vertices, which exhibit the smallest radius of curvature and therefore the highest Laplace pressure, retract the fastest (bottom curve), reaching a speed of ~ 80 m/s within the one nanosecond resolution of the experiment. On the same timescale, the prism sides (top curve), reach a maximum speed of ~ 40 m/s. After 4 ns, the sides reverse direction and expand again until 6.5 ns. Individual snapshots at these time delays reveal inverted triangular outlines (Fig. 4-2(e)). This inversion has been predicted to occur after the vertices have collapsed onto the center of mass^{20,21} and is associated with a three-fold symmetric in-plane oscillation of the droplet, which then dampens out in less than one oscillation period. At long times (>10 ns), the droplet boundaries appear to move apart again. This is in fact due to a blurring of the ensemble images (Fig. 4-2(o,p)), which occurs as the droplets jump in different directions.

The fact that the droplets do not jump straight up, but instead have finite in-plane velocities is also evident in Fig. 4-3(d), which displays the position of individual droplet centers of mass at different time delays (encoded in color). After detaching from the graphene surface, the droplets increasingly spread out without any obvious angular preference (Fig. 4-3(e)). Figure 4-3(f) shows the absolute displacement of the droplets from the center of the nanoprism

** The transients for the retraction of the sides and vertices of the molten nanoprisms were obtained from vertical intensity profiles [area marked in Fig. 3(a)] that were calculated for the ensemble images (0.5 ns time-bins). The intensity profiles $I(x)$ were fit with the function

$$I(x) = a_1 - a_2 \left[\frac{1}{2} + \frac{1}{2} \operatorname{erf} \left(\frac{x - x_1}{\sqrt{2}\sigma_1} \right) \right] \cdot \left[\frac{1}{2} + \frac{1}{2} \operatorname{erf} \left(-\frac{x - x_2}{\sqrt{2}\sigma_2} \right) \right]$$

where $\operatorname{erf}(x)$ is the error function and a_1 , a_2 , x_1 , x_2 , σ_1 , and σ_2 are fit parameters [red line in Fig. 2(b)]. The average positions p_1 and p_2 of the retreating contact line reported in Fig. 3(c) were obtained from the values x at which the function $I(x)$ has dropped halfway to its minimum value $\min(I(x))$, so that $I(p_1) = I(p_2) = \frac{1}{2}\{a_1 - \min(I(x))\}$ and $|p_1 - p_2|$ represents the FWHM of the intensity profile. The spread in the position of the contact line are indicated in Fig. 3(c) as vertical lines of length $2\sigma_1$, and $2\sigma_2$, respectively. The gray line serves as a guide for the eye and represents a spline of the data points.

precursor as a function of time. At negative times, the scatter of the data reflects the accuracy with which we can determine droplet centers from single-exposure images. After flash-melting, the scatter increases rapidly as the droplets contract and finally jump. Assuming a constant average acceleration, a , the in-plane velocity increases linearly until the jump, so that we can fit the droplet displacement $\Delta r(t)$ with the piecewise function

$$\Delta r(t) = \begin{cases} r_0 & \text{for } t \leq 0 \\ r_0 + \frac{1}{2}at^2 & \text{for } t > 0 \text{ and } t \leq t_{jump} \\ r_0 + \frac{1}{2}at_{jump}^2 + at_{jump}(t - t_{jump}) & \text{for } t > t_{jump} \end{cases} \quad (2)$$

where r_0 , a , and t_{jump} are fit parameters [solid line in Fig. 4-3(f)]. We thus estimate that the droplets detach at $t_{jump} = 10$ ns. For comparison, theory predicts droplets to detach at 7 ns (5 ns) for smaller nanoprisms of 405 nm side length and 47 nm (24 nm) thickness.²¹ From the fit, we obtain an average in-plane velocity of the detached droplets of $at_{jump} = 9$ m/s, with some droplets reaching more than 25 m/s. Such large in-plane velocities point to substantial asymmetry of the dewetting process. In contrast, a fully symmetric contraction should create a droplet that jumps straight up.^{19–21} Evidently, while the average behavior of the ensemble agrees with theoretical predictions, the trajectories of individual droplets exhibit a certain degree of variation.

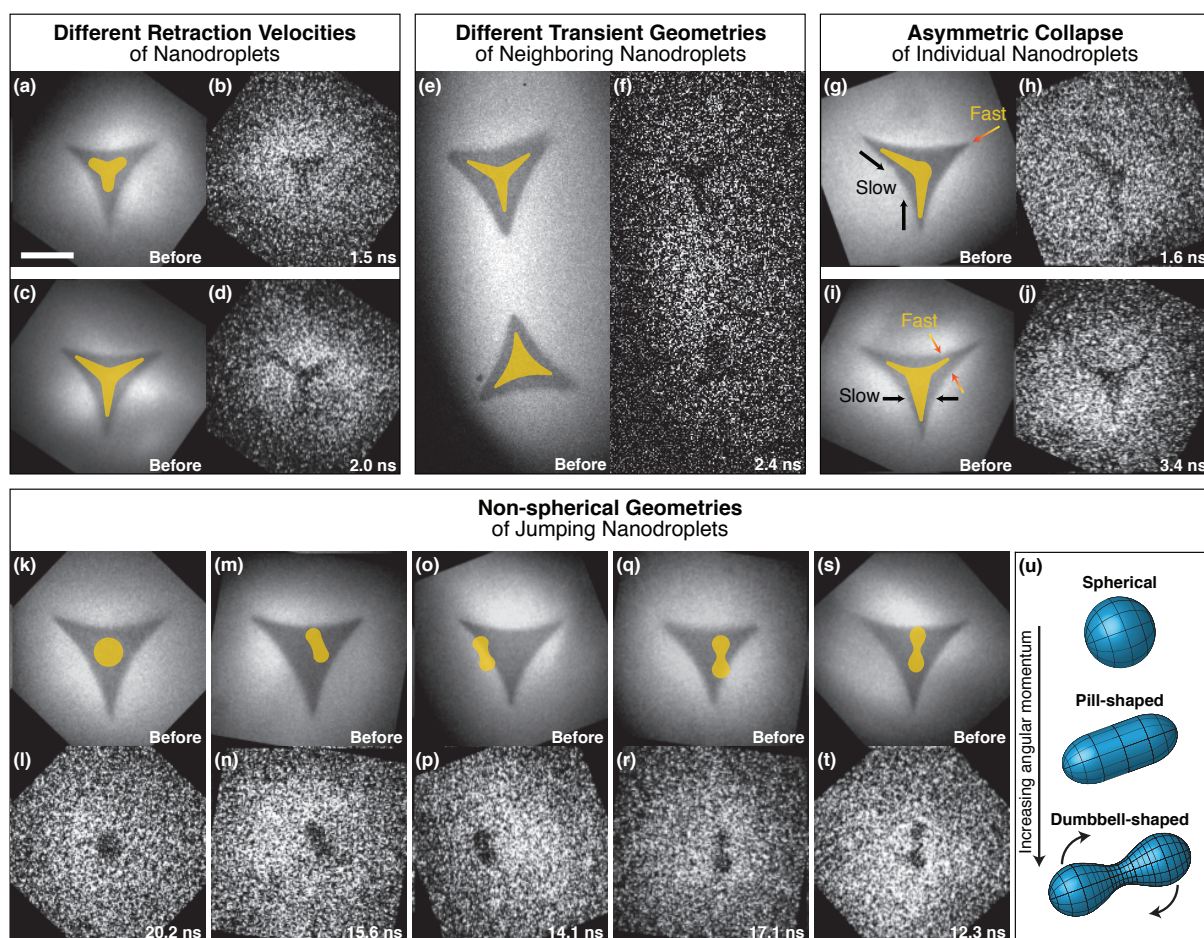


Figure 4-4. Heterogeneity of the nanoscale fluid dynamics and non-spherical geometries of free droplets. (a–d) Snapshots reveal different contraction velocities for different nanoprisms. (e,f) Simultaneously flash-melted nanoprisms adopt different transient geometries. (g–j) Individual nanoprisms reveal asymmetric transient configurations. (k–t) Snapshots of droplets after they have jumped reveal elongated as well as symmetric two-lobed geometries. Outlines of the transient configurations are superimposed on the images recorded before flash-melting. (Scale bar, 500 nm.) (u) Experimentally determined geometries of spinning macroscopic droplets, interpolated from photographs in Ref. 39.

Single-exposure images of jumping nanodroplets indeed reveal such variations in the trajectories of individual droplets (Fig. 4-4). The nanoprisms in Fig. 4-4(a,c) clearly contract

with different speeds, as evidenced by snapshots recorded at similar time delays [Fig. 4-4(b,d)]. For reference, outlines of the transient structures are superimposed on the images of the nanoprism precursors in Fig. 4-4(a,c). Even though the two neighboring nanoprisms in Fig. 4-4(e) are simultaneously flash-melted, a micrograph recorded at 2.4 ns reveals that they adopt different transient configurations, one of them more star-shaped, the other rather triangular [Fig. 4-4(f)]. Strikingly, even the collapse of a single nanodroplet can be highly asymmetric, as observed for the nanoprisms of Fig. 4-4(g,i) in the snapshots of Fig. 4-4(h,j), respectively.

We can exclude that the linear polarization of the heating laser induces the asymmetric nanodroplet geometries we observe. If we take the laser polarization into account when we align and average the single exposure images, we do not observe any significant asymmetry within experimental accuracy (Fig. S4-3). This suggests that any temperature differences induced by the linear laser polarization do not significantly alter the dynamics. Moreover, molecular dynamics simulations predict that even over a large temperature range of 700 K, dewetting timescales change only nominally,¹⁹ so that small variations in the droplet temperature should not have a significant effect. We can also exclude that the melting process interferes with the fluid dynamics. At the high temperatures that the nanoprisms initially reach after the laser pulse (heat transfer simulations in Fig. S4-4), heterogeneous melting of gold is known to occur in approximately 10 ps (Ref. 34), which is fast on the timescale of the dynamics studied here.

Instead, our observations point to friction as the origin of the observed heterogeneity. On a non-ideal surface, the moving contact line experiences friction as it dissipates energy through pinning and depinning on defects.^{35,36} Such defects can result from surface roughness, as it is present on the multilayer graphene surface used here. The thickness of the graphene substrate varies between six and eight layers on micron length scales. Therefore, many nanoprisms span

the boundary of a graphene flake, so that the contact line has to move over a microscopic step as the droplet contracts. Defects can also arise from chemical heterogeneity of the substrate, which locally alters the chemical properties of the surface and thus the contact angle of the liquid.^{35,36} A likely source of chemical defects is the colloidal lithography process that we have used to prepare the nanoprisms, following the methodology of previous studies of jumping nanodroplets.^{13,14} This process likely creates microscopic contaminants that locally alter the surface properties. We note that the angular distribution of the jumping droplets does not show any significant anisotropy [Fig. 4-3(e)], suggesting that the kinetic energy dissipated by each of the three retracting vertices varies independently.

Theoretical studies of jumping nanodroplets have so far only considered idealized surfaces and have therefore neglected the role of friction. In this respect, it is not surprising that on a realistic surface, friction will alter the trajectories of individual droplets and render the dynamics heterogeneous. However, we also observe that the interaction with surface defects gives rise to novel phenomena. Surprisingly, some of the droplets adopt non-spherical geometries in free space. After the droplets have detached from the surface (>10 ns), most appear round as expected [Fig. 4-4(k,l)]. However, a small fraction (approximately 5%) clearly feature either elongated or very distinct symmetric two-lobed shapes [Fig. 4-4(m-t)]. It is particularly striking that two-fold symmetric droplets are created from nanoprisms with three-fold symmetry.

The non-spherical droplets in Fig. 4-4(m-t) were captured at such late times that they must have already detached from the substrate. Interactions with the surface are therefore absent and cannot explain their geometry. In fact, we do not observe the symmetric two-lobed shapes at earlier time delays when the droplet is still in contact with the surface. Instead, this geometry is unique to droplets in free space. It is also unlikely that the non-spherical droplet shapes arise from large-amplitude oscillations.³⁷ Although simulations predict that the droplets

oscillate as they jump off the surface, these oscillations occur in the vertical direction and are of much smaller amplitude. They also rapidly dampen out as the droplet relaxes into a spherical geometry.^{19–21} This is not consistent with our observation of symmetric two-lobed geometries that persist at much later times.

Rather, it appears that the two-lobed shapes we observe correspond to the equilibrium geometries of spinning droplets.^{38,39} When angular momentum is imparted on a spherical droplet, it first deforms into an oblate equilibrium geometry and above a critical angular momentum, adopts a pill-like shape with two-fold symmetry [Fig. 4-4(u)]. At even higher angular momenta, the droplet evolves further into a dumbbell shape, as illustrated in Fig. 4-4(u). We note that these pill and dumbbell shapes^{38,39} bear close resemblance to the geometries observed in our experiments. Very recently, such geometries have been inferred for liquid helium nanodroplets from their diffraction patterns.^{40–43} In our experiments, the angular momentum imparted on the droplet likely has its origin in surface imperfections. On an ideal surface, the C_{3v} symmetry of the system dictates that the droplet cannot acquire angular momentum. However, the interaction of the liquid with surface defects breaks the symmetry of the system. Evidently, the resulting asymmetry of the dewetting process can generate sufficiently large angular momentum, so that dumbbell-shaped spinning droplets are formed.

For such dumbbell-shaped droplets, a unique relationship exists between the length R of the longest axis and the angular velocity Ω (Refs. 38,39). This allows us to estimate the rotational period of the droplets if we assume that the longest axis is perpendicular to the electron beam. For the droplets in Fig. 4-4(p,r,t), where this appears to be the case in good approximation, we measure $R = 180, 220, 230$ nm, respectively. We find that the relative elongations of the droplets $R^* = R/r$ do indeed fall within the range for which dumbbell shapes represent the most stable droplet geometry, $R^* \approx 1.1 - 2.1$. Through comparison with the numerical results of Ref. 38, we obtain rotational periods of approximately 26, 30, and 31 ns,

respectively. We note that the single nanosecond resolution of our experiment is therefore sufficient to resolve the characteristic shape of the spinning droplets.

Conclusion

Our experimental approach opens up new avenues for studying the fast morphological dynamics of nanodroplets through direct observation with time-resolved electron microscopy. To overcome the low number of electrons available in an electron pulse of sufficiently short duration, we average multiple snapshots of identical objects and obtain high signal-to-noise images of the dynamics. This approach should allow the investigation of the faster dynamics of even smaller droplets, for which nanoscale effects will become increasingly pronounced. Our real-time observations add details to the mechanism of the jumping droplets, highlighting the role that surface imperfections play in steering the dynamics. Since by its very nature, friction is a nanoscale phenomenon,⁴⁴ such studies of friction on its inherent length scale promise nanoscopic insights that are inaccessible to macroscopic experiments.^{35,36} An intriguing prospect would be to directly observe the interaction of the moving nanodroplets with a single, well-defined nanoscale defect that is lithographically written onto the surface. For example, molecular dynamics simulations have recently shown that water nanodroplets can be accelerated to high velocities when placed on a wedge-shaped defect on a graphene surface.²² Here, we present evidence that surface defects can be employed to spin nanodroplets to high angular momenta, suggesting new ways of manipulating these nanoscale systems. For macroscopic jumping droplets, the use of patterned surfaces to induce angular momentum has only recently been demonstrated.⁴⁵

References

- (1) Edgerton, H. E. *Milk Drop Coronet*; 1936.
- (2) Duft, D.; Achtzehn, T.; Muller, R.; Huber, B. A.; Leisner, T. Coulomb Fission - Rayleigh Jets from Levitated Microdroplets. *Nature* **2003**, *421* (6919), 128–128.
- (3) Grimm, R. L.; Beauchamp, J. L. Dynamics of Field-Induced Droplet Ionization: Time-Resolved Studies of Distortion, Jetting, and Progeny Formation from Charged and Neutral Methanol Droplets Exposed to Strong Electric Fields. *J. Phys. Chem. B* **2005**, *109* (16), 8244–8250.
- (4) Fernández de la Mora, J. The Fluid Dynamics of Taylor Cones. *Annu. Rev. Fluid Mech.* **2007**, *39* (1), 217–243.
- (5) Fenn, J. B.; Mann, M.; Meng, C. K.; Wong, S. F.; Whitehouse, C. M. Electrospray Ionization for Mass-Spectrometry of Large Biomolecules. *Science* **1989**, *246* (4926), 64–71.
- (6) Consta, S.; Oh, M. I.; Malevanets, A. New Mechanisms of Macroion-Induced Disintegration of Charged Droplets. *Chem. Phys. Lett.* **2016**, *663*, 1–12.
- (7) Oh, M. I.; Malevanets, A.; Paliy, M.; Frenkel, D.; Consta, S. When Droplets Become Stars: Charged Dielectric Droplets beyond the Rayleigh Limit. *Soft Matter* **2017**, *13* (46), 8781–8795.
- (8) Wang, Z. M. *Nanodroplets*; Springer Science & Business Media, 2014.
- (9) Park, J. U.; Hardy, M.; Kang, S. J.; Barton, K.; Adair, K.; Mukhopadhyay, D. K.; Lee, C. Y.; Strano, M. S.; Alleyne, A. G.; Georgiadis, J. G.; et al. High-Resolution Electrohydrodynamic Jet Printing. *Nat. Mater.* **2007**, *6* (10), 782–789.
- (10) Eijkel, J. C. T.; van den Berg, A. Nanofluidics: What Is It and What Can We Expect from It? *Microfluid. Nanofluidics* **2005**, *1* (3), 249–267.
- (11) Bocquet, L.; Barrat, J.-L. Flow Boundary Conditions from Nano- to Micro-Scales. *Soft Matter* **2007**, *3* (6), 685–693.

- (12) Secchi, E.; Marbach, S.; Niguès, A.; Stein, D.; Siria, A.; Bocquet, L. Massive Radius-Dependent Flow Slippage in Carbon Nanotubes. *Nature* **2016**, *537* (7619), 210–213.
- (13) Habenicht, A.; Olapinski, M.; Burmeister, F.; Leiderer, P.; Boneberg, J. Jumping Nanodroplets. *Science* **2005**, *309* (5743), 2043–2045.
- (14) Boneberg, J.; Habenicht, A.; Benner, D.; Leiderer, P.; Trautvetter, M.; Pfahler, C.; Plettl, A.; Ziemann, P. Jumping Nanodroplets: A New Route towards Metallic Nano-Particles. *Appl. Phys. A* **2008**, *93* (2), 415–419.
- (15) Herminghaus, S.; Jacobs, K.; Mecke, K.; Bischof, J.; Fery, A.; Ibn-Elhaj, M.; Schlagowski, S. Spinodal Dewetting in Liquid Crystal and Liquid Metal Films. *Science* **1998**, *282* (5390), 916–919.
- (16) Enright, R.; Miljkovic, N.; Sprittles, J.; Nolan, K.; Mitchell, R.; Wang, E. N. How Coalescing Droplets Jump. *ACS Nano* **2014**, *8* (10), 10352–10362.
- (17) Bergeron, V.; Bonn, D.; Martin, J. Y.; Vovelle, L. Controlling Droplet Deposition with Polymer Additives. *Nature* **2000**, *405*, 772.
- (18) Kuznetsov, A. I.; Evlyukhin, A. B.; Gonçalves, M. R.; Reinhardt, C.; Koroleva, A.; Arnedillo, M. L.; Kiyan, R.; Marti, O.; Chichkov, B. N. Laser Fabrication of Large-Scale Nanoparticle Arrays for Sensing Applications. *ACS Nano* **2011**, *5* (6), 4843–4849.
- (19) Fuentes-Cabrera, M.; Rhodes, B. H.; Baskes, M. I.; Terrones, H.; Fowlkes, J. D.; Simpson, M. L.; Rack, P. D. Controlling the Velocity of Jumping Nanodroplets *Via* Their Initial Shape and Temperature. *ACS Nano* **2011**, *5* (9), 7130–7136.
- (20) Afkhami, S.; Kondic, L. Numerical Simulation of Ejected Molten Metal Nanoparticles Liquified by Laser Irradiation: Interplay of Geometry and Dewetting. *Phys. Rev. Lett.* **2013**, *111* (3), 034501.
- (21) Afkhami, S.; Kondic, L. On the Dewetting of Liquefied Metal Nanostructures. *J. Eng. Math.* **2015**, *94* (1), 5–18.

- (22) Papadopoulou, E.; Megaridis, C. M.; Walther, J. H.; Koumoutsakos, P. Ultrafast Propulsion of Water Nanodroplets on Patterned Graphene. *ACS Nano* **2019**, *13* (5), 5465–5472.
- (23) Lord Rayleigh, F. R. S. On the Equilibrium of Liquid Conducting Masses Charged with Electricity. *Philos. Mag. Ser. 5* **1882**, *14* (87), 184–186.
- (24) Zewail, A. H. Four-Dimensional Electron Microscopy. *Science* **2010**, *328* (5975), 187–193.
- (25) Browning, N. D.; Bonds, M. A.; Campbell, G. H.; Evans, J. E.; LaGrange, T.; Jungjohann, K. L.; Masiel, D. J.; McKeown, J.; Mehraeen, S.; Reed, B. W.; et al. Recent Developments in Dynamic Transmission Electron Microscopy. *Curr. Opin. Solid State Mater. Sci.* **2012**, *16* (1), 23–30.
- (26) Lorenz, U. J.; Zewail, A. H. Observing Liquid Flow in Nanotubes by 4D Electron Microscopy. *Science* **2014**, *344* (6191), 1496–1500.
- (27) Voss, J. M.; Olshin, P. K.; Charbonnier, R.; Drabbels, M.; Lorenz, U. J. *In Situ* Observation of Coulomb Fission of Individual Plasmonic Nanoparticles. *ACS Nano* **2019**, *13* (11), 12445–12451.
- (28) McKeown, J. T.; Roberts, N. A.; Fowlkes, J. D.; Wu, Y.; LaGrange, T.; Reed, B. W.; Campbell, G. H.; Rack, P. D. Real-Time Observation of Nanosecond Liquid-Phase Assembly of Nickel Nanoparticles via Pulsed-Laser Heating. *Langmuir* **2012**, *28* (49), 17168–17175.
- (29) Hihath, S.; Santala, M. K.; Cen, X.; Campbell, G.; van Benthem, K. High Speed Direct Imaging of Thin Metal Film Ablation by Movie-Mode Dynamic Transmission Electron Microscopy. *Sci. Rep.* **2016**, *6* (1), 1–7.
- (30) Hulteen, J. C.; Van Duyne, R. P. Nanosphere Lithography: A Materials General Fabrication Process for Periodic Particle Array Surfaces. *J. Vac. Sci. Technol. Vac. Surf. Films* **1995**, *13* (3), 1553–1558.

- (31) Cong, C. X.; Yu, T.; Ni, Z. H.; Liu, L.; Shen, Z. X.; Huang, W. Fabrication of Graphene Nanodisk Arrays Using Nanosphere Lithography. *J. Phys. Chem. C* **2009**, *113* (16), 6529–6532.
- (32) Lotito, V.; Zambelli, T. Self-Assembly and Nanosphere Lithography for Large-Area Plasmonic Patterns on Graphene. *J. Colloid Interface Sci.* **2015**, *447*, 202–210.
- (33) Reddy, B. S.; Chatterji, B. N. An FFT-Based Technique for Translation, Rotation, and Scale-Invariant Image Registration. *IEEE Trans. Image Process.* **1996**, *5* (8), 1266–1271.
- (34) Mo, M. Z.; Chen, Z.; Li, R. K.; Dunning, M.; Witte, B. B. L.; Baldwin, J. K.; Fletcher, L. B.; Kim, J. B.; Ng, A.; Redmer, R.; et al. Heterogeneous to Homogeneous Melting Transition Visualized with Ultrafast Electron Diffraction. *Science* **2018**, *360*, 1451–1455.
- (35) de Gennes, P.-G.; Brochard-Wyart, F.; Quere, D. *Capillarity and Wetting Phenomena: Drops, Bubbles, Pearls, Waves*; Springer: New York, 2004.
- (36) Bonn, D.; Eggers, J.; Indekeu, J.; Meunier, J.; Rolley, E. Wetting and Spreading. *Rev. Mod. Phys.* **2009**, *81* (2), 739–805.
- (37) Jiang, Y. J.; Umemura, A.; Law, C. K. An Experimental Investigation on the Collision Behaviour of Hydrocarbon Droplets. *J. Fluid Mech.* **1992**, *234* (1), 171.
- (38) Brown, R. A.; Scriven, L. E. The Shape and Stability of Rotating Liquid Drops. *Proc. R. Soc. Math. Phys. Eng. Sci.* **1980**, *371*, 331–357.
- (39) Liao, L.; Hill, R. J. A. Shapes and Fissility of Highly Charged and Rapidly Rotating Levitated Liquid Drops. *Phys. Rev. Lett.* **2017**, *119* (11), 114501.
- (40) Gomez, L. F.; Ferguson, K. R.; Cryan, J. P.; Bacellar, C.; Tanyag, R. M. P.; Jones, C.; Schorb, S.; Anielski, D.; Belkacem, A.; Bernando, C.; et al. Shapes and Vorticities of Superfluid Helium Nanodroplets. *Science* **2014**, *345* (6199), 906–909.

- (41) Bernando, C.; Tanyag, R. M. P.; Jones, C.; Bacellar, C.; Bucher, M.; Ferguson, K. R.; Rupp, D.; Ziemkiewicz, M. P.; Gomez, L. F.; Chatterley, A. S.; et al. Shapes of Rotating Superfluid Helium Nanodroplets. *Phys. Rev. B* **2017**, *95* (6).
- (42) Langbehn, B.; Sander, K.; Ovcharenko, Y.; Peltz, C.; Clark, A.; Coreno, M.; Cucini, R.; Drabbels, M.; Finetti, P.; Di Fraia, M.; et al. Three-Dimensional Shapes of Spinning Helium Nanodroplets. *Phys. Rev. Lett.* **2018**, *121* (25), 255301.
- (43) Rupp, D.; Monserud, N.; Langbehn, B.; Sauppe, M.; Zimmermann, J.; Ovcharenko, Y.; Möller, T.; Frassetto, F.; Poletto, L.; Trabattoni, A.; et al. Coherent Diffractive Imaging of Single Helium Nanodroplets with a High Harmonic Generation Source. *Nat. Commun.* **2017**, *8* (1).
- (44) Urbakh, M.; Klafter, J.; Gourdon, D.; Israelachvili, J. The Nonlinear Nature of Friction. *Nature* **2004**, *430* (6999), 525–528.
- (45) Li, H.; Fang, W.; Li, Y.; Yang, Q.; Li, M.; Li, Q.; Feng, X.-Q.; Song, Y. Spontaneous Droplets Gyration via Asymmetric Self-Splitting on Heterogeneous Surfaces. *Nat. Commun.* **2019**, *10* (1), 1–6.

Chapter 5

Conclusion and Outlook

This dissertation covers the work conducted in the Laboratory of Molecular Nanodynamics on the development of a time-resolved resolved transmission electron microscope and describes some applications of the instrument.

In **Chapter 2**, the design as well as the characterization of the device are presented. Front illumination of the Schottky emitter allows for the generation of high brightness electron pulses from the Schottky filament as well as high current pulses from the extractor electrode. This flexibility expands the number of experiments that are accessible with the instrument. For example, the electron beam from the tungsten tip can be used for stroboscopic experiments in which high spatial coherence or high brightness are required. At the same time, photoemission from the extractor can be useful for time-resolved experiments that require high numbers of electrons in a pulse, for example, for single shot imaging and diffraction.

Chapter 3 presents an *in situ* study of Coulomb fission of gold core silica shell nanoparticles. Our study reveals that under femtosecond laser irradiation the gold cores can be fragmented so that aligned dual-core nanoparticles are formed. Our observations are consistent with a mechanism in which electrons are preferentially emitted from the gold core along the laser polarization direction. The resulting anisotropic charge distribution in the silica shell then determines the direction in which progeny droplets are ejected. With continued irradiation, the emitted droplets coalesce into a second particle within the silica shell, so that the system evolves into a dual-core particle

This experiment demonstrates that the combination of an electron microscope with a laser system provides great opportunities for *in situ* studies of the interactions of matter with

intense laser pulses at the nanoscale. Laser machining ¹ as well as the laser induced formation and modification of nanoparticles ² are among the many processes that can be studied with this approach. Real-time observation can significantly advance research in these fields and provide important information regarding the mechanism of laser induced transformations.

Chapter 4 describes the study of so-called jumping nanodroplets. In this experiment, picosecond laser pulses initiated melting of triangular gold nanoprisms, followed by their contraction into spheres and detachment from their substrate. The dynamics of the process were recorded with a temporal resolution of one nanosecond. In these experiments we took advantage of the unique design of the optical setup for the probe laser that allows us to generate high current electron pulses. Our work expands the field of microscale fluid dynamics to even shorter time and length scales, which can be beneficial for studying technologically important phenomena involving nanodroplets, such as friction, dewetting, and the effect of the surface defects on their propagation.

The field of time-resolved transmission electron microscopy is differentiating into many distinct directions, including the design of laser free instruments ³⁻¹², improving the temporal resolution by inserting RF cavities into the column ^{13,14}, performing new types of experiments based on the quantum manipulation of electron pulses ^{15,16}, studies with sub-femtosecond temporal resolution ¹⁷⁻²⁰, and improving the spatial resolution. In my opinion, expanding the method to shorter time and length scales is one of the most important objectives.

The temporal resolution of our instrument can be improved in two ways. First, using shorter laser pulses for the electron photoemission will significantly decrease the duration of the electron pulses. Reducing of the energy spread of the pulses will also limit the broadening of the pulses in the temporal domain. To minimize the energy spread of the electron pulses, a probe laser with a longer wavelength should be used. In the absence of Boersch effect, the energy spread of 1.8 eV is determined by high excess energy of electrons emitted with the

fourth harmonic (258 nm, 4.8 eV) of a 1030 nm laser. Such a high photon energy exceeds the work function of the W/ZrO₂ emitter by almost 2 eV, leading to the significant broadening. To reduce the energy distribution, third (343 nm, 3.6 eV) or even second (515 nm, 2.4 eV) harmonics should be used. Although the energy of the second harmonic is smaller than the work function, photoemission is still possible due to the Schottky effect and presence of thermally excited electrons ^{21,22}. If pulses with longer wavelengths are used, photoemission from the extractor surface will not be possible, as the work function of stainless steel is close to the energy of 258 nm photons. To keep the advantages of different electron sources, beams with different wavelengths can be combined.

Another important direction of the development of time-resolved electron microscopy involves attempts to enable atomic-resolution observations of nanoscale dynamics in real space. Single shot imaging suffers from severe space charge effects that limit the spatial resolution to several nanometers ²³. In stroboscopic experiments, in which the Coulomb interactions are minimized by using less than one electron per pulse, long acquisition times and laser induced drift of the sample prevent high-resolution imaging. Although it should be noted that images with atomic resolution have been recorded with ultrafast electron pulses in the absence of the pump laser pulses ^{24,25}. Thus, atomic resolution in single shot experiments can only be achieved by increasing the pulse duration. In our group we have modified a second TEM and installed the same illumination system for the probe laser as described in this thesis. With this instrument, we have demonstrated that 2 Å resolution can be reached with electron pulses of several microseconds ²⁶. In these experiments, the electron pulses are generated with an electrostatic deflector, and the beam current is increased by several times by heating a Schottky filament with a microsecond laser pulse ²⁷. To reach sub-μs temporal resolution, high quality pulses with higher currents must be obtained, and optimization of the geometry of the filament, extraction fields, and the heating laser power might be necessary.

Time-resolved TEM has proven to be an extremely powerful technique for studying fast and ultrafast dynamics with high spatial resolution. Being a relatively new research area, the ultimate performance of the method has not been reached yet. Therefore, working in a rapidly developing field like this inspires researchers to propose new concepts and perform unique experiments. The main output of such an approach, namely, development of new instruments and experimental techniques, opens up new avenues in studying physical and chemical properties of various materials, light-matter interactions, and the coherent manipulation of electron wave packets with light.

References

- (1) Lei, S.; Zhao, X.; Yu, X.; Hu, A.; Vukelic, S.; Jun, M. B. G.; Joe, H.-E.; Yao, Y. L.; Shin, Y. C. Ultrafast Laser Applications in Manufacturing Processes: A State-of-the-Art Review. *Journal of Manufacturing Science and Engineering* **2020**, *142* (3), 031005.
- (2) González-Rubio, G.; Díaz-Núñez, P.; Rivera, A.; Prada, A.; Tardajos, G.; González-Izquierdo, J.; Bañares, L.; Llombart, P.; Macdowell, L. G.; Alcolea Palafox, M.; Liz-Marzán, L. M.; Peña-Rodríguez, O.; Guerrero-Martínez, A. Femtosecond Laser Reshaping Yields Gold Nanorods with Ultranarrow Surface Plasmon Resonances. *Science* **2017**, *358* (6363), 640–644.
- (3) Weppelman, I. G. C.; Moerland, R. J.; Hoogenboom, J. P.; Kruit, P. Concept and Design of a Beam Blanker with Integrated Photoconductive Switch for Ultrafast Electron Microscopy. *Ultramicroscopy* **2018**, *184*, 8–17.
- (4) Verhoeven, W.; van Rens, J. F. M.; Kieft, E. R.; Mutsaers, P. H. A.; Luiten, O. J. High Quality Ultrafast Transmission Electron Microscopy Using Resonant Microwave Cavities. *Ultramicroscopy* **2018**, *188*, 85–89.
- (5) van Rens, J. F. M.; Verhoeven, W.; Kieft, E. R.; Mutsaers, P. H. A.; Luiten, O. J. Dual Mode Microwave Deflection Cavities for Ultrafast Electron Microscopy. *Appl. Phys. Lett.* **2018**, *113* (16), 163104.
- (6) Weppelman, I. G. C.; Moerland, R. J.; Zhang, L.; Kieft, E.; Kruit, P.; Hoogenboom, J. P. Pulse Length, Energy Spread, and Temporal Evolution of Electron Pulses Generated with an Ultrafast Beam Blanker. *Structural Dynamics* **2019**, *6* (2), 024102.
- (7) Verhoeven, W.; van Rens, J. F. M.; Kemper, A. H.; Rietman, E. H.; van Doorn, H. A.; Koole, I.; Kieft, E. R.; Mutsaers, P. H. A.; Luiten, O. J. Design and Characterization of Dielectric Filled TM₁₁₀ Microwave Cavities for Ultrafast Electron Microscopy. *Review of Scientific Instruments* **2019**, *90* (8), 083703.

- (8) Toonen, W. F.; Stragier, X. F. D.; Mutsaers, P. H. A.; Luiten, O. J. Gigahertz Repetition Rate Thermionic Electron Gun Concept. *Phys. Rev. Accel. Beams* **2019**, *22* (12), 123401.
- (9) Sannomiya, T.; Arai, Y.; Nagayama, K.; Nagatani, Y. Transmission Electron Microscope Using a Linear Accelerator. *Phys. Rev. Lett.* **2019**, *123* (15), 150801.
- (10) Zhang, L.; Garming, M. W. H.; Hoogenboom, J. P.; Kruit, P. Beam Displacement and Blur Caused by Fast Electron Beam Deflection. *Ultramicroscopy* **2020**, *211*, 112925.
- (11) Fu, X.; Wang, E.; Zhao, Y.; Liu, A.; Montgomery, E.; Gokhale, V. J.; Gorman, J. J.; Jing, C.; Lau, J. W.; Zhu, Y. Direct Visualization of Electromagnetic Wave Dynamics by Laser-Free Ultrafast Electron Microscopy. *Sci. Adv.* **2020**, *6* (40), eabc3456.
- (12) Lau, J. W.; Schliep, K. B.; Katz, M. B.; Gokhale, V. J.; Gorman, J. J.; Jing, C.; Liu, A.; Zhao, Y.; Montgomery, E.; Choe, H.; Rush, W.; Kanareykin, A.; Fu, X.; Zhu, Y. Laser-Free GHz Stroboscopic Transmission Electron Microscope: Components, System Integration, and Practical Considerations for Pump–Probe Measurements. *Review of Scientific Instruments* **2020**, *91* (2), 021301.
- (13) Gliserin, A.; Walbran, M.; Krausz, F.; Baum, P. Sub-Phonon-Period Compression of Electron Pulses for Atomic Diffraction. *Nat Commun* **2015**, *6* (1), 8723.
- (14) Sun, S.; Sun, X.; Bartles, D.; Wozniak, E.; Williams, J.; Zhang, P.; Ruan, C.-Y. Direct Imaging of Plasma Waves Using Ultrafast Electron Microscopy. *Structural Dynamics* **2020**, *7* (6), 064301.
- (15) Di Giulio, V.; Kociak, M.; de Abajo, F. J. G. Probing Quantum Optical Excitations with Fast Electrons. *Optica* **2019**, *6* (12), 1524.
- (16) Reinhardt, O.; Kaminer, I. Theory of Shaping Electron Wavepackets with Light. *ACS Photonics* **2020**, *7* (10), 2859–2870.
- (17) Morimoto, Y.; Baum, P. Diffraction and Microscopy with Attosecond Electron Pulse Trains. *Nature Phys* **2018**, *14* (3), 252–256.

- (18) Kozák, M.; Schönenberger, N.; Hommelhoff, P. Ponderomotive Generation and Detection of Attosecond Free-Electron Pulse Trains. *Phys. Rev. Lett.* **2018**, *120* (10), 103203.
- (19) Schönenberger, N.; Mittelbach, A.; Yousefi, P.; McNeur, J.; Niedermayer, U.; Hommelhoff, P. Generation and Characterization of Attosecond Microbunched Electron Pulse Trains via Dielectric Laser Acceleration. *Phys. Rev. Lett.* **2019**, *123* (26), 264803.
- (20) Ryabov, A.; Thurner, J. W.; Nabben, D.; Tsarev, M. V.; Baum, P. Attosecond Metrology in a Continuous-Beam Transmission Electron Microscope. *Sci. Adv.* **2020**, *6* (46), eabb1393.
- (21) Cook, B.; Brongseest, M.; Hagen, K.; Kruit, P. Improving the Energy Spread and Brightness of Thermal-Field (Schottky) Emitters with PHAST—PHoto Assisted Schottky Tip. *Ultramicroscopy* **2009**, *109* (5), 403–412.
- (22) Israel, Y.; Bowman, A. J.; Klopfer, B. B.; Koppell, S. A.; Kasevich, M. A. High-Extinction Electron Pulses by Laser-Triggered Emission from a Schottky Emitter. *Applied Physics Letters* **2020**, *5*.
- (23) LaGrange, T.; Campbell, G. H.; Reed, B. W.; Taheri, M.; Pesavento, J. B.; Kim, J. S.; Browning, N. D. Nanosecond Time-Resolved Investigations Using the in Situ of Dynamic Transmission Electron Microscope (DTEM). *Ultramicroscopy* **2008**, *108* (11), 1441–1449.
- (24) Cao, G.; Sun, S.; Li, Z.; Tian, H.; Yang, H.; Li, J. Clocking the Anisotropic Lattice Dynamics of Multi-Walled Carbon Nanotubes by Four-Dimensional Ultrafast Transmission Electron Microscopy. *Sci Rep* **2015**, *5* (1), 8404.
- (25) Bucker, K.; Picher, M.; Crégut, O.; LaGrange, T.; Reed, B. W.; Park, S. T.; Masiel, D. J.; Banhart, F. Electron Beam Dynamics in an Ultrafast Transmission Electron Microscope with Wehnelt Electrode. *Ultramicroscopy* **2016**, *171*, 8–18.

- (26) Olshin, P. K.; Bongiovanni, G.; Drabbels, M.; Lorenz, U. J. Atomic-Resolution Imaging of Fast Nanoscale Dynamics with Bright Microsecond Electron Pulses. *Nano Lett.* **2021**, 7.
- (27) Bongiovanni, G.; Olshin, P. K.; Drabbels, M.; Lorenz, U. J. Intense Microsecond Electron Pulses from a Schottky Emitter. *Appl. Phys. Lett.* **2020**, 116 (23), 234103.

Appendix 1.

Supporting information for Chapter 4

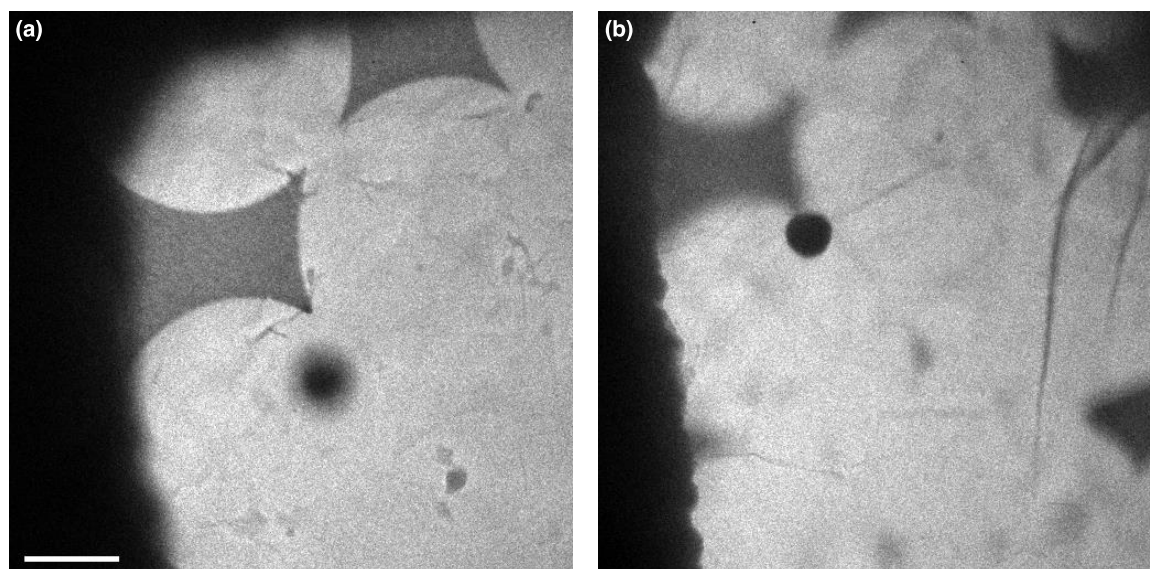


Figure S4-1. Droplet adhering to the top graphene layer. (a) Micrograph of a sample after being laser heated. The substrate plane is in focus and a blurred object appears in the middle of the image. (b) A micrograph of the same sample with the top graphene layer in focus reveals a resolidified nanodroplet adhering to the upper graphene layer. (Scale bar, 1 μm .)

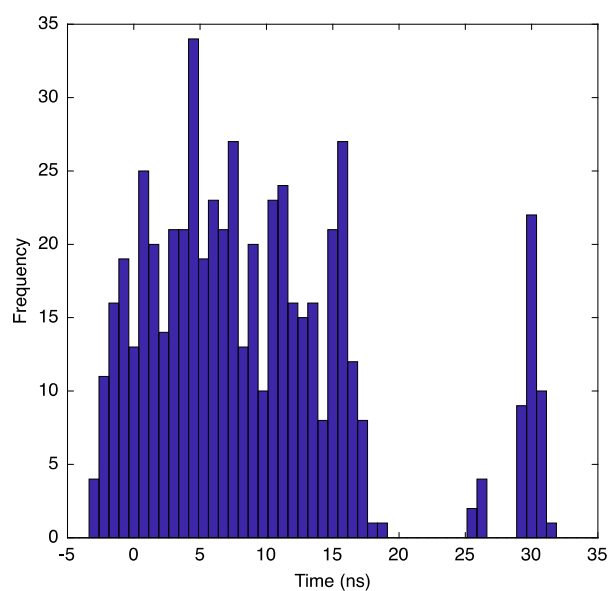
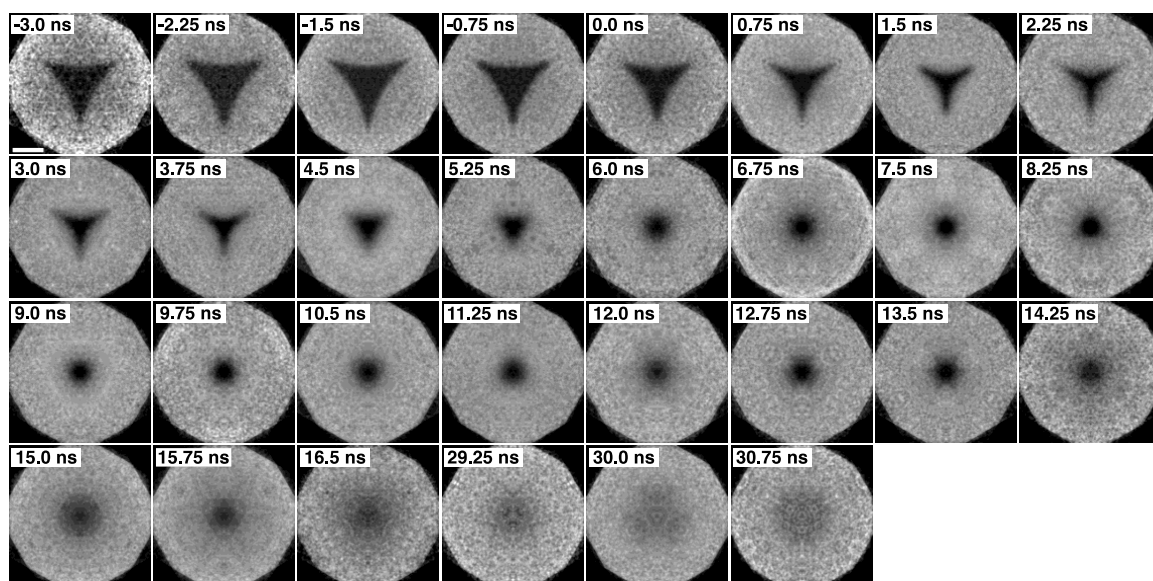


Figure S4-2. Ensemble images of jumping nanodroplets. The frames were obtained by averaging single-exposure images within 0.75 ns time-bins as described in the main text. In total, over 500 images were recorded. The distribution of their time delays is shown in the histogram. (Scale bar, 400 nm).

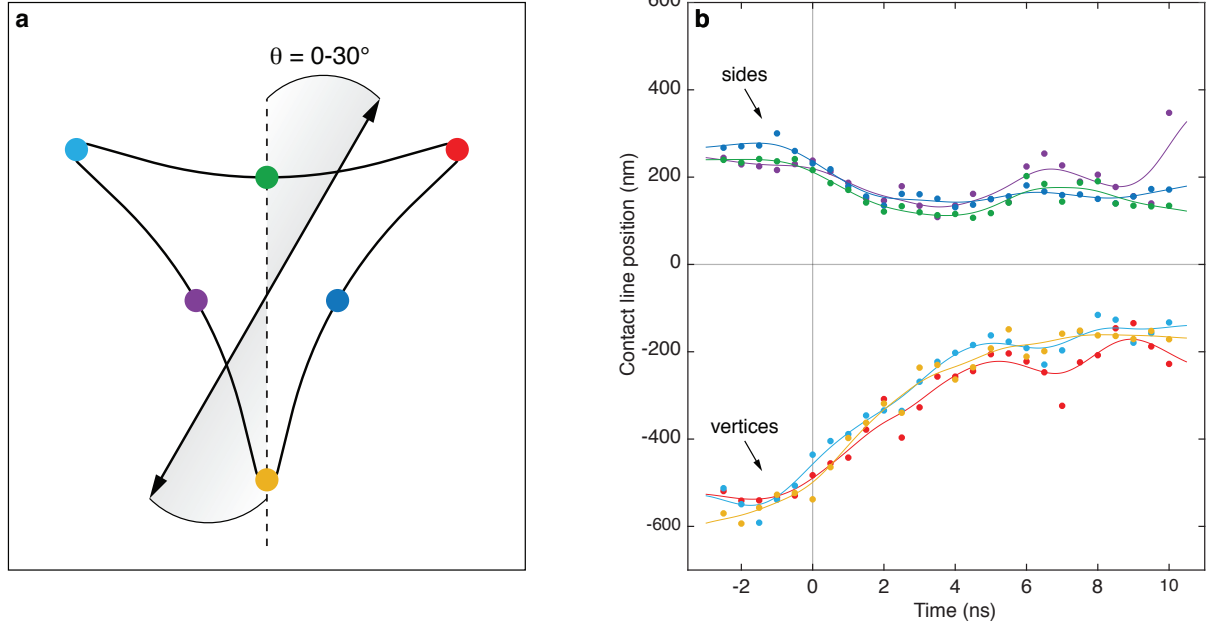


Figure S4-3. Analysis of the nanodroplet dynamics for different laser polarizations. (a) Single-exposure micrographs were aligned and averaged with the procedure described in the main text. Here, the additional constraint that the laser polarization should fall within an angle of $0-30^\circ$ with respect to the vertical was imposed (shaded area). After averaging, the ensemble images were not symmetrized. Note that now, the three vertices of the triangular prism are no longer equivalent if one considers the laser polarization; the same holds for the prism sides. (b) The droplet dynamics were analyzed as in the main text, with the center positions of the droplet boundaries shown here as a function of time (dots). The colored lines serve as guides for the eye. The transients bear close resemblance to those presented in Fig. 3(c) of the main text, although they appear noisier. This is expected since the ensemble images were not symmetrized. Importantly, within our experimental accuracy, the dynamics are the same for all three vertices and for all three sides, even though they are not equivalent with respect to the laser polarization. For example, the prism vertices and sides contract with similar velocities and reverse direction at similar times, respectively. We conclude that the morphological

dynamics of the system do not feature any measurable dependence on the polarization of the laser, which therefore cannot explain the asymmetries of the transient structures we observe.

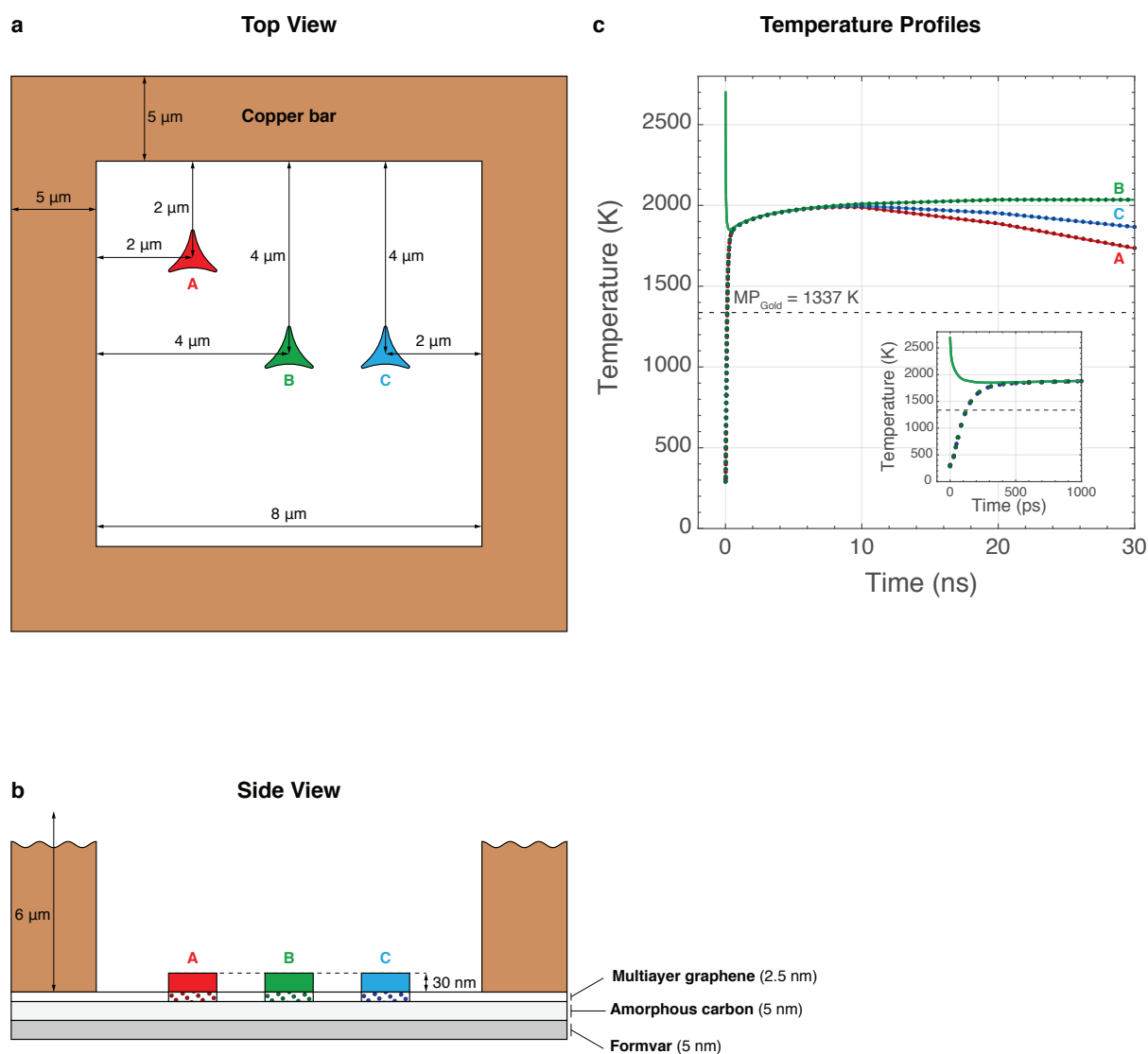


Figure S4-4. Simulation of the temperature evolution of laser heated gold nanoprisms. (a) Top and (b) side views for simulation geometry. The three gold nanoprisms (1 μm side length, 30 nm thickness) reside directly on multilayer graphene (2.5 nm thickness), which is supported by an amorphous carbon/formvar thin film (10 nm total thickness). The thin film is in contact with a copper mesh (5 μm width, 6 μm height, 8 μm inner spacing), which acts as a heat sink. (c) Finite element simulation of the temperature evolution of the three gold prisms using COMSOL Multiphysics.

We estimate that the laser pulse (515 nm, 3 ps, 86 mJ/cm²) initially heats the prisms to a temperature of 2706 K, while the graphene and amorphous carbon layers are heated to 4319 K and 2304 K, respectively.¹⁻⁹ Since the formvar polymer is transparent to the excitation wavelength, we assume that it initially remains at room temperature.¹⁰ This is also the case for the substrate underneath the nanoprisms, since the gold prisms are sufficiently thick to not transmit the laser light. Since the laser pulse deposits only a limited amount of energy on the copper bars, which have a large heat capacity, the copper mesh is also assumed to remain at room temperature.

The simulation reveals that after the laser pulse, the temperature of the nanoprisms (solid lines) equilibrates with that of the underlying substrate (dotted lines) on a timescale of 200 ps, with both reaching a temperature of about 1700 K. At such high temperatures, the gold structure can be expected to melt rapidly, on a timescale of 10 ps (Ref. 11), so that we can conclude that melting does not interfere with the fluid dynamics. Subsequently, the prisms slowly equilibrate with the surrounding hot substrate, and their temperatures rise to 2000 K at 10 ns, when the droplet jumps off the substrate (see main text). It should be noted that our simulation overestimates this temperature rise as it does not account for the fact that the contact area between the liquid gold droplet and its substrate rapidly shrinks as the droplet contracts. The simulation also reveals that all three prisms (A-C), placed in different locations with respect to the copper bars, have an almost identical temperature evolution. Small differences only appear at late times. Again, the simulation overestimates these differences as it does not consider the contraction of the droplet.

References

- (1) Yakubovsky, D. I.; Arsenin, A. V.; Stebunov, Y. V.; Fedyanin, D. Y.; Volkov, V. S. Optical Constants and Structural Properties of Thin Gold Films. *Opt. Express* **2017**, *25* (21), 25574–25587.
- (2) Arblaster, J. W. Thermodynamic Properties of Gold. *J. Phase Equilibria Diffus.* **2016**, *37* (2), 229–245.
- (3) Huang, J.; Zhang, Y.; Chen, J. K. Ultrafast Solid–Liquid–Vapor Phase Change of a Gold Film Induced by Pico- to Femtosecond Lasers. *Appl. Phys. A* **2009**, *95* (3), 643–653.
- (4) Weber, J. W.; Calado, V. E.; van de Sanden, M. C. M. Optical Constants of Graphene Measured by Spectroscopic Ellipsometry. *Appl. Phys. Lett.* **2010**, *97* (9), 091904.
- (5) Pop, E.; Varshney, V.; Roy, A. K. Thermal Properties of Graphene: Fundamentals and Applications. *MRS Bull.* **2012**, *37* (12), 1273–1281.
- (6) Spencer, H. M. Empirical Heat Capacity Equations of Gases and Graphite. *Ind. Eng. Chem.* **1948**, *40* (11), 2152–2154.
- (7) Arakawa, E. T.; Williams, M. W.; Inagaki, T. Optical Properties of Arc-evaporated Carbon Films between 0.6 and 3.8 eV. *J. Appl. Phys.* **1977**, *48*, 3176.
- (8) Bullen, A. J.; O'Hara, K. E.; Cahill, D. G.; Monteiro, O.; von Keudell, A. Thermal Conductivity of Amorphous Carbon Thin Films. *J. Appl. Phys.* **2000**, *88* (11), 6317–6320.
- (9) Natali, M.; Puri, I.; Rallini, M.; Kenny, J.; Torre, L. Ablation Modeling of State of the Art EPDM Based Elastomeric Heat Shielding Materials for Solid Rocket Motors. *Comput. Mater. Sci.* **2016**, *111*, 460–480.
- (10) Xie, X.; Li, D.; Tsai, T.-H.; Liu, J.; Braun, P. V.; Cahill, D. G. Thermal Conductivity, Heat Capacity, and Elastic Constants of Water-Soluble Polymers and Polymer Blends. *Macromolecules* **2016**, *49* (3), 972–978.

(11) Mo, M. Z.; Chen, Z.; Li, R. K.; Dunning, M.; Witte, B. B. L.; Baldwin, J. K.; Fletcher, L. B.; Kim, J. B.; Ng, A.; Redmer, R.; et al. Heterogeneous to Homogeneous Melting Transition Visualized with Ultrafast Electron Diffraction. *Science* **2018**, *360*, 1451–1455.

List of Figures

Figure 2-1. Overview of the time-resolved electron microscope.....	29
Figure 2-2. Characterization of the spatial, energy, and temporal resolution.....	32
Figure 2-3. Characterization of electron pulses with high charge densities.....	35
Figure 2-4. Determination of the brightness for ultrafast electron pulses.....	38
Figure 3-1. Formation of aligned dual-gold-core silica shell nanoparticles under femtosecond laser irradiation.....	52
Figure 3-2. Angular distribution and yield of the dual-cores as a function of laser fluence...	54
Figure 3-3. Effects of laser polarization and pulse duration on the formation of dual-cores...	55
Figure 3-4. <i>In-situ</i> observation of the formation of aligned dual-core particle.....	57
Figure 3-5. High resolution micrographs of progeny particles.....	58
Figure 3-6. The formation mechanism of dual-core particles.....	61
Figure 4-1. Gold nanoprisms as precursors of jumping nanodroplets.....	73

Figure 4-2. Snapshots of jumping nanodroplets and ensemble images.....	75
Figure 4-3. Analysis of the jumping nanodroplet dynamics.....	77
Figure 4-4. Heterogeneity of the nanoscale fluid dynamics and non-spherical geometries of free droplets.....	80
Figure S4-1. Droplet adhering to the top graphene layer.....	97
Figure S4-2. Ensemble images of jumping nanodroplets.....	98
Figure S4-3. Analysis of the nanodroplet dynamics for different laser polarizations.....	99
Figure S4-4. Simulation of the temperature evolution of laser heated gold nanoprisms.....	101

List of tables

Table 2-1. Brightness of the photoelectron pulses for different operating parameters.....	42
--	----

Acknowledgments

This thesis could not be completed successfully without the support and assistance of many great people. I would like to thank:

My PhD advisor, Professor Ulrich J. Lorenz for the exciting opportunity to join the Laboratory of Molecular Nanodynamics. I greatly appreciate all the knowledge and experience he shared with me and the research independence I was provided;

The teams of the mechanical and electronics workshops, especially André Fattet, who actively participated in solving various problems that we had during the modification of the microscope, and Benjamin Charles Le Geyt, who helped us with the high voltage equipment and wrote the data acquisition software;

JEOL engineers for their assistance during this project, especially Naoki Tsukamori, who helped us a lot in the modification of the instrument, and Lionel Cachoulet, who often visited our laboratory to fix different problems that we had during these years;

All the past and current members of LND group, for the warm and productive atmosphere in the group, especially, Professor Marcel Drabbels for his valuable comments and fruitful discussions during our group meetings, Annick Gaudin Delmonaco for all the support during my PhD that started even before I arrived to Lausanne, Dr. Johnathan M. Voss for his sense of humor that always keeps the great mood in the group, Gabriele Bongiovanni for the great time I had when we were performing different experiments.

Members of LMCP group, for all the group outings and celebration we held together. In particular, I would like to thank Dr. Valeriu Scutelnic, for his optimism, and Professor Oleg Boyarkine for the great teaching experience.

Members of the committee, Professor Rainer Beck, Professor Oh-Hoon Kwon, Dr. Florent Houdellier, and Professor Christoph Bostedt for accepting to participate in the oral exam and valuable comments.

Finally, I would like to thank my family for their support and encouragement during PhD.

Curriculum Vitae

Education

École polytechnique fédérale de Lausanne (EPFL) February 2017 - Present

PhD advisor: Prof. Ulrich J. Lorenz

Thesis: Time-Resolved Electron Microscopy: Principle and Applications

Saint Petersburg State University September 2013 – June 2015

M.S. in laser chemistry

Saint Petersburg State University September 2009 – June 2013

B.S. in laser chemistry

Teaching activities

1. Experimental physical chemistry for Bachelor students: spring semesters 2018, 2019, 2020.
2. General physics: electromagnetism for Bachelor students: fall semesters 2018, 2019.

Publications

1. P. K. Olshin, G. Bongiovanni, M. Drabbels, U. J. Lorenz, Atomic-Resolution Imaging of Fast Nanoscale Dynamics with Bright Microsecond Electron Pulses. *Nano Lett.* **21**, 612–618 (2021).
2. Y.-C. Cheng, et al., Imaging multiphoton ionization dynamics of CH₃I at a high repetition rate XUV free-electron laser. *J. Phys. B At. Mol. Opt. Phys.* **54**, 014001 (2021).
3. P. K. Olshin, M. Drabbels, U. J. Lorenz, Characterization of a time-resolved electron microscope with a Schottky field emission gun. *Struct. Dyn.* **7**, 054304 (2020).

4. G. Bongiovanni, P. K. Olshin, M. Drabbels, U. J. Lorenz, Intense microsecond electron pulses from a Schottky emitter. *Appl. Phys. Lett.* **116**, 234103 (2020).
5. P. K. Olshin, J. M. Voss, M. Drabbels, U. J. Lorenz, Real-time observation of jumping and spinning nanodroplets. *Struct. Dyn.* **7**, 011101 (2020).
6. J. M. Voss, P. K. Olshin, R. Charbonnier, M. Drabbels, U. J. Lorenz, *In Situ* Observation of Coulomb Fission of Individual Plasmonic Nanoparticles. *ACS Nano*. **13**, 12445–12451 (2019).
7. F. Brauße, et al., Time-resolved inner-shell photoelectron spectroscopy: From a bound molecule to an isolated atom. *Phys. Rev. A*. **97**, 043429 (2018).
8. A. S. Mereshchenko, O. S. Myasnikova, P. K. Olshin, S. M. Matveev, M. S. Panov, V. A. Kochemirovsky, M. Yu. Skripkin, A. N. Tarnovsky, Ultrafast Excited-State Dynamics of Ligand-Field and Ligand-to-Metal Charge-Transfer States of CuCl_4^{2-} in Solution: A Detailed Transient Absorption Study. *J. Phys. Chem. B*. **122**, 10558–10571 (2018).
9. F. Allum, et al., Coulomb explosion imaging of CH_3I and CH_2ClI photodissociation dynamics. *J. Chem. Phys.* **149**, 204313 (2018).
10. P. K. Olshin, O. S. Myasnikova, M. V. Kashina, A. O. Gorbunov, N. A. Bogachev, V. O. Kompanets, S. V. Chekalin, S. A. Pulkin, V. A. Kochemirovsky, M. Yu. Skripkin, A. S. Mereshchenko, The electronic spectra and the structures of the individual copper(II) chloride and bromide complexes in acetonitrile according to steady-state absorption spectroscopy and DFT/TD-DFT calculations. *Chem. Phys.* **503**, 14–19 (2018).
11. M. Burt, et al., Coulomb-explosion imaging of concurrent CH_2BrI photodissociation dynamics. *Phys. Rev. A*. **96**, 043415 (2017).
12. V. Veiko, Y. Karlagina, M. Moskvina, V. Mikhailovskii, G. Odintsova, P. Olshin, D. Pankin, V. Romanov, R. Yatsuk, Metal surface coloration by oxide periodic structures formed with nanosecond laser pulses. *Opt. Lasers Eng.* **96**, 63–67 (2017).

13. P. K. Ol'shin, A. V. Povolotskii, A. A. Man'shina, V. A. Markov, I. A. Sokolov, Optic properties of niobium-phosphate glasses containing lithium, sodium, and potassium oxides. *Glass Phys. Chem.* **43**, 294–297 (2017).
14. A. S. Mereshchenko, P. K. Olshin, O. S. Myasnikova, M. S. Panov, V. A. Kochemirovsky, M. Yu. Skripkin, P. N. Moroz, M. Zamkov, A. N. Tarnovsky, Ultrafast Photochemistry of Copper(II) Monochlorocomplexes in Methanol and Acetonitrile by Broadband Deep-UV-to-Near-IR Femtosecond Transient Absorption Spectroscopy. *J. Phys. Chem. A*. **120**, 1833–1844 (2016).
15. O. Yu. Tretiak, J. W. Blanchard, D. Budker, P. K. Olshin, S. N. Smirnov, M. V. Balabas, Raman and nuclear magnetic resonance investigation of alkali metal vapor interaction with alkene-based anti-relaxation coating. *J. Chem. Phys.* **144**, 094707 (2016).
16. A. A. Vasileva, I. A. Nazarov, P. K. Olshin, A. V. Povolotskiy, I. A. Sokolov, A. A. Manshina, Structural features of silver-doped phosphate glasses in zone of femtosecond laser-induced modification. *J. Solid State Chem.* **230**, 56–60 (2015).
17. A. S. Mereshchenko, P. K. Olshin, K. E. Karabaeva, M. S. Panov, R. M. Wilson, V. A. Kochemirovsky, M. Yu. Skripkin, Y. S. Tveryanovich, A. N. Tarnovsky, Mechanism of Formation of Copper(II) Chloro Complexes Revealed by Transient Absorption Spectroscopy and DFT/TDDFT Calculations. *J. Phys. Chem. B*. **119**, 8754–8763 (2015).
18. A. A. Manshina, A. V. Povolotskiy, P. K. Ol'shin, A. A. Vasileva, V. A. Markov, I. A. Sokolov, Structure of lithium-niobium phosphate glass promising for optical phase elements creation with femtosecond laser radiation. *Glass Phys. Chem.* **41**, 572–578 (2015).
19. A. S. Mereshchenko, P. K. Olshin, A. M. Karimov, M. Yu. Skripkin, K. A. Burkov, Y. S. Tveryanovich, A. N. Tarnovsky, Photochemistry of copper(II) chlorocomplexes in acetonitrile: Trapping the ligand-to-metal charge transfer excited state relaxations pathways. *Chem. Phys. Lett.* **615**, 105–110 (2014).